
MODELLING MULTI-SCALE
ATMOSPHERE AND LAND-SURFACE INTERACTIONS
–A LARGE-ENSEMBLE APPROACH–

INAUGURAL-DISSERTATION
ZUR
ERLANGUNG DES DOKTORGRADES
DER MATHEMATISCH-NATURWISSENSCHAFTLICHEN FAKULTÄT
DER UNIVERSITÄT ZU KÖLN

vorgelegt von
Zahra Sadat Parsakhoo
aus Teheran

KÖLN, 2019

Berichtersteller:

Prof. Dr. Y. Shao
PD. Dr. H. Elbern

Tag der mündlichen Prüfung:

29.11.2019

Contents

Abstract	IV
Zusammenfassung	VII
List of Figures	IX
List of Tables	XIII
List of acronyms	XV
1. Introduction	1
1.1. Land-surface heterogeneity in numerical models	1
1.2. Atmosphere and land-surface interactions in numerical models	4
1.3. Research objectives	6
2. Definition of a simulation and analysis framework	9
2.1. Para-real simulation	9
2.1.1. Simulation framework	9
2.1.2. Analysis framework	11
2.2. Synthesized surface pattern generation	11
2.2.1. Fractal approach	13
2.2.2. Quasi fractional Brownian surface (quasi-fBs)	16
2.3. Estimation of scales from original geo-SPs	20
2.4. Analysis approach	21
2.4.1. The classic ANOVA method	22
2.4.2. Application	23
3. Model setup and case description	27
3.1. The Weather Research and Forecasting (WRF) model	27
3.1.1. Model discretization	28
3.1.2. Nesting	30
3.1.3. Physics options	30
3.1.4. Surface layer parameterization	30
3.1.5. Land-surface model	32
3.2. Synoptic situation	33
3.3. Reference run	36
3.3.1. Setup	36
3.3.2. Evaluation	40
4. Illustration of the simulation and analysis framework	43
4.1. Synthesized surface pattern as a lower boundary condition	43

4.2. Impact of random realizations on surface–atmosphere interactions	46
5. Quantifying the impact of land-surface heterogeneity on the atmosphere	51
5.1. Multi-dimensional variance decomposition	52
5.1.1. Thermodynamic coupling through surface albedo (α)	55
5.1.2. Hydrological coupling through soil-type (s_t)	55
5.1.3. Aerodynamic coupling through surface roughness (z_0)	56
5.1.4. Remarks	57
5.2. Correlation of synthesized SPs with full 2D standing eddy	58
5.2.1. Thermodynamic coupling through α	58
5.2.2. Hydrological coupling through s_t	61
5.2.3. Aerodynamic coupling through z_0	63
5.2.4. Remarks	64
6. Propagation of the land-surface pattern into the atmosphere	65
6.1. Vertical propagation of the surface signal into 3D standing eddy (f_{xyz})	66
6.1.1. Thermodynamic coupling by α	68
6.1.2. Hydrological coupling by s_t	69
6.1.3. Aerodynamic coupling by z_0	70
6.1.4. Remarks	71
6.2. Vertical propagation of SSP into full stationary eddy (f_{hz})	72
6.2.1. Thermodynamic coupling via α	74
6.2.2. Hydrological coupling via s_t	76
6.2.3. Aerodynamic coupling via z_0	76
6.2.4. Remarks	77
6.3. Temporal propagation of horizontal eddy (f_{xyt})	78
6.3.1. Thermodynamic coupling through α	78
6.3.2. Hydrological coupling through s_t	78
6.3.3. Aerodynamic coupling through z_0	80
6.3.4. Remarks	80
6.4. Temporal evolution of merged temporal/horizontal eddy (f_{ht})	80
6.4.1. Thermodynamic coupling via α	81
6.4.2. Hydrological coupling via s_t	83
6.4.3. Aerodynamic coupling via z_0	84
6.4.4. Remarks	85
7. Summary and discussion	87
7.1. Para-real ensemble modelling	87
7.2. Insights to individual land–atmosphere coupling mechanisms	88
7.3. The role of length scale and persistency on surface–atmosphere couplings	89
7.4. Synthesis	90
A. Supplement figure	93
Bibliography	95
Erklärung	101

Acknowledgements

103

Abstract

The solid earth as a basic component of the climate system profoundly influences the development of the atmospheric boundary layer, in particular through processes at the interface. As land-surface properties are heterogeneous over a broad range of length-scales, surface-induced fluxes are heterogeneous too. Representing land-surface heterogeneity and the corresponding fluxes is a challenging task in numerical prediction of weather and projection of climate. Earlier studies separate the role of heterogeneity into *flux aggregation* and *dynamic effects*.

In this work, we introduce the approach of '*para-real*' *ensemble modelling* to investigate the dynamic effect of land-surface heterogeneity. We perform a large ensemble of high-resolution simulations using the Weather research and forecast model (WRF) in its advanced research mode (WRF-ARW) together with the Noah-MP land surface model (LSM). The para-real simulation ensembles are externally forced by a reanalysis of a real case in spring 2013, but become exposed to different synthesized surface patterns (SP) generated as quasi-fractal Brownian surfaces (quasi-fBs) with exact control of the dominant wave length and fractal persistence to satisfy a tailored randomized-spectrum.

The focus of this study is on the three inter-related land-surface and atmosphere coupling mechanisms—the *thermodynamic coupling*, *aerodynamic coupling*, and *hydrological coupling*. For each mechanism, a corresponding surface property is identified, namely surface albedo (α) for thermodynamic coupling, roughness length (z_0) for aerodynamic coupling, and soil type (s_t) for hydrological coupling. For each surface property, we generate a set of quasi-fBs with different dominant length scale and fractal persistence. In our para-real ensembles, the original fields of the surface properties are—in a first step—derived from satellite data (for α) and/or in-situ estimates (for z_0 and s_t). In a second step, these are replaced by the quasi-fBs, for which we estimate the control parameters from the original data, i.e., the probability density distribution of the original data matches that of the quasi-fBs which eliminates the flux aggregation effect and allows us to focus on the dynamic effect. In total, 480 simulations, i.e., ensembles of 48 physical cases each containing 10 random realizations, are analyzed using Analysis of Variance (ANOVA); this allows for an isolated analysis of the signal contained in particular dimensional combinations, for instance the horizontal plane.

We find, first, a strong impact of the length scale of the surface forcing on the intensity of coupling: while the dynamic effect of surface heterogeneity significantly impacts the state of the atmospheric boundary layer for all cases investigated, the impact of the surface signal on the atmospheric state grows with the length-scale of the surface heterogeneity. Second, we demonstrate that larger fractal persistence of the surface signal also strengthens the atmosphere–surface coupling. Third, the qualitative impact of the surface forcing is shown to depend on time, which eliminates the possibility of a simple linear forward propagation of the surface signal; there is strong sensitivity to the diurnal cycle,

in particular with respect to the horizontal wind components: The maximum intensity of atmosphere–surface coupling (measured in terms of correlation) is found around noon for the atmospheric temperature, and some hours later (in the early afternoon) for water vapor. Fourth, among the different surface forcing investigated, we find that the heterogeneity of soil type is the most important to the atmospheric state–surface exchanges and its signal are detected in the atmospheric water-vapor up to 2 km height; in particular, the soil-type pattern with the smallest length-scale causes a doubling of cloud-water above 500 m height whereas no impact on the bulk atmospheric state is found for patterns with other length-scales and fractal persistence or forcing of other surface variables. This illustrates the key part that hydrological coupling plays in connecting the atmosphere to the surface, and it underlines the relevance of improved hydrological process-level representation for improved parameterization of the coupled land–atmosphere system.

Zusammenfassung

Die feste Erde hat als wesentlicher Bestandteil des Klimasystems einen maßgeblichen Einfluss auf die Entwicklung der planetaren Grenzschicht, insbesondere durch Prozesse an der Grenzfläche. Da die Eigenschaften der Landoberfläche auf vielen Längenskalen variieren, sind auch die dadurch hervorgerufenen Flüsse an der Oberfläche heterogen. Die Wiedergabe der Oberflächenheterogenität und der daraus resultierenden Flüsse ist daher eine Herausforderung der numerischen Wettervorhersage und Klimaprojektion. Frühere Untersuchungen unterteilen die Wirkung der Heterogenität in die *Aggregation von Oberflächenflüssen* und *dynamische Effekte der Oberflächenflüsse*.

In dieser Arbeit führen wir den Ansatz der *para-reellen Ensemblemodellierung* ein, um den dynamischen Effekt der Oberflächenheterogenität zu untersuchen. Wir untersuchen ein großes Ensemble von hochaufgelösten Simulationen mit dem *Weather Research and Forecast Model* (WRF) in der Forschungsversion (WRF-ARW) und mit dem Noah-MP Landoberflächenmodell (LSM). Die para-reellen Simulationsensembles werden extern durch die Reanalyse eines Falls im Frühling 2013 angetrieben, dabei jedoch unterschiedlichen synthetischen Randbedingungen für die Landoberfläche ausgesetzt, welche mittels einer maßgeschneiderten spektralbasierten Zufallsmethode als quasi-fraktale Brown'sche Oberflächen (qfBO) erstellt werden. Dabei wird die dominante Wellenlänge und die fraktale Persistenz kontrolliert variiert.

Wir fokussieren uns auf drei Mechanismen der Land–Atmosphärenkopplung: *thermodynamische, aerodynamische und hydrologische Kopplung*. Für jeden dieser Mechanismen identifizieren wir eine atmosphärische Variable, die direkt Änderungen in lediglich dem jeweiligen Mechanismus hervorrufen soll; das ist die Oberflächenalbedo (α) für die thermodynamische Kopplung, die Rauigkeitslänge (z_0) für die aerodynamische Kopplung und der Oberflächentyp (s_r) für die hydrologische Kopplung. Für jede Oberflächeneigenschaft, werden qfBO mit unterschiedlicher dominanter Längenskala und fraktaler Persistenz erstellt. In unseren para-reellen Modellensembles werden in einem ersten Schritt die Ursprungsfelder aus den realen Oberflächendaten aus Satellitenbeobachtungen für die Albedo und/oder in-situ Abschätzungen für Rauigkeit und Bodentyp abgeleitet. In einem weiteren Schritt werden diese ursprünglichen Felder durch eine große Anzahl an qfBO ersetzt, wobei wir die Parameter der qfBO basierend auf den ursprünglichen Geodaten abschätzen, d.h. die ursprüngliche Wahrscheinlichkeitsdichteverteilung bleibt erhalten um Effekte der Flussaggregation zu eliminieren und so den dynamischen Effekt zu isolieren. Insgesamt untersuchen wir 480 Simulationen – das sind 48 Ensembles unterschiedlicher physikalischer Fälle mit je 10 unterschiedlichen Zufallsrealisationen – mittels Varianzanalyse (ANOVA); dies ermöglicht die isolierte Untersuchung des Signals in einer bestimmten Kombination von Dimensionen, zum Beispiel in der horizontalen Ebene.

Wir zeigen, erstens, einen starken Einfluss der Längenskala des Oberflächenantriebes auf die Intensität der Land–Atmosphärenkopplung: Während der dynamische Effekt der

Oberflächenheterogenität für alle untersuchten Fälle einen maßgeblichen, statistisch signifikanten Einfluss auf den Zustand der atmosphärischen Grenzschicht hat, ist der Einfluss bei größeren Längenskalen des Oberflächenantriebes größer. Zweitens zeigen wir, dass auch zunehmende fraktale Persistenz die Kopplung zwischen Atmosphäre und Landoberfläche verstärkt. Drittens ist selbst der qualitative Einfluss des Oberflächenantriebes zeitabhängig, was die Möglichkeit linearer Vorwärtsoperatoren für die Kopplung ausschließt; wir finden eine starke Abhängigkeit des Vorzeichens der Kopplung vom Tageszyklus, insbesondere im Hinblick auf den Horizontalwind: Die intensivste Kopplung zwischen Oberfläche und Atmosphäre (gemessen anhand der Korrelation) finden wir in den Mittagsstunden für die Temperatur und einige Stunden später (am frühen Nachmittag) für den Wasserdampf. Viertens finden wir – im Vergleich der verschiedenen Antriebe –, dass die Heterogenität des Bodentyps den größten Einfluss auf die Atmosphäre hat. Der Einfluss der Oberfläche ist bis in eine Höhe von 2 km nachweisbar; insbesondere führt das Bodentypmuster mit der kleinsten Längenskala zu einer Verdopplung des Wolkenwassergehalt oberhalb von 500 m, wohingegen Änderungen in den mittleren Profilen für Oberflächenmuster mit anderen Längenskalen, anderer Persistenz bzw. für Oberflächenmuster anderer Parameter nicht nachweisbar sind. Dies illustriert die Schlüsselrolle, die die hydrologische Kopplung für die Verbindung der Atmosphäre mit der Oberfläche spielt, und es unterstreicht die Relevanz einer verbesserten Prozesswiedergabe der hydrologischen Kopplung für bessere Parameterisierungen des gekoppelten Land–Atmosphäre Systems.

List of Figures

1.1.	Illustration of the surface–atmosphere interactions within the planetary boundary layer (PBL) including the exchange of energy, namely as the net shortwave radiation at the surface, S_{net} , the net longwave radiation at the surface, L_{net} , the surface sensible heat flux, H , the surface latent heat flux, LE , the ground heat flux, G ; the exchange of the momentum flux at the surface (friction), M ; the exchange of water; and the exchange of trace constituents (CO_2 , CH_4 , N_2O ,...).	2
1.2.	Schematic representation of mosaic, tile (adapted from AMENT AND SIMMER [2006]), and semi-tile (adapted from NIU ET AL. [2011]) approaches. Symbols in semi-tile panel are the same as Fig. 1.1. Subscripts 'b' and 'v' denote the 'bare' and 'vegetated' area, respectively.	3
2.1.	Illustration of SPs of the specified surface properties for a real case (left column) versus a para-real case (right column). The left column shows the original SPs of two model domains. The first row (a,b) is for land-used index, the second (c,d) for albedo, third (e,f) for roughness-length, and bottom row (g,h) for soil-type. The right column shows the original SP of the outer domain (d01) and an example of the synthesized SPs of the inner domain (d02). The SPs of LU is not changed in any para-real run, and only the SP of the single specific surface property of the d02 is replaced individually by the synthesized one.	10
2.2.	(a) The real SP of roughness-length for a model domain under this study. (b) The PDF of (a). (c) An intermediate pattern is generated by the quasi-fBs approach. The SP of subfigure-a exhibits continuous values which are normalized between +1 and -1. (d) A synthesized SP for roughness-length. The SP of subfigure-d indicates categorical values. The intermediate pattern is converted to the synthesized SP of z_0 through the PDF of a real SP.	12
2.3.	Schematic of equation (2.9) in loglog scale with $s_1 = 4$ and $s_2 = 1.5$ which is normalized at the maximum of k	16
2.4.	Plots (a)-(f) illustrate fields generated by quasi-fBs approach in xy-plane with $n = 150$ points and $s_1 = 4$. Plot (g) shows the corresponding power spectra.	19
2.5.	Power spectrum of α for the 25 domains given in table 2.1 (colored curves) with the best linear fit curve (solid black curve).	20
2.6.	Intermediate SPs according to estimations in table 2.2. Numbers assigned to each SP are used in chapter 4, 5, and 6 for the sake of easier discussions.	21
2.7.	Schematic of ANOVA decompositions for a 3D-multivariate function.	23
3.1.	WRF system flowchart for a real simulation including the WPS and the ARW solver. The green rectangle indicates an extra step in this study to replace the original SP with a synthesized SP.	28
3.2.	Horizontal and vertical grids of the WRF ARW. Red circle at the center of grid indicates mass point.	29

3.3.	Equivalent potential temperature at 900 hPa pressure UTC 12:00 on a) 24th, b) 25th, and c) 26th of April 2013. White contour lines indicate mean sea level (msl) pressure in hPa. Dashed white contour lines show msl below 1013 hPa and solid white contour lines show msl above 1013 hPa. Contours interval is 2 hPa.	34
3.4.	Low cloud cover (lcc) at UTC 12:00 on a) 24th, b) 25th, and c) 26th of April 2013. Red arrows indicate horizontal wind velocity at 500 hPa. The reference wind velocity vector equals to 40 ms^{-1}	35
3.5.	Map of model domains in Europe region. $d01$ is parent domain. $d02$ is inner domain which is under study. It shows the topography of the model domains: Eifel mountain area is indicated by brown color and almost flat area is shown by green color.	36
3.6.	Original SPs of albedo (left), roughness-length (center) and soil-type (right) (upper row) and their corresponding PDF (bottom row).	37
3.7.	Illustration of soil layers/thicknesses and η -levels used in this study (left) versus default soil layers/thicknesses in Noah-MP LSM and default η -levels in WRF.	39
3.8.	Vertical profile of potential temperature (left column) and specific humidity (right column) at UTC: 12:00. Red, black and blue curves correspond to observation, reference model run, and ERA-Interim ECMWF forcing data at Jülich location. Rows show the days of study starting on 24.04.2013 to 26.04.2013.	41
4.1.	Influence of the individual synthesized SP on atmospheric bulk parameters. Sub-figures (a), (b), and (c) show the synthesized SP of α , s_t , and z_0 , respectively; generated by $s_2=3$ and $k_{max}=0.1$. The remaining subfigures indicate the differences of the atmospheric states $-T2$ [K] (d,e), $Q2$ [kgkg^{-1}] (g,h), $UV = \sqrt{U_{10}^2 + V_{10}^2}$ [ms^{-1}] (f), and W [ms^{-1}] at the first vertical level (i)– between the reference run and the para-real run with a specified synthesized SP shown on top of each column at 15 UTC.	45
4.2.	Random realization for the four synthesized SPs at the corners of Fig. 2.6. Five different sets of random realization (columns) for each case (rows). Patterns are normalized between -1 and +1.	47
4.3.	The sensitivity index of the full horizontal variance (S_{xy}) of temperature (a), water-vapor (b), and cloud-water (c) is shown. The horizontal axis indicates the four cases of study which are forced by the synthesized SP. Numbering of the cases is according to the numbering of the synthesized SP in the Fig. 2.6. Each box indicates S_{xy} variations over the 10 rr. The color of boxes refers to a simulation which is forced by a synthesized SP of a specific surface property: α (orange), z_0 (green) and s_t (blue). The bottom and top edges of the box shows the 25th and 75th percentiles of S_{xy} data, respectively. The mark inside the box shows the median and the whiskers are extended to the most extreme values. The outliers are plotted with the red '+' symbol individually.	49
4.4.	Same as Fig. 4.3, but for wind components: horizontal wind (a), and W (b).	50

5.1.	Sensitivity indices, S_u for: (a) Temperature, (b) Water-vapor, and (c) Cloud-water. Columns show different decomposed variance components and rows indicate \bar{S}_u for different para-real runs: albedo ($\alpha_1, \dots, \alpha_{16}$), roughness-length (z_1, \dots, z_{16}), and soil-type (s_1, \dots, s_{16}). The subscripts refer to numbering in Fig. 2.6 for different synthesized SPs. The colorbar indicates the ratio of the variance components of the reference run to the mean over 10 rr of the variance components of the para-real runs. Gray color exhibits insignificant difference between \bar{S}_u and $S_{u,ref}$ with 90% confidence.	53
5.2.	Same as 5.1, but for: (a) U, (b) V, and (c) W.	54
5.3.	Correlation between a synthesized SP and \mathbf{T}_{xy} (a, b, c), \mathbf{QV}_{xy} (d, e, f), \mathbf{QC}_{xy} (g, h, i), and \mathbf{UV}_{xy} (j, k, l) and for 3 surface properties: α (left column), z_0 (middle column), and s_t (right column). Each matrix contains 16 cells indicating 16 synthesized SP of Fig. 2.6.	59
6.1.	Vertical profile of $\bar{R}_{N_{xyz}}^M$ for α (left column), z_0 (middle column), and s_t (right column) with T_{xyz} (a,b,c), QV_{xyz} (d, e, f), QC_{xyz} (g, h, i), and UV_{xyz} (j, k, l). The legend shows 16 synthesized SP according to numbering in Fig. 2.6.	67
6.2.	Vertical profile of the correlation between the synthesized SPs of three surface properties (α (left column), z_0 (center column), and s_t (right column)) and the T_{hz} (a, b, c), QV_{hz} (d, e, f), QC_{hz} (g, h, i), and UV_{hz} (j, k, l). The axes and colors are similar to Fig. (6.1).	73
6.3.	Time series of integrated cloud-water below 500 m (a), in an atmospheric layer between 500 m and below 2 km (b), and below 2 km (c) for para-real simulations forced by s_t . The color of curves is similar to Fig. 6.1.	75
6.4.	Time series of the correlation between the synthesized SPs of s_t and the T_{xyt} (a), and QV_{xyt} (b), and between the synthesized SP of z_0 and UV_{xyt} (c). The colors are similar to Fig. (6.1). The horizontal black dashed lines indicate noon time of the two days of the simulations at UTC time scale.	79
6.5.	Time series of the correlation between the synthesized SPs of three surface properties, α (left column), z_0 (middle column), s_t (right column) and for T_{ht} (a, b, c), QV_{ht} (d, e, f), QC_{ht} (g, h, i), and UV_{ht} (j, k, l). The axes and colors are similar to Fig. (6.4).	82
A.1.	Vertical mean profile of temperature (a), water-vapor (b), cloud-water(c), and horizontal wind (d). The profiles are similar for all para-real simulations regardless of which surface properties used for forcing.	93

List of Tables

2.1. Location of the center of 25 domains.	20
2.2. Proposed range of s_2 and k_{max} based on the estimation from original SPs. . .	21
3.1. WRF model physics options used in this study.	31
5.1. A list of soil properties given by SOILPARM.TBL of WRF.	61
6.1. Contribution of subspace variance into the total variance [%] from the reference run.	66
6.2. Maximum chance to explain an atmospheric signal by a single couplings through the corresponding surface property: $E_u^M = S_u^M \times \bar{R}_{N_u}^M _{max}$. Colors indicate different couplings: thermodynamic (red), aerodynamic (green), and hydrological (blue) coupling.	85

List of Acronyms

1D	one dimensional
2D	two dimensional
3D	three dimensional
4D	four dimensional
ANOVA	Analysis of variance
ARW	Advance Research WRF
AVHRR	Advanced Very High Resolution Radiometer
CFL	Courant-Friedrichs-Lewy
CHEOPS	Cologne High Efficient Operating Platform for Science
ECMWF	European Centre for Medium Range Weather Forecasts
fBm	fractional Brownian motion
fBs	fractional Brownian surface
GSI	Global Sensitivity Index
HOPE	HD(CP)2 Observational Prototype Experiment
HPC	High Performance Computing
lcc	low cloud cover
LES	Large Eddy Simulation
LSM	Land Surface Model
mslp	mean sea level pressure
NWP	Numerical Weather Prediction
PDF	Probability Density Function
PBL	Planetary Boundary Layer
RK3	third-order Runge-Kutta
rr	Random Realization
SP	Surface Pattern
SSP	Synthesized Surface Pattern
SZA	Solar Zenith Angle
USGS	United States Geological Survey
WPS	WRF Preprocessing System
WRF	Weather Research and Forecasting

1. Introduction

The land-surface plays an important role in weather and climate systems through energy, mass, and momentum exchanges with the atmosphere [AVISSAR AND PIELKE, 1989]. It is naturally heterogeneous over a wide range of length scales [GIORGI AND AVISSAR, 1997], with the spatially and temporally varying thermal, optical, aerodynamic and hydrological surface properties. As a result, land-surface fluxes are also heterogeneous. While the horizontal resolution of the numerical weather-prediction and climate models has been rapidly increasing in recent years, it remains an unsolved problem how to deal with sub-grid scale land-surface heterogeneity. It is, however, known that a misrepresentation of surface heterogeneity may lead to substantial inaccuracy of model outcomes (e.g., HECHTEL ET AL. [1990]; MAHRT [2000]). In the present study, we use a high-resolution numerical weather prediction model to quantify the effects of surface heterogeneity on atmosphere and land-surface interactions.

1.1. Representation of land-surface heterogeneity in numerical models

The exchanges between the land-surface and the atmosphere constitute the lower boundary condition for the atmosphere [GIORGI AND AVISSAR, 1997]. These exchanges are schematically illustrated in Fig. 1.1. The shortwave solar energy (S_{net}) is partially reflected by the surface and partially absorbed, as with the longwave radiation (L_{net}). The net radiation is either transferred to the atmosphere as sensible heat flux (H) and latent heat flux (LE) or conducted to the soil (G).

The surface energy balance is a key to the quantitative description of land-surface processes, which takes the form of

$$R_{net} + LE + H + G = 0, \quad (1.1)$$

where R_{net} is the net radiation ($R_{net} = S_{net} + L_{net}$). Besides mass and energy exchanges, momentum flux (M) is another key quantity in land-surface and atmosphere interactions as a result of friction.

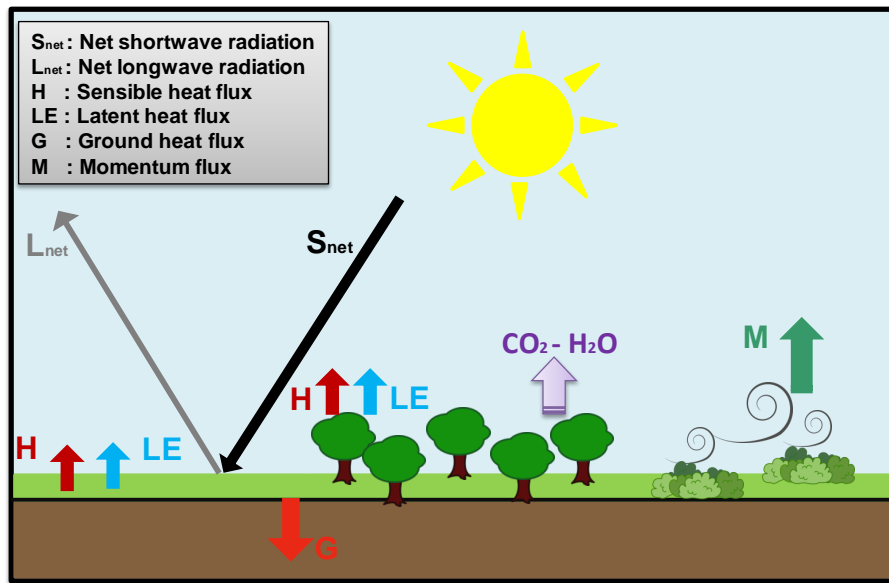


Figure 1.1.: Illustration of the surface–atmosphere interactions within the planetary boundary layer (PBL) including the exchange of energy, namely as the net shortwave radiation at the surface, S_{net} , the net longwave radiation at the surface, L_{net} , the surface sensible heat flux, H , the surface latent heat flux, LE , the ground heat flux, G ; the exchange of the momentum flux at the surface (friction), M ; the exchange of water; and the exchange of trace constituents (CO_2 , CH_4 , N_2O ,...).

Land-surface and atmosphere interactions are commonly represented using a land surface model (LSM). The first generation of LSMs, initiated by MANABE [1969], estimated the surface sensible and latent heat fluxes in climate models at minimal complexity. The complexity of the second generation LSMs increased by considering the diurnal cycle of the fluxes using the force-restore model for soil temperature and soil moisture (BHUMRAKAR [1975] and DEARDORFF [1978]). More recent versions also take into account plant canopy and more sophisticated surface soil hydrology [DICKINSON ET AL., 1993]. The third generation LSMs contemplate the plant physiology and photosynthesis. More recent implementations involve the carbon and other gaseous components of the earth system carbon cycle (e.g., OLESON ET AL. [2007]).

To explicitly consider the multi-scale heterogeneity over model grid boxes, model representation of the coupled land-atmosphere system must resort to high resolution. However, this approach is computationally expensive and hence, methods have been proposed in previous studies to parameterize heterogeneity at scales smaller than the grid, known as the subgrid-scale heterogeneity.

Earlier studies (e.g., GIORGI AND AVISSAR [1997] and SHAO ET AL. [2001]) explained the effect of subgrid-scale heterogeneous processes and divide it into two main effects: (1) the aggregation effect; and (2) the dynamic effect.

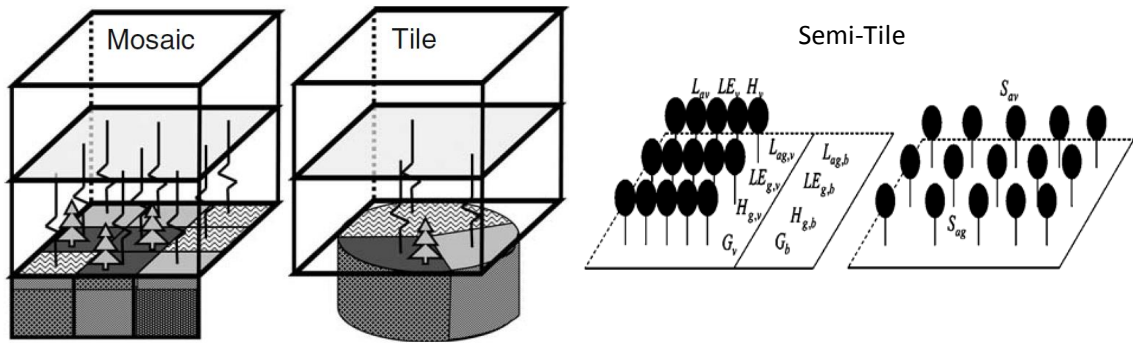


Figure 1.2.: Schematic representation of mosaic, tile (adapted from AMENT AND SIMMER [2006]), and semi-tile (adapted from NIU ET AL. [2011]) approaches. Symbols in semi-tile panel are the same as Fig. 1.1. Subscripts 'b' and 'v' denote the 'bare' and 'vegetated' area, respectively.

Aggregation effect. Since land-surface properties vary on a continuum of horizontal scales and the interactions between land-surface and atmosphere is non-linear, neglecting subgrid-scale land-surface heterogeneity or calculations with averaged, or effective parameters does not necessarily result in correct flux-estimations (e.g., LHOMME ET AL. [1994]). This effect is called the aggregation effect. The MOSAIC, TILE and semi-TILE approaches are employed to address the aggregation effect (Fig. 1.2):

The mosaic approach is proposed by AVISSAR AND PIELKE [1989]: the land-surface is subdivided into N subgrid cells smaller than the overlaid atmospheric grid (first right panel in Fig. 1.2). Each surface-subgrid is assumed to be homogeneous and the corresponding surface fluxes are calculated separately. Then, the **average** of the N subgrid fluxes at the lowest atmospheric vertical level is used as a surface-forcing for the atmospheric model.

In the tile approach, the land surface is subdivided into several tiles, e.g. according to the land-use type (second right panel in Fig. 1.2). As for a mosaic approach, all surface processes are calculated separately for each tile. The **weighted average** of the tiles fluxes is determined as the forcing for the atmosphere aloft, i.e., the weight is a portion of the land-use classes [AMENT AND SIMMER, 2006]. In comparison to the mosaic approach, the tile approach is less computationally demanding because usually the number of tiles is smaller than the number of subgrids in the mosaic approach. On the other hand, the approach lacks the effect of some surfaces type, that are not defined as a tile.

The semi-tile subgrid scheme has been proposed by NIU ET AL. [2011] (left two panels in Fig. 1.2). In that approach, the net shortwave solar radiation is first calculated over the whole surface grid, taking into account the gap probabilities (S_{av} and S_{ag} in Fig. 1.2). Then, other components of the surface energy balance are computed for two tiles: a vegetated tile and a bare tile (subscripts v and b in Fig. 1.2, respectively). The semi-tile approach has benefit over the conventional tile or "mosaic" approaches because it

calculates solar radiation independent of the solar zenith angle (SZA).

Dynamic effect. Dynamic effect occurs because land-surface heterogeneity induces circulations on various spatial scales, i.e., from mesoscale circulations to small eddies. AVISAR AND SCHMIDT [1998] and ROY ET AL. [2003] explained that, in order to simulate the dynamic effect of the mesoscale circulations, the land-surface heterogeneity must be on scales of 5-10 km. These mesoscale circulations are resolved by most modern numerical weather prediction (NWP) models [AMENT AND SIMMER, 2006] and many studies have already investigated the dynamic effects on them, e.g., MAHFOUF ET AL. [1987] and SETH AND GIORGI [1987] among many others. However, some small eddies remain unresolved depending on the model resolution.

Eddies smaller than grid cell length are named 'subgrid-scale' circulations and a range of eddies which are close to the model resolution, is defined by WYNGAARD [2004] as a gray-zone of turbulence. In fine-resolution large eddy simulation (LES) or in coarse-resolution meso-scale modeling, subgrid-scale circulations are either resolved or parameterized. However, eddies in the gray-zone [WYNGAARD [2004]; HONNERT [2019]] or on the edge of the gray-zone, i.e., low-resolution LES simulation or high-resolution meso-scale modelling, are not.

These eddies also contribute to land-atmosphere fluxes that are not accounted for in land-surface parameterizations. As a result, the organization of the convective events is often poorly represented or the estimation of surface fluxes is incorrect due to the unresolved secondary circulations. Therefore, the parameterization of the dynamic effect of subgrid-scale motion induced by land-surface heterogeneity is crucial for proper representation of land-surface–atmosphere interaction, in particular for formation and maintenance of shallow convection. The principal object of this work is these gray-zone eddies. The work covers the dynamic effect of these eddies with high resolution meso-scale modeling that is dedicated to studying interactions between land-surface heterogeneity and atmosphere.

1.2. Representation of land-surface–atmosphere interactions in numerical models

Studying the multi-scale interactions between the land-surface and the atmosphere requires four-dimensional (4D) atmospheric and land-surface data. It is difficult or even unachievable to acquire such data via field measurements for a large study area. Thus, atmospheric models coupled with the LSM come into use. The atmospheric models can be run for either an idealized (or LES) or a real case. And the LSMs can have real land-surfaces (e.g., AMENT AND SIMMER [2006]; HUANG AND MARGULIS [2010]; SHAO ET AL.

[2013]) or synthetic land-surfaces (e.g., PATTON ET AL. [2005]; HUANG AND MARGULIS [2009] ; RIECK ET AL. [2014]).

Traditionally, simplified and idealized studies are performed to understand the effects of the surface heterogeneity. For instance, HADFIELD ET AL. [1991] used one-dimensional (1D) sinusoidal heat flux as small-scale surface forcing (1.5 and 4.5 km wavelength) for free convective conditions and found that the surface heterogeneity induces organized motions into the planetary boundary layer (PBL). SHEN AND LECLERC [1995] and RAASCH AND HARBUSCH [2001] applied two-dimensional (2D) chessboard-like surface heterogeneity and found that the intensity of secondary circulations enhances when the length-scale of the land-surface inhomogeneity reaches the PBL height. In none of the above-mentioned studies is the atmospheric model component dynamically coupled to a LSM, i.e., the surface cannot respond to changes in the atmospheric state.

PATTON ET AL. [2005] were the first to study the impact of soil heterogeneity on a range of 2 to 30 km on the wet and dry PBL with dynamically coupled a LSM. They used strip-like heterogeneity and found the strongest patch-induced atmospheric motion in the range of 4-9 times the boundary layer depth. HUANG AND MARGULIS [2009] used a series of realizations replicating the mean and covariance of surface properties such as roughness length, sensible and latent heat flux and found that the sensitivity of potential temperature to surface heterogeneity is larger than that of the specific humidity. Additionally the variability of horizontal and vertical velocity clearly shows the impact of the surface inhomogeneity. RIECK ET AL. [2014] studied the impact of artificial patch-like leaf area index (LAI) surface patterns on cloud size development and found that the transition from shallow to deep convection in a simulation with heterogeneous surface is faster than the simulation with homogeneous surface and the fastest transition occurs with a patch size of 12.8 km. SHAO ET AL. [2013] modelled atmosphere–land-surface interactions over a heterogeneous surface with 60 m horizontal resolution using LES simulation. They found that there is a significant correlation between the land-SP and surface–atmosphere fluxes near the surface and the signal from the land-surface properties is detectable on the average flux up to about 650 m.

To provide new insight into the topic, the present study investigates the impact of many surface heterogeneities on the surface–atmosphere fluxes with a **real** case meso-scale atmospheric simulation, which allows the full complexity of real boundary conditions to be considered. As another aspect of the present work different from those cited earlier, the applied surface heterogeneities replicate the probability density function (PDF) of a real surface heterogeneity of an area under study from satellite data, but they exhibit different heterogeneity (structure), i.e., they are organized by a different pattern.

To understand the definition of surface heterogeneity and to quantify distinctions between

patterns, different tools are used, e.g., fractal analysis [RODRIGUEZ-ITURBE ET AL., 1995], the variogram method [GARRIGUES ET AL., 2006], the wavelet transform [BRUNSELL AND ANDERSON, 2011], the entropy spectrum [HINTZ ET AL., 2014], and the cluster analysis through a weighted average [LIU ET AL., 2017]. For the purpose of this study, a method is needed that generates many surface heterogeneities with the desired properties. The theoretical link between the fractal approach and the spectral properties of multi-dimensional fields allows a randomized-phase approach to be used to generate artificial surface patterns with controlled fractal properties (use of efficient fast Fourier transforms for the generation of artificial patterns). This approach can be tuned to yield surface patterns that resemble the multi-variate surface properties of the real surface patterns. The generated para-real surface heterogeneity is used as a lower boundary condition in a large ensemble of mesoscale atmospheric simulations, forced with lateral and upper boundary condition from a real case, and coupled with a LSM.

1.3. Research objectives

The overall goal of this thesis is to improve the understanding of the interaction between land-surface heterogeneity and the atmosphere. While the aggregation effect of the subgrid-scale heterogeneous processes is investigated by several studies, the dynamic effect is not yet properly addressed by the numerical models. Parameterizing the dynamic effect requires a better understanding of its role on surface–atmosphere exchanges. Therefore, this research aims to quantify the dynamic effect’s impact on surface–atmosphere interactions through three main inter-related coupling mechanisms between the land-surface and the atmosphere:

- **thermodynamic** coupling, i.e., energy exchange via absorption or reflection by the surface or through sensible heat flux,
- **aerodynamic** coupling, i.e., momentum exchange via friction at the surface,
- **hydrological** coupling, i.e., mass and energy exchange via water or heat transfer at the surface, namely latent and sensible heat fluxes,

A land surface has many properties, e.g., surface-albedo, surface-emissivity, LAI, surface-moisture availability, and soil-type. It is difficult to distinguish the impact of each surface property on the above mechanisms if the heterogeneity of all surface properties is considered simultaneously in the analysis.

In the face of this difficulty, a compromising approach is to choose three surface properties each of which drives a single exchange mechanism. This study focuses on the impact of these three specified properties of heterogeneity on the atmosphere. The criteria used to

select the surface properties are, first, it has to be representative of the three main surface-atmosphere exchanges (i.e., radiative, momentum and sensible/latent heat fluxes), and second, it has to be a static property. Among the surface properties that meet the above criteria, we select the following ones:

- Surface-albedo (α) as a representative of thermodynamic properties,
- Roughness-length (z_0) as a representative of mechanical properties,
- Soil-type (s_r) as a representative of hydrological properties.

Studying the impact of the heterogeneity of these surface properties on the atmosphere required running numerous simulations that are forced by a new surface heterogeneity of a single surface property; all other boundary conditions remain unchanged. The focus is on the effect of different scales of the surface heterogeneity on the atmosphere via the three main coupling mechanisms individually.

A multi-scale random fractal approach (inspired by a quasi-fractional Brownian surface) is employed to model the synthesized surface pattern with specific parameters under control. This fractal approach can model the surface pattern (SP) across all spatial scales, not only exhibiting the dominant scale but also simulating the persistency of the spatial heterogeneity. In addition, this approach can retrieve the dominant scale of surface heterogeneity holding the maximum information content and find a characteristic length scale within the entire domain that represents the spatial structure.

This study seeks to answer the following research questions under real atmospheric conditions coupled with the synthesized SP:

- 1) If land-surface heterogeneity is to be parameterized, which heterogeneity should be considered as an important surface property?
- 2) Which land-surface pattern is most important for the boundary-layer development, in particular for the formation of shallow convection?

We introduce a novel approach to address (1) and (2) as follows:

- ▶ developing a multi-scale random fractal approach for generating the land-surface heterogeneity based on the real length-scales,
- ▶ running a large ensemble of simulations forced by the heterogeneous synthesized SPs of selected surface properties,
- ▶ applying an ANalysis of VAriance (ANOVA) approach to this large ensemble and handling an ultra-large data with high performance computing (HPC),

A description of the model used, the synoptic situation, the final model setup and its validation against observations are given in Chapter 3. To attain a proper representation of

the main coupling mechanisms in the para-real ensemble runs, Section 4.1 is designed to set the stage for a case study of the para-real framework. The emphasis in Section 4.2 is on the convergence of random realizations (rr). Finally, the results of ~ 500 simulations are provided with the focus on the impact of the key coupling mechanisms on the atmospheric states (Chapter 5) and on the propagation of land-surface signal (Chapter 6). Chapter 7 presents some conclusions and directions for future work.

2. Definition of a simulation and analysis framework for surface–atmosphere interaction

In this chapter, first the concept of the **para-real** simulation—which is the core of this study—is illustrated. To study the impact of different length-scales of land-surface heterogeneity, hundreds of synthesized SPs with different spatial characteristics are generated by the fractal approach (Section 2.2). These synthesized SPs are mapped on to the real SP through some surface parameters estimated from real geodata (Section 2.3). In the last section, ANOVA method used to analyze the results is given.

2.1. Para-real simulation

The main intent in this study is to demonstrate how the land-surface heterogeneity affect the triggering surface–atmosphere coupling mechanisms (cf. Section 1.3). We aim at more firmly establishing the influence of albedo (α), soil-type (s_t), and roughness-length (z_0) on the thermodynamic, hydrological, and aerodynamic mechanisms, respectively. We would expect that albedo impacts a loss of energy from the solar irradiance, soil-type influences the availability of moisture at the surface, and roughness-length contributes to the momentum exchanges at the surface through friction. Here, the relationship between an individual selected surface property and the corresponding fluxes is more closely examined, with the aid of **para-real** simulation.

2.1.1. Simulation framework

We propose the term “para-real” for the simulations of this study because they have the full complexity of a real boundary condition except one SP at a lower boundary condition (Fig. 2.1). To isolate and eventually attribute coupling effects to physical mechanisms, we simulate individually the impact of the heterogeneity of a single surface property on the atmosphere aloft. Thus, in each simulation, the SP of only **one** of the considered surface

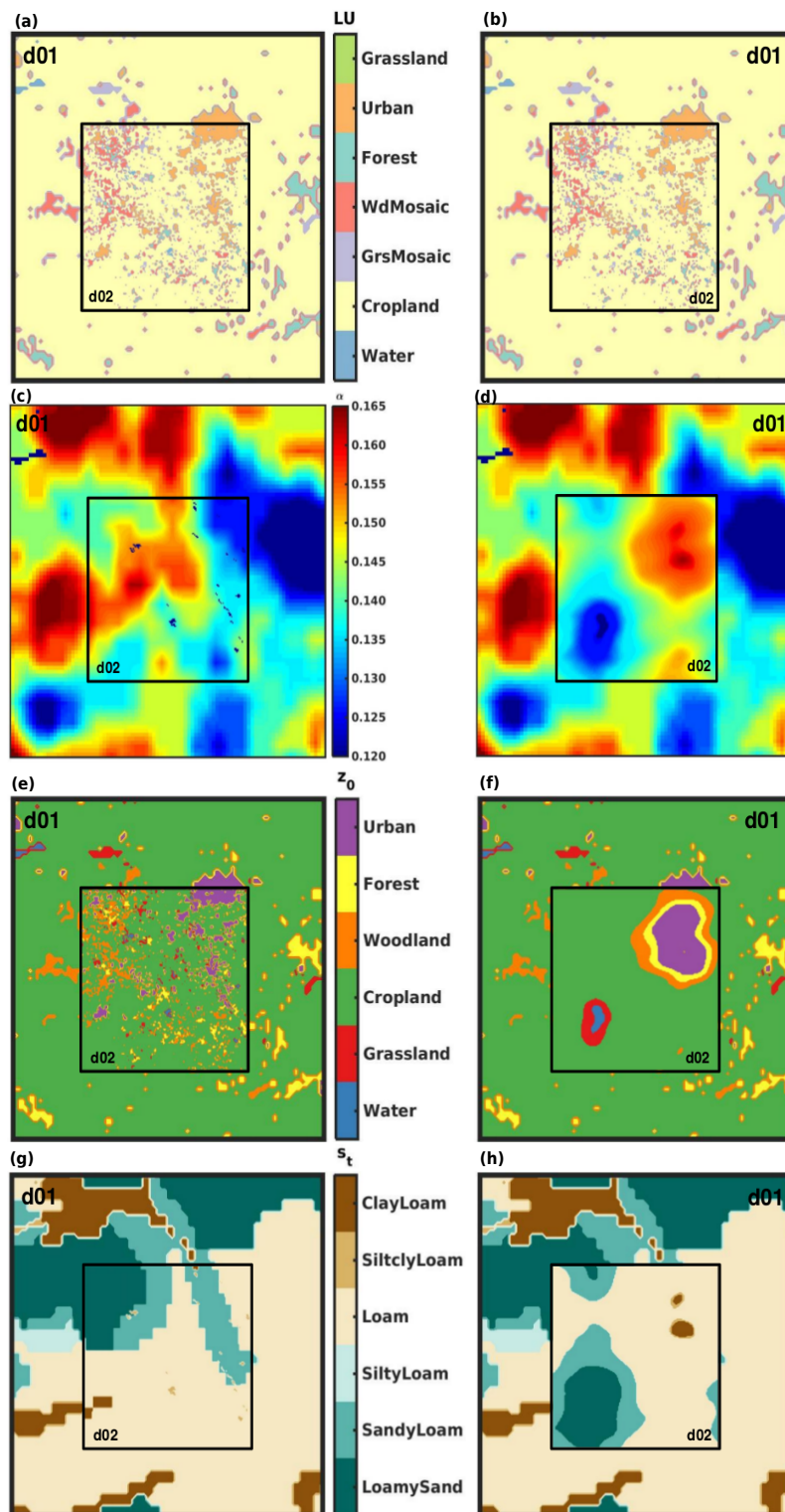


Figure 2.1.: Illustration of SPs of the specified surface properties for a real case (left column) versus a para-real case (right column). The left column shows the original SPs of two model domains. The first row (a,b) is for land-used index, the second (c,d) for albedo, third (e,f) for roughness-length, and bottom row (g,h) for soil-type. The right column shows the original SP of the outer domain (d01) and an example of the synthesized SPs of the inner domain (d02). The SPs of LU is not changed in any para-real run, and only the SP of the single specific surface property of the d02 is replaced individually by the synthesized one.

properties –albedo, soil-type, and roughness-length– is **replaced** by a synthesized one. All remaining surface-properties, in particular, the land-use index (LU) does not change in any simulation.

The synthesized SP is generated by the quasi-fractional Brownian surface (quasi-fBs) method (cf. Section (2.2.2)). The generated SP is governed by fractal parameters, known as the dominant scale of the pattern (k_{max}) and the persistency of the pattern (s_2). These two fractal parameters are tuned according to the real land-surface heterogeneity on a wide range of length-scales to generate an arbitrary number of synthesized SPs from a large-scale SP to a small-scale SP. Furthermore, as this study is focused on the quantification of the subgrid-scale dynamic effects, the generated synthesized SP replicates the PDF of the real SP of the surface property in order not to change the flux aggregation. Indeed, only the spatial arrangement of the surface properties is reshuffled.

An intermediate pattern generated by the quasi-fBs is a random 2D fractal (Fig. 2.2-c). It is converted to the synthesized SP of a selected surface property (Fig. 2.2-d) through the PDF of the real SP (Fig. 2.2-b). Thus, the synthesized SP of a specific surface property (Fig. 2.2-d) resembles the PDF of the real SP of the considered surface property (Fig. 2.2-a) but the spatial arrangement is synthetically relocated (Fig. 2.2-d).

2.1.2. Analysis framework

All analyses are provided for the three surface properties individually to show the impact of the new spatial arrangement of them on above-mentioned coupling mechanisms and consequently on corresponding atmospheric states. Since albedo and soil-type properties affect the surface energy balance through the changes of temperature and moisture, we select some atmospheric states from model output which are linked to the changes of temperature and moisture including temperature (T), water-vapor mixing ratio (QV), and cloud-water mixing ratio (QC). As wind velocity and roughness-length are inversely linked, we select wind velocity components to study the effect of the changes of the roughness-length SP on them (U , V , and W). In this way, we perceive any subgrid-scale dynamic effect of heterogeneity of a single surface property on the coupling mechanisms individually.

2.2. Synthesized surface pattern generation

Land-surface heterogeneity has been observed on a continuum and variety of horizontal scales. It can be characterized as multi-scale spatial structures with randomness features.

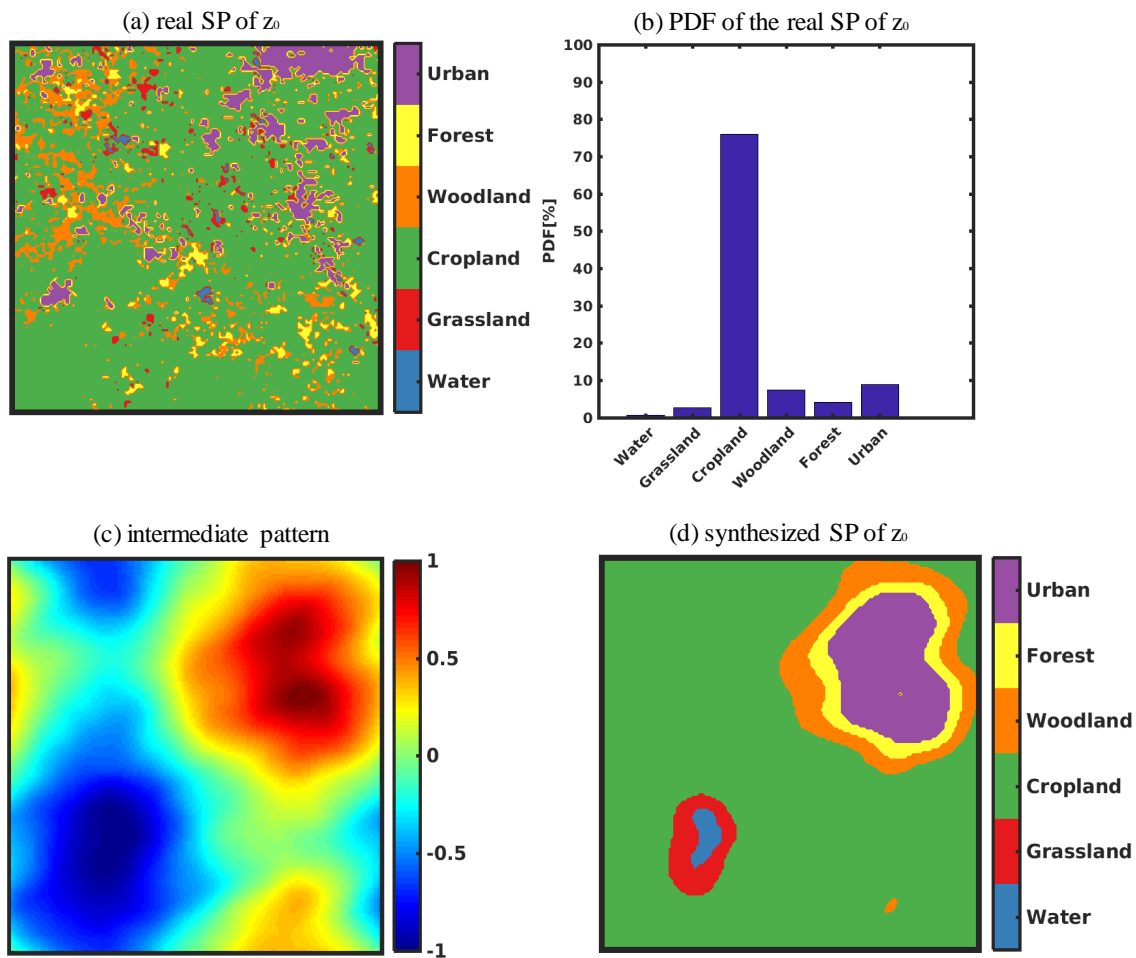


Figure 2.2.: (a) The real SP of roughness-length for a model domain under this study. (b) The PDF of (a). (c) An intermediate pattern is generated by the quasi-fBs approach. The SP of subfigure-a exhibits continuous values which are normalized between +1 and -1. (d) A synthesized SP for roughness-length. The SP of subfigure-d indicates categorical values. The intermediate pattern is converted to the synthesized SP of z_0 through the PDF of a real SP.

Since sometimes the patchiness of scales are very small (less than a kilometer), the determination of dominant scale which holds the maximum information of heterogeneity becomes problematic. Therefore, a suitable approach which is able to detect the range of scales and their correlation is required to attain a more thorough understanding of the surface spatial variations. With fractal approach, it is possible to determine the dominant length-scale, and to model a large number of heterogeneous SPs with controlled fractal properties.

2.2.1. Fractal approach

Surface heterogeneity can be characterized as 2D multi-scale random fractals. In the early 1960s, Mandelbrot worked on the fractal geometry of nature and proposed his notion of fractional Brownian motion (fBm) in his ground-breaking paper, [MANDELBROT AND VAN NESS, 1968]. He proposed to model the irregular earth surface by an extension of fBm to three dimensions. Indeed, Euclidean geometry fails to explain the complex geometric arrangement of many geophysical observables from earth topography via land-surface heterogeneity, rivers and coastlines up to clouds shapes and star clusters. Hence, the idea of fractal representation is widely used (e.g., MANDELBROT [1977]; PEITGEN AND SAUPE [1988]; BUNDE AND SHLOMO [1994]; GRAVES ET AL. [2017]). In particular, RODRIGUEZ-ITURBE ET AL. [1995] found fractal behavior in the spatial variability of soil moisture fields.

There are two categories of fractals: deterministic fractals and random fractals; most fractals in nature belong to the latter category [BUNDE AND SHLOMO, 1994]. While the dimension of deterministic fractals can be estimated by analytical methods, the dimensionality of random fractals can only be found by numerical methods [PEITGEN AND SAUPE, 1988; ABEDINI AND SHAGHAGHIAN, 2009]. Several numerical methods have been developed to estimate fractal dimension either directly, such as box counting [BLACKMORET AND ZHOU, 1998] and variogram estimation [BURROUGH, 2008], or indirectly, such as spectral analysis (e.g., MUNIANDY AND LIM [2001]; GARCÍA-SERRANA ET AL. [2018]), or detrended fluctuation analysis [GU AND ZHOU, 2006].

When using indirect methods, one assumes that the signal under study is a realization of fBm (or in 2D cases of a fractional Brownian surface (fBs)). It means the surface under consideration has a single fractal dimension (D_f). Despite a lot of success when using this assumption, some phenomena possess local fractionality which is overlooked in these methods (e.g., MUNIANDY AND LIM [2001]; ABEDINI AND SHAGHAGHIAN [2009]). Nevertheless, the basic concept of all indirect methodologies is fBm and depending on the application, fBm has been extended to higher dimensions (multifractal Brownian motions). Therefore, it is appropriate to present here some basic theories about fBm and

its properties relevant to our study according to MANDELBROT AND VAN NESS [1968].

Fractional Brownian motion (fBm)

MANDELBROT AND VAN NESS [1968] assumed $B(t)$ is an ordinary Brownian motion which has uncorrelated and independent increments, and the mean square increments have a variance proportional to the time difference, $\langle |B(t + \tau) - B(t)|^2 \rangle \propto \tau$ [BUNDE AND SHLOMO, 1994]. They defined a fractional Brownian motion of exponent H , $B_H(t)$ as

$$B_H(t) = \frac{1}{\Gamma(H + \frac{1}{2})} \left\{ \int_{-\infty}^0 [(t-s)^{H-1/2} - (-s)^{H-1/2}] dB(s) + \int_0^t (t-s)^{H-1/2} dB(s) \right\}, \quad (2.1)$$

where Γ is a gamma function and $dB(s)$ is a Wiener process. Both integrals on the right hand side of equation (2.1) are a stochastic integral due to the fact that $dB(s)$ is a stochastic process and it evolves probabilistically in time [GARDINER, 2004].

The parameter H satisfies $0 < H < 1$, and it is called *Hurst exponent*¹. In the one dimensional case, it is restricted into three classes: $H < 1/2$ for relatively rough times series, $H = 1/2$ for ordinary Brownian motions and $H > 1/2$ for relatively smooth time series.

The increments of fBm have two main properties: (1) The stochastic differential dB_H is a stationary and isotropic Gaussian process with the mean of $\langle B_H(t + \tau) - B_H(t) \rangle = 0$ and the variance of $\langle |B_H(t + \tau) - B_H(t)|^2 \rangle \propto \tau^{2H}$. (2) dB_H is statistically self-similar, i.e., if τ is rescaled by a factor of b , dB_H is changed by a factor of b^H . In other words, $B_H(t + \tau) - B_H(t)$ and $b^{-H}[B_H(t + b\tau) - B_H(t)]$ are statistically similar.

By extending self-similarity to $E \in \mathbb{N}$ dimensions, the general scaling relation is

$$\langle |B_H(\vec{r}_2) - B_H(\vec{r}_1)|^2 \rangle \propto |\vec{r}_2 - \vec{r}_1|^{2H} \quad (2.2)$$

where $\vec{r} = (r_1, \dots, r_E)$ and E indicates the dimension of the fractional Brownian signal, e.g. at time-series ($E=1$), a landscape ($E=2$), or a cloud ($E=3$). For $E=2$, \vec{r} can be replaced by the xy -plane, then $B_H(x, y)$ can be considered as the surface property (for example altitude) and equation (2.2) simplifies to $\langle |B_H(x_2, y_2) - B_H(x_1, y_1)|^2 \rangle \propto \Delta r^{2H}$ where $\Delta r = \sqrt{\Delta x^2 + \Delta y^2}$. This means $B_H(x, y)$ is scale invariant along the x and y dimensions, and it is isotropic. The resulting surface is indistinguishable by zooming in or out. If $B_H(x, y)$ varies anisotropically along x and y by rescaling, it is known as *self-affinity*. Indeed, many fractals in nature are self-affine [MANDELBROT, 1977; PEITGEN AND SAUPE, 1988; BUNDE AND SHLOMO, 1994].

¹In the literatures H is referred to various expressions: the 'self-similarity parameter', the 'long memory parameter', the 'Hurst coefficient', the 'Hurst parameter' and the 'fractional Brownian motion parameter'.

The seemingly complex form of the irregular manifolds that result from fractal Brownian process, is characterized by a fractal dimension D_f which relates to the Hurst exponent H via

$$D_f = E + 1 - H \quad (2.3)$$

there, $E < D_f < E + 1$. D_f is a measure of the irregularity in a fractal. For instance, in case of a mountainous area $E = 2$ and its D_f is limited to $2 < D_f < 3$. When $D_f = 2$, the area is extremely smooth. As D_f increases, the area becomes increasingly corrugated [MANDELBROT, 1977]. The area of high Earth mountains can be resembled with $2.5 < D_f < 3$. Ultimately, when $D_f = 3$, the whole 3D space is filled as a consequence of dense point to point jumps in altitude covering the entire 2D space on which the process is defined.

Spectral densities for fBm

We consider now the generation of a Brownian process through a Fourier-Spectral approach. For illustrative purpose, we resort to the 1D case, i.e., fractional Brownian motion, $B_H(t)$. The Fourier transform of $B_H(t)$ is defined as

$$\hat{B}_H(f) = \int_{-\infty}^{\infty} B_H(t) e^{-i2\pi ft} dt, \quad (2.4)$$

where, $f \in \mathbb{R}_+$ is the frequency. According to Parseval's theorem [BUTTKUS, 2000], the total energy ξ_S obeys

$$\xi_S = \int_{-\infty}^{\infty} |B_H(t)|^2 dt = \int_{-\infty}^{\infty} |\hat{B}_H(f)|^2 df. \quad (2.5)$$

We hence can associate the magnitude of the Fourier transform to the amount of energy located at a particular discrete frequency with the power spectral density $|\hat{B}_H(f)|^2$. $\hat{B}_H(f)$ is given as $\hat{B}_H(f) = |\hat{B}_H(f)|(\cos \Theta + i \sin \Theta) = |\hat{B}_H(f)|e^{i\Theta(f)}$. A power spectrum of the form $1/f^\beta$ corresponds to the fBm with $H = (\beta - 1)/2$ [PEITGEN AND SAUPE, 1988]. As H is restricted between 0 and 1 for the fBm, $1 < \beta < 3$ is for 1D problems. Accordingly the fractal dimension of the corresponding process is linked to β by

$$D_f = E + 1 - H = E + \frac{3 - \beta}{2}. \quad (2.6)$$

For isotropic problems of higher dimensions, we consider radial wave numbers, $f_r = \sum_{i=1}^E f_i^2$, and the spectral slope, β , is linked to the Hurst exponent and dimensionality of the problem as

$$\hat{B}_H(f_1, f_2, \dots, f_E) \propto \frac{1}{(\sqrt{f_1^2 + f_2^2 + \dots + f_E^2})^{2H+E}} = \frac{1}{(\sum_{i=1}^E f_i^2)^{\frac{\beta+E-1}{2}}} \quad (2.7)$$

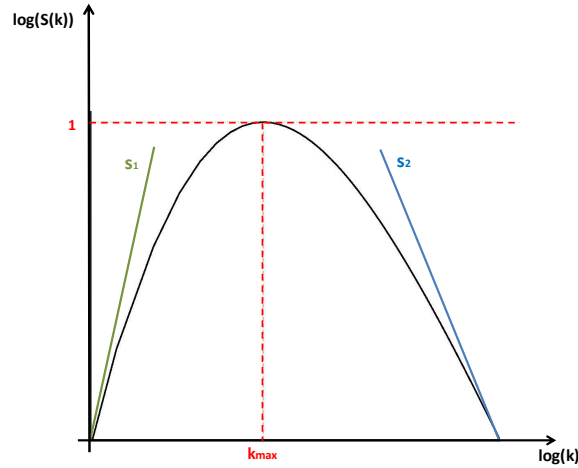


Figure 2.3.: Schematic of equation (2.9) in loglog scale with $s_1 = 4$ and $s_2 = 1.5$ which is normalized at the maximum of k .

then \hat{B}_H of fractional Brownian surface (fBs) is proportional to $(f_x^2 + f_y^2)^{-(\beta+1)/2}$.

2.2.2. Quasi fractional Brownian surface (quasi-fBs)

We describe now, how these general properties of Brownian processes can be inverted to obtain a random surface with defined fractal properties as a realization of a Brownian process. We start from equation (2.7) and mimic the fBs power spectrum by imposing a slope $s_2 \in \mathbb{R}_+$ in the limit of $k \rightarrow \infty$. This yields

$$\lim(|\hat{B}_H|)_{k \rightarrow \infty} = \frac{1}{k^{s_2}} \quad (2.8)$$

where $k \in \mathbb{R}_+$ is the wave number. The slope s_2 indicates long term memory of the signal and shows how far patterns are correlated in the domain, or in other words, how persistent a variance signal is across the spectral space. Small s_2 indicates a high persistence and a large s_2 means that the small features of the pattern vanish and patterns look more clustered.

The relation (2.8), however, implies $|\hat{B}_H(k)| \rightarrow \infty$ as $k \rightarrow 0$ which is not desired. To control the variance of the fractals at large scales, we impose a second slope $s_1 \in \mathbb{R}_+$ as $k \rightarrow 0$ by letting

$$|\hat{B}_H(k)| = N \frac{k^{s_1}}{(1+k)^{s_1+s_2}}. \quad (2.9)$$

The slope s_1 now indicates the decay of the signal in the frequency space as large wavelength is approached. $N \in \mathbb{R}$ is a normalization factor and k is shifted with respect to reference wave number $k = k'/k_0$. The power spectrum then acquires the shape shown schematically in Fig. 2.3. This approach is named *quasi*-fBs to reflect the fact that its

power spectrum diverts from a pure fractal shape as $k \rightarrow 0$. Further, the slope s_2 which is analogous to β , is not strictly limited to the same interval as β . Consequently, many 2D fractals with a wide range of D_f can be generated by this approach.

It is crucial to know on which length scale the maximum of the power spectrum occurs. k_{max} is the wave number that corresponds to the dominant scale which holds the maximum energy of the power spectrum $d|\hat{B}_H(k)|/dk = 0$. We define a reference wave number as $k_0 = (s_2/s_1)k_{max}$ and use it for normalizing the spectrum with respect to the k_{max} . Besides, N is defined as²

$$N^{-1} = |\hat{B}_H|(k_{max}) = - \left(\frac{s_2}{s_1 + s_2} \right)^{s_1 + s_2} \left(\frac{s_1}{s_2} \right)^{s_1}. \quad (2.10)$$

The maximum of the spectral density is always unity by this normalization. Further, k_{max} is the scale parameter determining the number of structures per dimension.

By approximating equation (2.9), $|\hat{B}_H(k)| \propto 1/(k_x^2 + k_y^2)^{s_2}$ is analogous to $|\hat{B}_H(f)| \propto 1/(f_x^2 + f_y^2)^{\frac{\beta+1}{2}}$ according to the expression 2.7. If $1 < \beta < 3$, fBs is generated. Correspondingly, if $1 < s_2 < 2$, fBs is obtained. Out of this range, the generated fractals are not fractional Brownian surfaces rather multi-scale 2D fractals.

Equation (2.9) has three parameters (i.e., s_1 , s_2 and k_{max}) characterizing the spectrum of the quasi-fBs. For the sake of simplicity, we keep s_1 constant and vary s_2 and k_{max} in a reasonable range according to the original geodata from WRF (more detail is given in Section 2.3). Arbitrary synthesized SPs can be generated for each power spectrum defined by s_2 and k_{max} through phase randomization as explained below.

Generation of quasi-fBs by phase randomization

Step 1. Create the spectrum $\hat{B}_H(k_{xy})$ according to equation (2.9).

First, a set of 2D wave number k_{xy} is generated as $k_{xy} = \sqrt{k_x^2 + k_y^2}$ where $k_x = k_y = 0, 1, 2, \dots, n/2$. n is the size of the multi-scale fractal field. Then, we impose equation (2.9) to the amplitude of spectrum together with Gaussian random perturbation across the radial wavenumber. For this random perturbation, we use a particular implementation of Gaussian noise that forces exact conservation of mean and variance for every 2 consecutive numbers. We also perturb the phase of the spectrum by a set of random numbers between 0 and 2π ($0 < \Theta_{xy} < 2\pi$). As a result of this step, we obtain the randomized spectrum of multi-scale 2D fractal, $\hat{B}_H(k_x, k_y) = |\hat{B}_H(k_{xy})|e^{i\Theta_{xy}}$.

Step 2. Compute the inverse Fourier transform of $\hat{B}_H(k_x, k_y)$.

²Or it is defined as $N^{-1} = \int_0^\infty |\hat{B}_H(k)|^2 dk = n \frac{\Gamma(s_1)}{\Gamma(1+s_1)\Gamma(s_2-(1+s_1))}$ to govern the total variance, and it exists under following condition $1 + s_1 > 0$ and $s_2 > 1 + s_1$.

Figures 2.4 illustrates the quasi-fBs method. The 2D patterns contain the 2D quasi-fBs realization and the corresponding power spectrum. In subfigures (a), (b), and (c), s_1 and k_{max} are kept constant and s_2 varies from 3 to 0.5. By decreasing slope ($|s_2|$) from left to right, the pattern becomes less and less persistent (more randomized). In subfigures (d), (e), and (f), s_1 and s_2 are kept constant and k_{max} varies from 10 to 1. By decreasing k_{max} from left to right, the pattern is less randomized and more clustered.

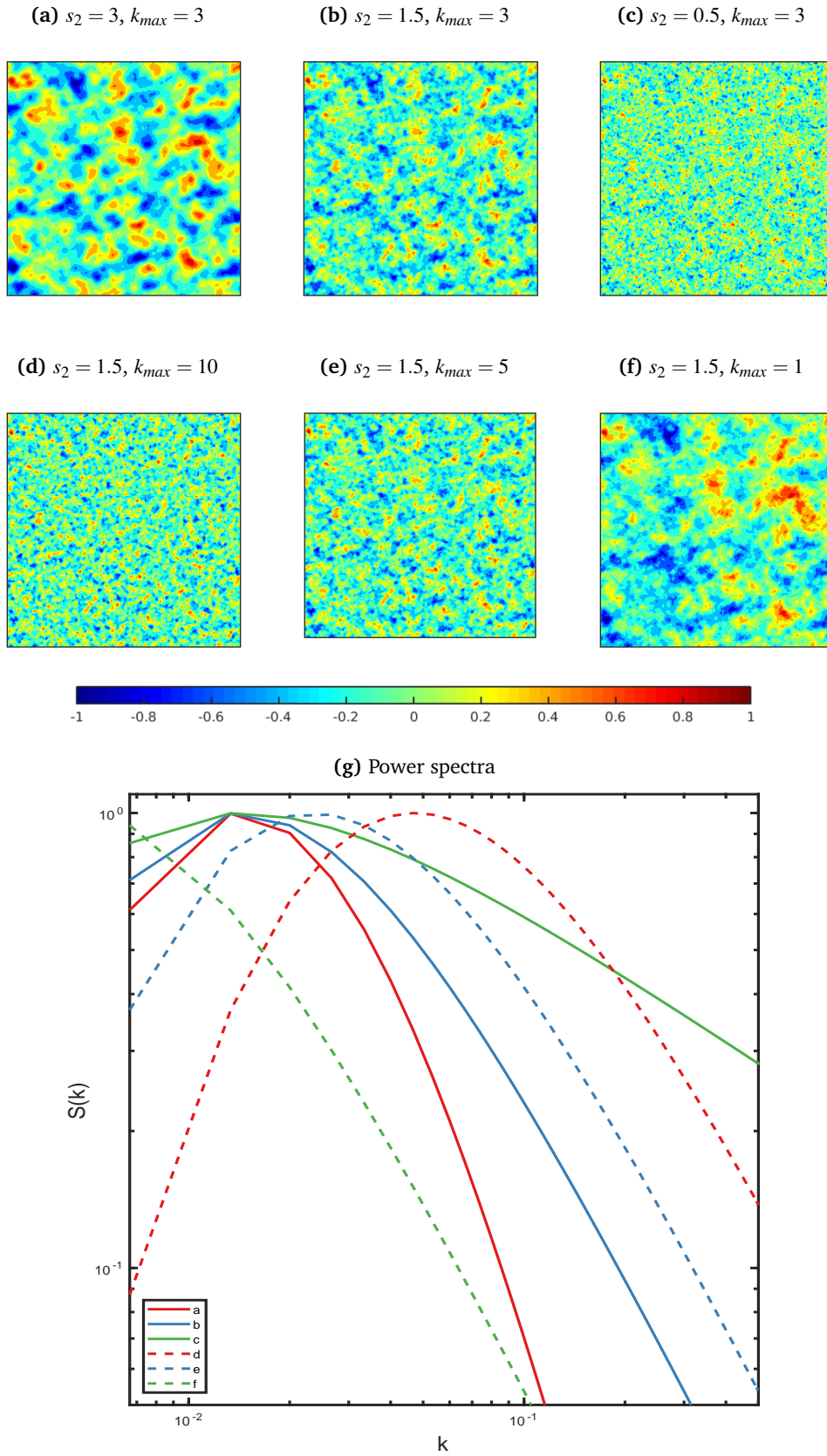


Figure 2.4.: Plots (a)-(f) illustrate fields generated by quasi-fBs approach in xy-plane with $n = 150$ points and $s_1 = 4$. Plot (g) shows the corresponding power spectra.

2.3. Estimation of scales from original geo-SPs

To acquire an estimate of the parameters s_2 and k_{max} of the spectrum used for generating the quasi-fBs, we consider the SP of the original geo-data of WRF input files. We use the original SPs of three surface properties (α , z_0 , s_t) from USGS WPS geo-data. In order to make sure that we arrive at a representative estimate and also to reduce noise in spectral estimates from a single sample, we use 25 domains arranged as shown in table 2.1. In terms of the radial power spectra, we find that overall slope among different domains is quite similar (Fig. 2.5). Figure 2.5 indicates the power spectra of the original SP of α for 25 domains and the best linear fit to them.

Table 2.1.: Location of the center of 25 domains.

Longitude ($^{\circ}$ E)	5.0	5.5	6.4	7.0	7.5
Latitude ($^{\circ}$ N)	49.5	50.0	50.9	51.5	52.0

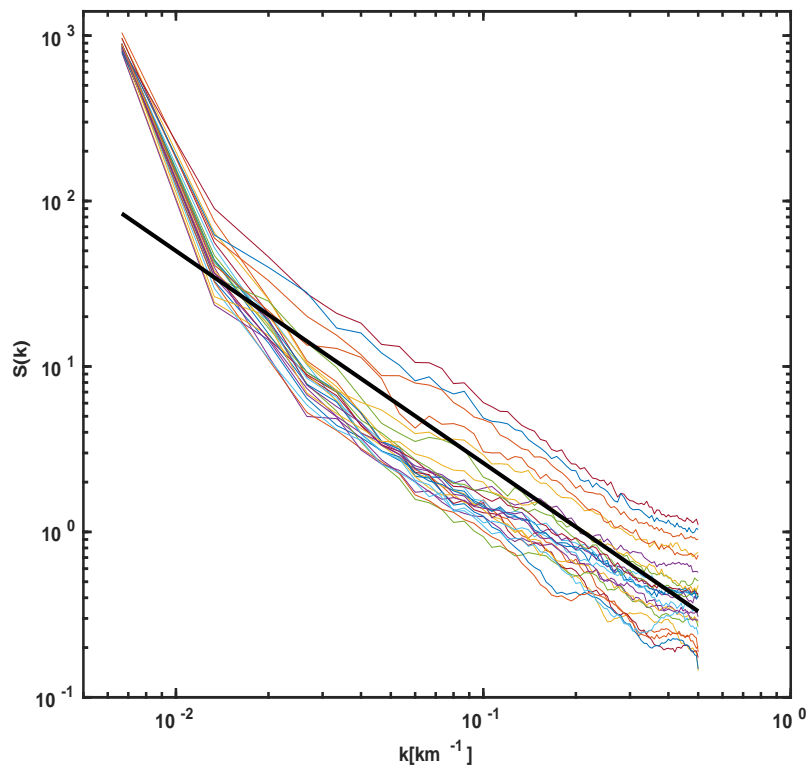


Figure 2.5.: Power spectrum of α for the 25 domains given in table 2.1 (colored curves) with the best linear fit curve (solid black curve).

The same calculation is done for the original SPs of z_0 and s_t . From the power spectra of original SPs, s_2 is estimated for α , z_0 , and s_t at 1.3, 0.8, and 1.5, respectively. And based on

that, a logical range of s_2 and k_{max} is proposed in table 2.2 for generating 16 intermediate SPs (Fig. 2.6). These intermediate SPs are the basis of the final synthesized SPs for each of the surface properties of interest (cf. Section 2.1).

Table 2.2.: Proposed range of s_2 and k_{max} based on the estimation from original SPs.

s_2	1.3	1.8	2.4	3
k_{max} [km^{-1}]	0.1	0.5	1	3

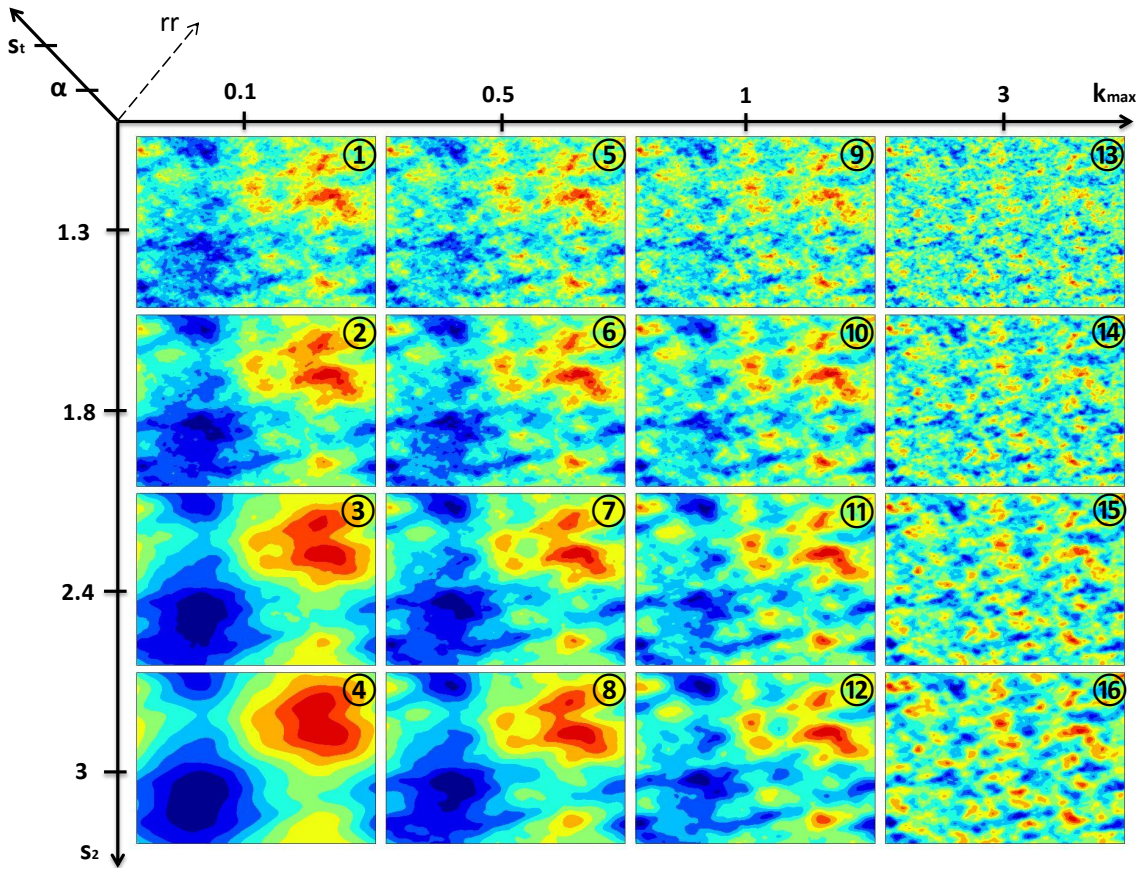


Figure 2.6.: Intermediate SPs according to estimations in table 2.2. Numbers assigned to each SP are used in chapter 4, 5, and 6 for the sake of easier discussions.

2.4. Analysis approach

Analysis of Variance (ANOVA) has historically been applied in different research areas to study the deviation of data from its mean [RUTHERFORD, 2011]. ANOVA decomposition was revealed as far back 1948 by Hoeffding and is widely used in determining what portion of total variation is explained by lower-order variations [Hooker, 2007]. A common

formulation for ANOVA-decomposition is that by SOBOL [1993].

In high dimensional models, quite often a small group of input variables can represent the main effects on independent-multivariate outputs [SOBOL, 1993]. ANOVA decomposition renders a family of subsets of multivariate functions that each subsets contains the information about the variations along the dimensions of corresponding subset. Thus, this family of subsets can approximate the model outputs.

Since we want to inquire to what extent atmospheric data depends on land-surface properties and in particular on the spatial arrangement (e.g. cloud distribution is influenced by land-surface induced flows [GARCIA-CARRERAS ET AL., 2011].), ANOVA method is applied. Our hypothesis is that the decomposed ANOVA components can elucidate the signal from the SP in the atmospheric state variables at different heights.

2.4.1. The classic ANOVA method

Let $F(x) : I^n \rightarrow \mathbb{R} : x \mapsto F(x)$ be a multivariate function and suppose F is square integrable in Hilbert space where I^n indicates the unit hypercube in n dimensions:

$$F(x) = f_\emptyset + \sum_{i=1}^n f_i(x_i) + \sum_{i \neq j} f_{ij}(x_i, x_j) + \dots, \quad (2.11)$$

where f_\emptyset is a constant mean and the summand terms denote the first order effects on total variations, the second order effects, and so on [HOOKER, 2007]. For the sake of notational brevity, let u denote a subset of indices with $u \subseteq D$ where $D := \{1, \dots, n\}$, then the expression (2.11) reads as

$$F(x) = \sum_{u \subseteq \{1, \dots, n\}} f_u(x_u). \quad (2.12)$$

The decomposed components $f_u(x_u)$ are defined as

$$f_u(x_u) := P_u(x_u) - \sum_{v \subset u} f_v(x_v), \quad (2.13)$$

where, v are subsets within the u -subspace that account for lower-order effects. $P_u(x_u)$ is the projection of $F(x)$ in the subspace excluding u -subspace and defined as:

$$P_u(x_u) := \int_{x_{-u}} F(x) dx_{-u}, \quad (2.14)$$

x_{-u} indicates variables with indices not in u -subspace.

Since all variation in the subspace with dimension v are removed from the multivariate function F , each ANOVA component indicates the pure contribution of the subspace containing the dimension u to the total variance. The total number of decomposed ANOVA

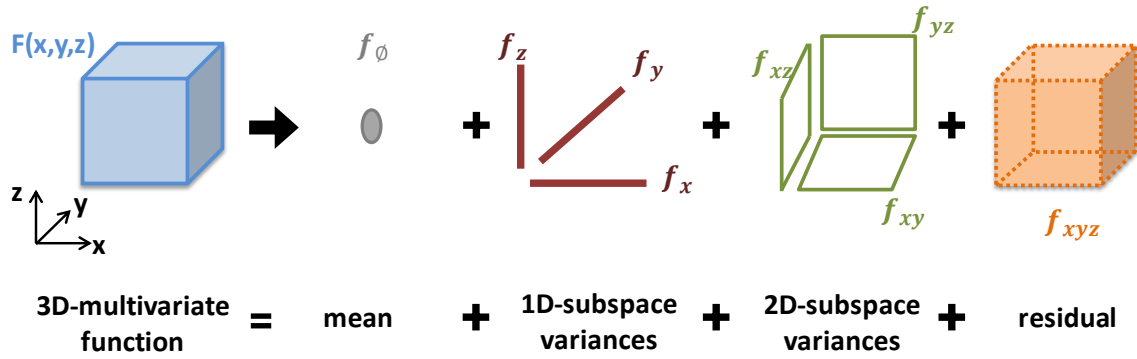


Figure 2.7.: Schematic of ANOVA decompositions for a 3D-multivariate function.

components is 2^n .

Representation 2.11 is called 'classic' ANOVA³ and it implies the following fundamental properties:

- zero means: $\int f_u(x_u) dx_u = 0$ for each $u \neq \emptyset$,
- orthogonality: $\int f_u(x_u) f_v(x_v) dx = 0$ for $u \neq v$,
- variance decomposition: $D_u := \sigma_u^2 := \int f_u(x_u)^2 dx_u$ and $\sum D_u = \sigma^2 := \int F^2(x) dx - f_0^2$

The last property implies the *Global Sensitivity Index* (S_u)

$$S_u := D_u/D, \quad (2.15)$$

which gives the contribution of the variance in subspace u to the total variance. As the variance is additive, the two equalities $\sum_{u \subseteq D} D_u = D$ and $\sum_{u \subseteq D} S_u = 1$ can be obtained.

Figure 2.7 schematically describes how a 3D-multivariate function is decomposed into its lower-order variances by ANOVA.

2.4.2. Application

Most model outputs under this study are 4D-multivariate functions. Thus, a 4D-ANOVA decomposition is demonstrated here. Let $F \equiv F(x, y, z, t)$ be a function of longitude (x), latitude (y), altitude (z) and time (t), the corresponding ANOVA decomposition is obtained by two steps:

Step 1. calculate the projections $P_u(x_u)$:

$$P_{xyzt}(x, y, z, t) := F(x, y, z, t),$$

³alternatively it is called 'functional' ANOVA [HOOKER, 2007].

$$\begin{aligned}
P_{xyz}(x, y, z) &:= \int F(x, y, z, t) dt, \\
P_{xyt}(x, y, t) &:= \int F(x, y, z, t) dz, \\
P_{yzt}(y, z, t) &:= \int F(x, y, z, t) dx, \\
P_{xzt}(x, z, t) &:= \int F(x, y, z, t) dy, \\
P_{xy}(x, y) &:= \iint F(x, y, z, t) dz dt, \\
P_{xz}(x, z) &:= \iint F(x, y, z, t) dy dt, \\
P_{xt}(x, t) &:= \iint F(x, y, z, t) dy dz, \\
P_{yz}(y, z) &:= \iint F(x, y, z, t) dx dt, \\
P_{yt}(y, t) &:= \iint F(x, y, z, t) dx dz, \\
P_{zt}(z, t) &:= \iint F(x, y, z, t) dx dy, \\
P_x(x) &:= \iiint F(x, y, z, t) dy dz dt, \\
P_y(y) &:= \iiint F(x, y, z, t) dx dz dt, \\
P_z(z) &:= \iiint F(x, y, z, t) dx dy dt, \\
P_t(t) &:= \iiint F(x, y, z, t) dx dy dz, \\
P_\emptyset(\emptyset) &:= \iiint F(x, y, z, t) dx dy dz dt.
\end{aligned} \tag{2.16}$$

Step 2. calculate ANOVA decompositions $f_u(x_u)$:

$$\begin{aligned}
f_\emptyset(\emptyset) &:= P_\emptyset(\emptyset), \\
f_x(x) &:= P_x(x) - f_\emptyset(\emptyset) = P_x(x) - P_\emptyset(\emptyset), \\
f_y(y) &:= P_y(y) - f_\emptyset(\emptyset) = P_y(y) - P_\emptyset(\emptyset), \\
f_z(z) &:= P_z(z) - f_\emptyset(\emptyset) = P_z(z) - P_\emptyset(\emptyset), \\
f_t(t) &:= P_t(t) - f_\emptyset(\emptyset) = P_t(t) - P_\emptyset(\emptyset), \\
f_{xy}(x, y) &:= P_{xy}(x, y) - f_x(x) - f_y(y) - f_\emptyset(\emptyset) \\
&= P_{xy}(x, y) - P_x(x) - P_y(y) + P_\emptyset(\emptyset), \\
f_{xz}(x, z) &:= P_{xz}(x, z) - f_x(x) - f_z(z) - f_\emptyset(\emptyset) \\
&= P_{xz}(x, z) - P_x(x) - P_z(z) + P_\emptyset(\emptyset), \\
f_{xt}(x, t) &:= P_{xt}(x, t) - f_x(x) - f_t(t) - f_\emptyset(\emptyset) \\
&= P_{xt}(x, t) - P_x(x) - P_t(t) + P_\emptyset(\emptyset),
\end{aligned}$$

$$\begin{aligned}
f_{yz}(y, z) &:= P_{yz}(y, z) - f_y(y) - f_z(z) - f_{\emptyset}(\emptyset) \\
&= P_{yz}(y, z) - P_y(y) - P_z(z) + P_{\emptyset}(\emptyset), \\
f_{yt}(y, t) &:= P_{yt}(y, t) - f_y(y) - f_t(t) - f_{\emptyset}(\emptyset) \\
&= P_{yt}(y, t) - P_y(y) - P_t(t) + P_{\emptyset}(\emptyset), \\
f_{zt}(z, t) &:= P_{zt}(z, t) - f_z(z) - f_t(t) - f_{\emptyset}(\emptyset) \\
&= P_{zt}(z, t) - P_z(z) - P_t(t) + P_{\emptyset}(\emptyset), \\
f_{xyz}(x, y, z) &:= P_{xyz}(x, y, z) - f_{xy}(x, y) - f_{yz}(y, z) - f_{xz}(x, z) - f_x(x) - f_y(y) - f_z(z) - f_{\emptyset}(\emptyset) \\
&= P_{xyz}(x, y, z) - P_{xy}(x, y) - P_{yz}(y, z) - P_{xz}(x, z) + P_x(x) + P_y(y) + P_z(z) - P_{\emptyset}(\emptyset), \\
f_{xyt}(x, y, t) &:= P_{xyt}(x, y, t) - f_{xy}(x, y) - f_{yt}(y, t) - f_{xt}(x, t) - f_x(x) - f_y(y) - f_t(t) - f_{\emptyset}(\emptyset) \\
&= P_{xyt}(x, y, t) - P_{xy}(x, y) - P_{yt}(y, t) - P_{xt}(x, t) + P_x(x) + P_y(y) + P_t(t) - P_{\emptyset}(\emptyset), \\
f_{xzt}(x, z, t) &:= P_{xzt}(x, z, t) - f_{xz}(x, z) - f_{zt}(z, t) - f_{xt}(x, t) - f_x(x) - f_z(z) - f_t(t) - f_{\emptyset}(\emptyset) \\
&= P_{xzt}(x, z, t) - P_{xz}(x, z) - P_{zt}(z, t) - P_{xt}(x, t) + P_x(x) + P_z(z) + P_t(t) - P_{\emptyset}(\emptyset), \\
f_{yzt}(y, z, t) &:= P_{yzt}(y, z, t) - f_{yz}(y, z) - f_{yt}(y, t) - f_{zt}(z, t) - f_y(y) - f_z(z) - f_t(t) - f_{\emptyset}(\emptyset) \\
&= P_{yzt}(y, z, t) - P_{yz}(y, z) - P_{yt}(y, t) - P_{zt}(z, t) + P_y(y) + P_z(z) + P_t(t) - P_{\emptyset}(\emptyset), \\
f_{xyzt}(x, y, z, t) &:= P_{xyzt}(x, y, z, t) - f_{xyz}(x, y, z) - f_{xyt}(x, y, t) - f_{xzt}(x, z, t) - f_{yzt}(y, z, t) \\
&\quad - f_{xy}(x, y) - f_{xz}(x, z) - f_{xt}(x, t) - f_{yz}(y, z) - f_{yt}(y, t) - f_{zt}(z, t) \\
&\quad - f_x(x) - f_y(y) - f_z(z) - f_t(t) \\
&\quad - f_{\emptyset}(\emptyset) \\
&= F(x, y, z, t) - P_{xyz}(x, y, z) - P_{xyt}(x, y, t) - P_{xzt}(x, z, t) - P_{yzt}(y, z, t) \\
&\quad + P_{xy}(x, y) + P_{xz}(x, z) + P_{xt}(x, t) + P_{yz}(y, z) + P_{yt}(y, t) + P_{zt}(z, t) \\
&\quad - P_x(x) - P_y(y) - P_z(z) - P_t(t) \\
&\quad + P_{\emptyset}(\emptyset).
\end{aligned}
\tag{2.17}$$

3. Model setup and case description

To better understand the propagation of the land-surface pattern into the atmosphere on various scales, we use a real case forced by a real lateral atmospheric situation (i.e., high-resolution reanalysis atmospheric data) coupled with LSM. The boundary conditions of the LSM in a reference run are real and all SPs are original from geo-data. In para-real ensemble runs, one single SP of three identified surface properties is replaced by a synthetic one and the rest SPs are real from original geo-data. To resolve the aggregation effect of land-surface heterogeneity, the LSM of the current model uses the semi-tile scheme.

We commence by describing the numerical simulation framework, namely WRF in its Advance Research WRF (ARW) version. Second, the synoptic situation for the studied days April 24-26, 2013 is described. Third, the reference model setup including all implemented modifications to achieve a high-resolution representation of shallow convection and to detect short and long-term soil responses are provided. The last section validates the model setup against observation and reanalysis data.

3.1. The Weather Research and Forecasting (WRF) model

The Weather Research and Forecasting model (WRF) version 3.7.1 is used for this study to produce simulations based on real atmospheric conditions. A detailed description of the WRF model can be found in [SKAMAROCK ET AL., 2008].

WRF consists of several components designed for both research and operational applications. Figure 3.1 shows the procedure for a real case. Each real forecast starts with the WRF Preprocessing System (WPS) preparing the WRF input files and WRF boundary files. In WPS, the static terrestrial data is extracted from different sources of geo-data according to defined model domains within *geogrid.exe*, and the gridded meteorological data is encoded within *ungrib.exe*. In *geogrid*, geodata is extracted, projected according to chosen coordinate system and horizontally interpolated. The last step in WPS is to horizontally merge the output from *geogrid* and *ungrib* programs by *metgrid.exe*. The vertical interpolation is done by *real.exe* where the vertical levels can be changed depending on the model resolution. After *real.exe*, WRF initial input files and WRF boundary files are ready to be given to the dynamic solver WRF (here ARW is used).

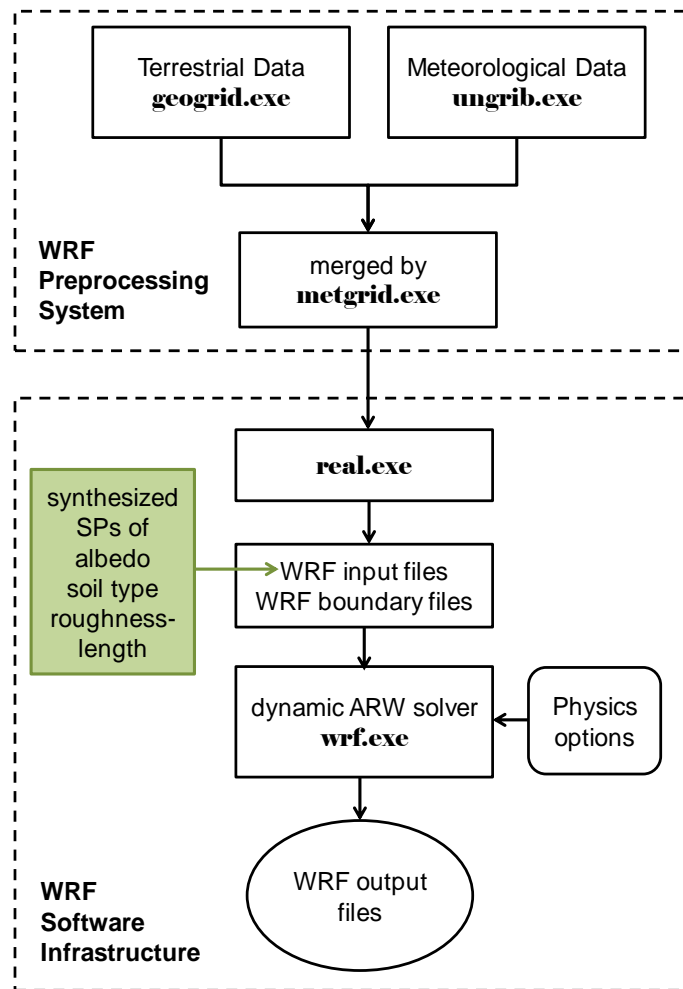


Figure 3.1.: WRF system flowchart for a real simulation including the WPS and the ARW solver. The green rectangle indicates an extra step in this study to replace the original SP with a synthesized SP.

3.1.1. Model discretization

Temporal discretization. The ARW solver uses a third-order Runge-Kutta (RK3) time integration scheme for low-frequency (or meteorologically significant) modes [WICKER AND SKAMAROCK, 2002] and applies a time-split integration scheme for high-frequency (acoustic waves and meteorologically insignificant) modes [KLEMP ET AL., 2007], since high-frequency acoustic modes severely limit the model time step in RK3 scheme.

Spatial discretization. The ARW dynamical core solves the compressible, non-hydrostatic Euler equations using a terrain-following hydrostatic pressure vertical coordinate system

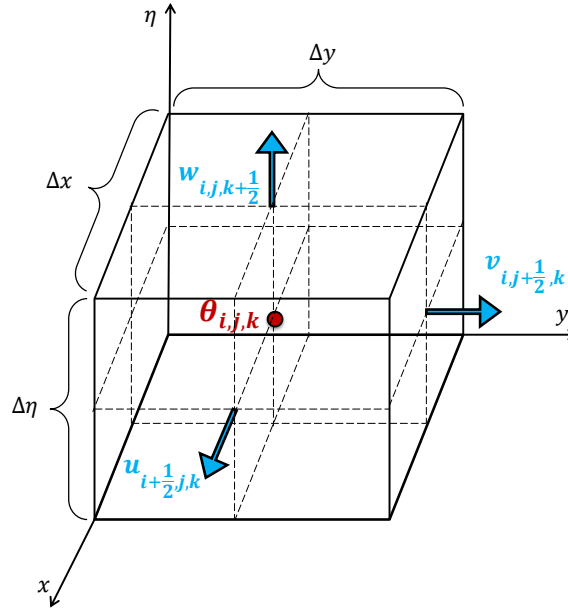


Figure 3.2.: Horizontal and vertical grids of the WRF ARW. Red circle at the center of grid indicates mass point.

represented by η and proposed by LAPRISE [1992] as

$$\eta = \frac{p_h - p_{ht}}{\mu}, \quad (3.1)$$

where $\mu = p_{hs} - p_{ht}$. p_h is the hydrostatic component of the pressure. μ is the difference between the pressure at the surface (p_{hs}) and the pressure at the top boundary (p_{ht}). This vertical coordinate definition is commonly known as σ -coordinate. η varies between 1 at the surface and 0 at the top boundary.

Spatial discretization is shown in Fig. 3.2 and obtained by the finite difference scheme using the Arakawa C-grid staggering [ARAKAWA AND LAMB, 1977]. Diagnostic variables, pressure and inverse density are computed at mass points (the location of θ in Fig. 3.2) and the wind vector components are staggered and computed at half-levels. w is staggered only in k and u and v components of wind are staggered horizontally. Δx and Δy are constant whereas $\Delta\eta$ can change with height and horizontally.

Stability constraint. The model time step in RK3 scheme is limited by the advective Courant¹ number. WICKER AND SKAMAROCK [2002] provide a table for the maximum stable Courant number (Cr_{max}) for 1D linear advection in the RK3 scheme depending on

¹The Courant-Friedrichs-Lewy (CFL) condition: this condition is essential to obtain numerically stable solutions of partial differential equations. The general form of CFL condition is $Cr = \Delta t \sum_{i=1}^n u_{x_i} / \Delta x_i \leq Cr_{max}$, where u is the magnitude of the velocity, Δx and Δt are the length interval and the time step, respectively. The Cr_{max} value depends on the time integration scheme solver.

the order of spatial discretization. Based on that, the physical time step of 3D application must satisfy the following condition

$$\Delta t_{max} < \frac{Cr_{max}}{\sqrt{3}} \frac{\Delta x}{u_{max}}, \quad (3.2)$$

where $Cr_{max} = 1.61$ for the 3rd-order RK3 scheme from WICKER AND SKAMAROCK [2002]'s table and u_{max} is the maximum velocity which might occur during the simulation. It is recommended by WRF developers to choose a time step about 25% less than that given by (3.2) that is approximately 6 times the grid distance in kilometers, as a rule of thumb.

From ARW solver version 3, there is a capability to apply an adaptive time step, since the maximum stable time step is possibly larger than the fixed time step implied by the relation (3.2) at any time during integration. This speeds up the computation considerably.

3.1.2. Nesting

WRF-ARW provides the capability to introduce additional grids for higher horizontal resolution across a domain of particular interest. The coarser resolution grid (parent domain) acts as lateral boundary condition for the higher resolved grid. The finer domains have a relaxation zone on the outer most edges where the model is nudged towards the parent domain.

There are two options for nested grid simulations: 1-way and 2-way grid nesting. In the 1-way nest integration, the information is only exchanged from the coarser grid to the finer one. In the 2-way nesting option, the information from the finer integration is replaced for the coarser domain.

3.1.3. Physics options

In WRF-ARW, different physical options are available. Table 3.1 shows physical schemes used in this study, where we follow the WRF-ARW recommendations. Since the computation of land-surface-atmosphere fluxes in WRF depends on both the surface layer physics and the LSM, a summary of major features of them is given in the following sections.

3.1.4. Surface layer parameterization

The surface layer scheme in this study is based on the fifth-generation Pennsylvania State University- National Center for Atmospheric Research Mesoscale Model (MM5) parameterization. In the revised MM5 scheme, the surface fluxes are parameterized as follows:

Table 3.1.: WRF model physics options used in this study.

WRF model physics options	Option #	Scheme Name
Micro physics (mp_physics)	d01: 1	d01: Kessler scheme [KESSLER, 1995]
	d02: 2	d02: Purdue Lin Scheme [CHEN AND SUN, 2002]
Land surface (sf_surface_physics)	4	Noah-MP Land surface model [NIU ET AL., 2011], [YANG ET AL., 2011]
PBL (bl_pbl_physics)	1	Yonsei university scheme [HONG ET AL., 2006]
Surface layer (sf_sfclay_physics)	1	Revised MM5 scheme [JIMÉNEZ ET AL., 2012]
Shortwave radiation (ra_sw_physics)	1	RRTMG shortwave scheme [IACONO ET AL., 2008]
Longwave radiation (ra_lw_physics)	1	RRTMG longwave scheme [IACONO ET AL., 2008]

Momentum flux parameterization. The parameterization of momentum flux solves for the surface momentum flux $\overline{u'w'}|_{z=z_0}$ in terms of the friction velocity u_* :

$$\tau = -\rho \overline{u'w'} = \rho u_*^2, \quad (3.3a)$$

$$u_* = \frac{\kappa(u - u_0)}{\ln\left(\frac{z}{z_0}\right) - \psi_m(R_{iB})}, \quad (3.3b)$$

$$R_{iB} = \frac{gz(\theta - \theta_0)}{\theta u^2}, \quad (3.3c)$$

where u_* is the friction velocity, ρ is the air density, $\kappa=0.4$ in MM5 is von Kármán constant, z_0 is the aerodynamic roughness length, u is the wind speed at the level z , u_0 is the wind speed at the surface (assumed $u_0 = 0$) and ψ_m is a stability parameter which is determined by the Bulk Richardson number (R_{iB}). θ_0 is the temperature near the surface at $z = z_0$ (For more detail see JIMÉNEZ ET AL. [2012]).

Sensible heat flux parameterization. The surface heat flux is similarly parameterized:

$$H = \rho c_p \overline{\theta'w'} = -\rho c_p u_* \theta_*, \quad (3.4a)$$

$$\theta_* = \frac{\kappa(\theta - \theta_0)}{Pr \left[\ln\left(\frac{z}{z_0}\right) - \psi_h(R_{iB}) \right]}, \quad (3.4b)$$

where θ_* is the characteristic temperature; c_p is the specific heat capacity at constant pressure; $Pr=1$ in MM5 is the turbulent Prandtl number; and ψ_h is also a stability parameter as a function of R_{iB} .

Latent heat flux parameterization. The parameterization for latent heat flux follows

$$LE = -l_e \rho \overline{q'w'} = l_e \rho u_* q_*, \quad (3.5a)$$

$$q_* = \frac{\kappa(q - q_0)}{Pr \left[\ln \left(\frac{z}{z_0} \right) - \psi_h(R_{iB}) \right]}, \quad (3.5b)$$

where q_* is the moisture scale; q_0 is the moisture near the surface at $z = z_0$; and l_e is the latent heat of evaporation.

3.1.5. Land-surface model

We use here the Noah land surface model with multiparameterization options (Noah-MP LSM) developed from Noah LSM. The Noah MP LSM is the version 3 of the Noah LSM augmented through community effort [NIU ET AL., 2011].

The model incorporates snow with a maximum of three possible layers, soil with four layers and an unconfined aquifer. The total soil depth is set to 2 m. There is free gravitational drainage of soil moisture at the lower boundary. Therefore, extra water which is drained off at 2 m soil depth, accumulates in the aquifer.

Horizontally, NOAH-MP LSM uses a *semitile* subgrid scheme to realize heterogeneity (Fig. 1.2-right panel). The semi-tile approach has benefit over the conventional tile or "mosaic" approaches because it calculates solar radiation independent of the solar zenith angle (SZA). Here the surface energy balance over a grid cell used in this scheme is:

$$S_{av} + S_{ag} = L_a + LE + H + G, \quad (3.6)$$

where S_{av} and S_{ag} are canopy-absorbed and ground-absorbed solar radiation over a grid cell, respectively. L_a , LE , H , and G are the net longwave radiation, latent heat, sensible heat, and ground heat, respectively. First, the shortwave radiation is calculated over the entire grid cell considering the gap probabilities (left side of equation (3.6)). Then, L_a , LE , H , and G fluxes are obtained separately over vegetated and non-vegetated tiles (right

side of equation (3.6)) as:

$$\begin{aligned}
 L_a &= (1 - F_{veg})L_{ag,b} + F_{veg}(L_{av} + L_{ag,v}) \\
 LE &= (1 - F_{veg})LE_{g,b} + F_{veg}(LE_v + LE_{g,v}) \\
 H &= (1 - F_{veg})H_{g,b} + F_{veg}(H_v + H_{g,v}) \\
 G &= (1 - F_{veg})G_{g,b} + F_{veg}(G_v + G_{g,v})
 \end{aligned} \tag{3.7}$$

where F_{veg} is the fractional vegetated area.

There are two gap probabilities used in this scheme: between-canopy and within-canopy gap probabilities. By using these gap probabilities, shadows resulting from crown-canopies are estimated better in comparison with conventional tile schemes, especially when the sun is not overhead of canopies. Besides, this scheme can consider radius and thickness of the canopy, tree density and SZA through gap probabilities.

3.2. Synoptic situation

In this section, the large-scale weather pattern in Central Europe during the study period, 24-26 of April 2013, is discussed based on ERA-Interim reanalysis by the ECMWF. Figures (3.3) and (3.4) show a map of equivalent potential temperature (θ_e) overlaid by mean sea level pressure (mslp) contour lines, and cloud cover (cc) overlaid by horizontal wind at 500 hPa, respectively.

The study period is characterized by zonal flow in mid and western Europe with the jet stream and a very pronounced polar front located at about 60°N. Throughout 24th and 25th of April, a low-pressure system in a very wide area (North Atlantic and Scandinavia) can be seen. Thus, the weather is almost stationary and a geopotential trough extends from Greenland to Fenno-Scandia. There are very weak gradients of the geopotential over central Europe with calm winds and stationary weather.

During the study period, the center of the low-pressure system is located over Iceland and it strengthens and activates the western part of the wide trough. It steepens up and eventually merges with the cold-air mass over north-west Africa/Morocco. While on April 25, Germany is on the front side of the trough experiencing fair weather with some convection (the suppression of convection is very weak due to the weak anti-cyclonicity in the geopotential ridge over central Europe), the narrower geopotential trough begins to travel eastward on April 25 and its front side reaches West Germany on April 26 causing an eastward frontal passage over West Germany on April 26. Eventually, the trough again splits off the polar low on April 26 and builds up cold-air mass over the Iberian peninsula, i.e., the large-scale zonal flow pattern is recovered.

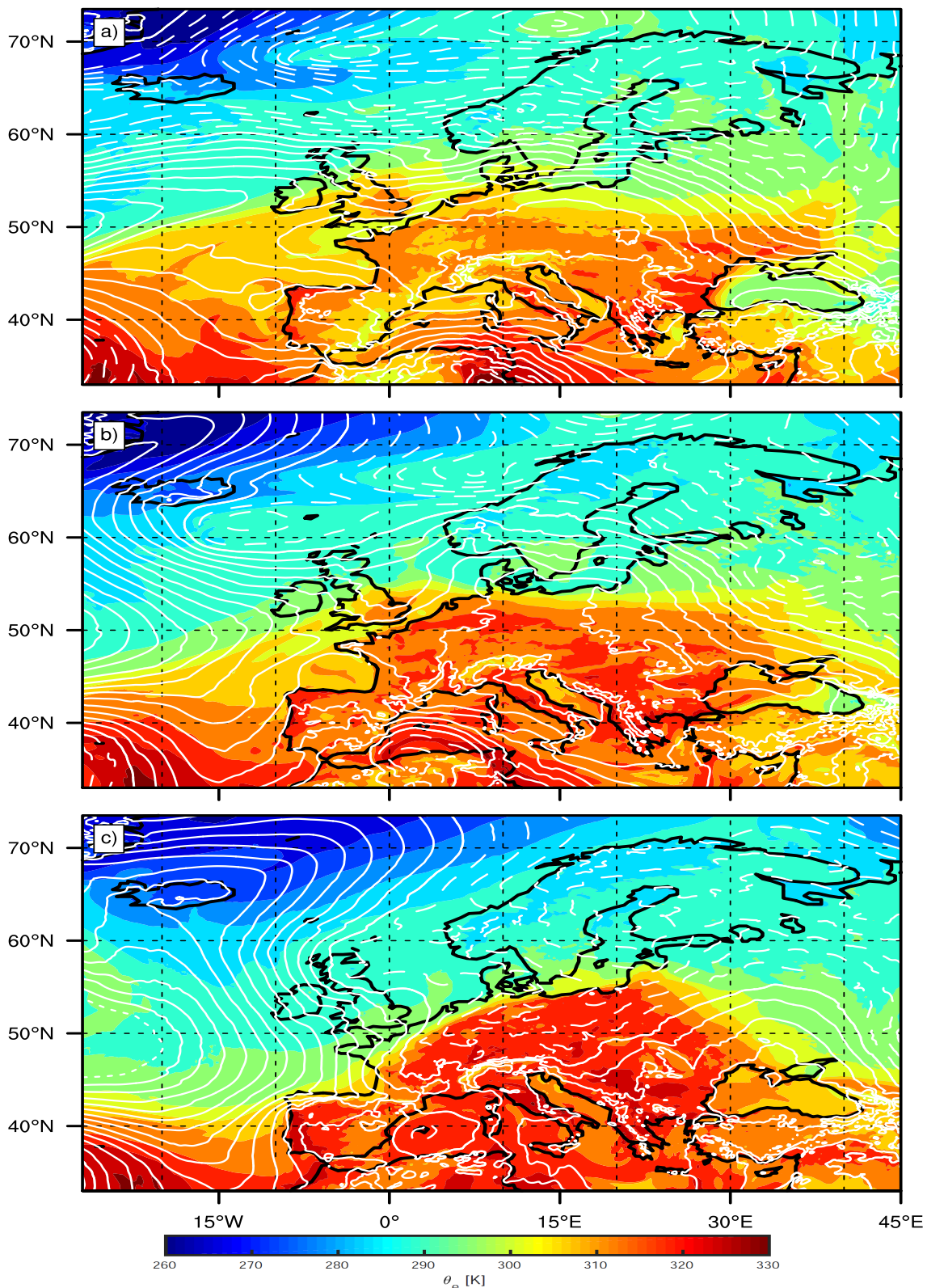


Figure 3.3.: Equivalent potential temperature at 900 hPa pressure UTC 12:00 on a) 24th, b) 25th, and c) 26th of April 2013. White contour lines indicate mean sea level (msl) pressure in hPa. Dashed white contour lines show msl below 1013 hPa and solid white contour lines show msl above 1013 hPa. Contours interval is 2 hPa.

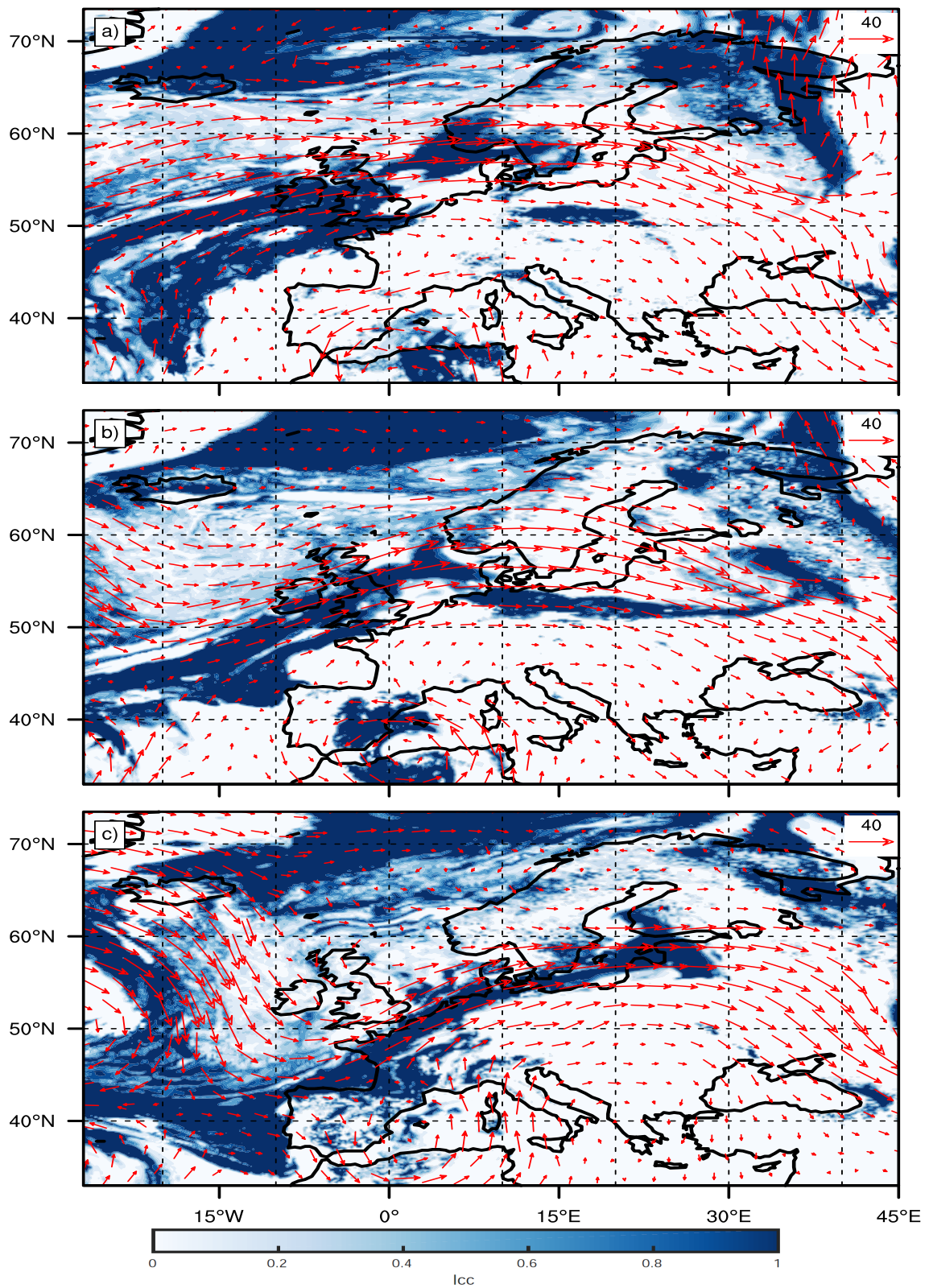


Figure 3.4.: Low cloud cover (lcc) at UTC 12:00 on a) 24th, b) 25th, and c) 26th of April 2013. Red arrows indicate horizontal wind velocity at 500 hPa. The reference wind velocity vector equals to 40 ms⁻¹.

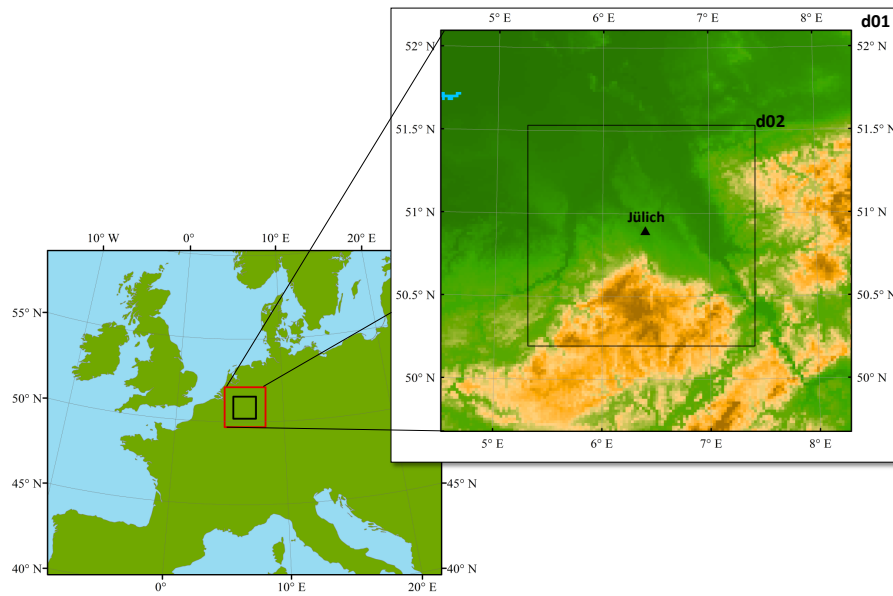


Figure 3.5.: Map of model domains in Europe region. $d01$ is parent domain. $d02$ is inner domain which is under study. It shows the topography of the model domains: Eifel mountain area is indicated by brown color and almost flat area is shown by green color.

Figure (3.4) indicates that clouds exist all along the polar jet stream. On 24th and 25th of April, almost no cloud exists over continental Europe whereas east of Iceland, eastern Russia, England and mid of Atlantic ocean are cloudy. On 26th of April, clouds are found over western Europe and Scandinavia whereas no clouds are visible Eastern and Southern Europe. The polar front is located over Germany allowing for the development of precipitation and the jet stream meanders over the Atlantic ocean.

3.3. Reference run

3.3.1. Setup

WRF-ARW is tun with two model domains centered around Jülich (Fig. 3.5). The inner domain has 1 km horizontal resolution and the parent domain has 3 km horizontal resolution and is forced by the ECMWF operational atmospheric data with a spatial resolution of 10 km and temporal resolution of 6 hours [DEE ET AL., 2011].

One-way nesting is used to couple the inner and outer domains (cf. section 3.1.2). We choose this nesting option as only for $d02$ the original land-SP is replaced by synthesized SP. Hence, a back-transfer of information from $d02$ to $d01$ is not desired. Consequently, it is ensured that $d02$ is forced by real data from $d01$ and the information from $d01$ is not mixed by artificial information from $d02$. For the same reason, a larger relaxation zone

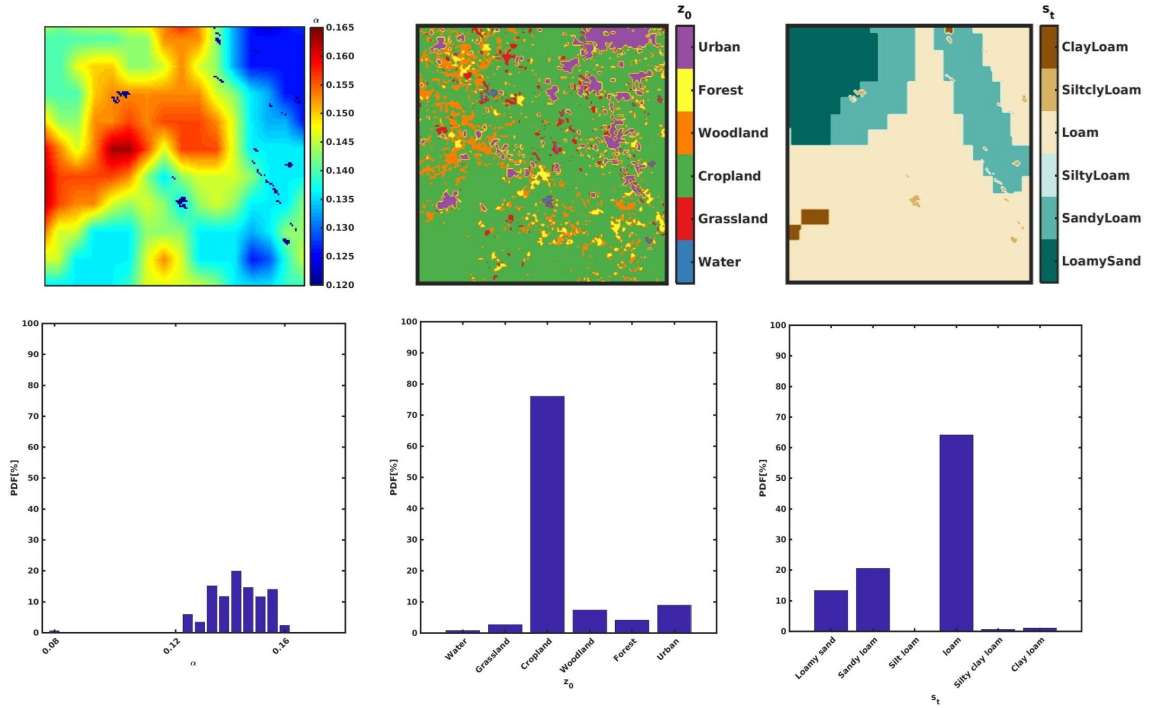


Figure 3.6.: Original SPs of albedo (left), roughness-length (center) and soil-type (right) (upper row) and their corresponding PDF (bottom row).

between the two domains is applied. In this work, the relaxation zone on the fringe of $d02$ is extended from 4 grid points (default) to 8 grid points to damp artificial modes originating from inconsistency between the outer and inner domain.

The period 24-26 of April 2013 is chosen because there exist high resolution observational data from the HOPE campaign [MACKE ET AL., 2017]. This period incorporates different atmospheric cases: 24th was clear sky, 25th was cloudy and 26th was rainy day.

For a reference run, the original geodata from USGS ² 24-category data is used. Figure 3.6 shows the original SP of the three surface properties of interest and their corresponding PDFs.

Vertical levels. Since the soil layer configuration has a fundamental impact on atmosphere land-surface interactions [LIU AND SHAO, 2013], the number of soil layers is adjusted according to the relation given by

$$\Delta s \sim \sqrt{V_G \cdot t_A}, \quad (3.8)$$

²USGS stands for the United States Geological Survey. The built-in USGS 24-category land-use data is one of the WRF geodata source which is based on Advanced Very High Resolution Radiometer (AVHRR) satellite data with about 1 km spatial resolution.

where Δs is the thickness of the soil layer in meters, ν_G is the soil thermal diffusivity ($\nu \simeq 10^{-6}[m^2s^{-1}]$), and t_A is the time scale in seconds. Based on the smallest and largest time scales in this study (from less than 1 hour to 72 hour), the soil layers are defined as shown in Fig. 3.7. The number of soil layers is also changed from 4 (default number in Noah-MP LSM scheme) to 8 to allow the land surface properties to respond to atmospheric variables.

We also change the number of atmospheric η -levels in this study from 30 levels (default) to 52 levels to have higher resolution within the boundary layer and to allow vertical resolution of shallow convection (Fig. 3.7-left side) .

Adaptive time step. Due to the high resolution in both the horizontal and vertical direction, the CFL-error is very likely to occur throughout the simulations, in particular as they are repeated many times with different boundary conditions. Thus, the model time step and the acoustic time step have to be chosen very small ($\Delta t = 6\Delta x = 6(1[km]) = 6[s]$). The computing time would become prohibitive for the case study we intend. To circumvent this limitation, we apply an adaptive time step during the simulations and as a result the computation time is reduced by approximately a factor of two. Microphysics and land-surface schemes are called every time step. The time interval for calling the radiation scheme is every 2 s.

Summary of implemented changes

The synthetic generation mechanism for the lower SP (cf. Section 2.1) allows for a study varying particular aspects of the surface boundary, where each simulation carries one single specific lower boundary condition. Similar to an operational setup, we adapt the model setup to be applicable for any of ~ 500 para-real simulations. To fulfill this condition, several adjustments to the WRF model and associated tools are performed including

- increase the number of soil layers,
- change the thickness of soil layers,
- increase the number of η levels,
- use an adaptive time step,
- use a larger buffer zone on the fringe of the inner model domain.

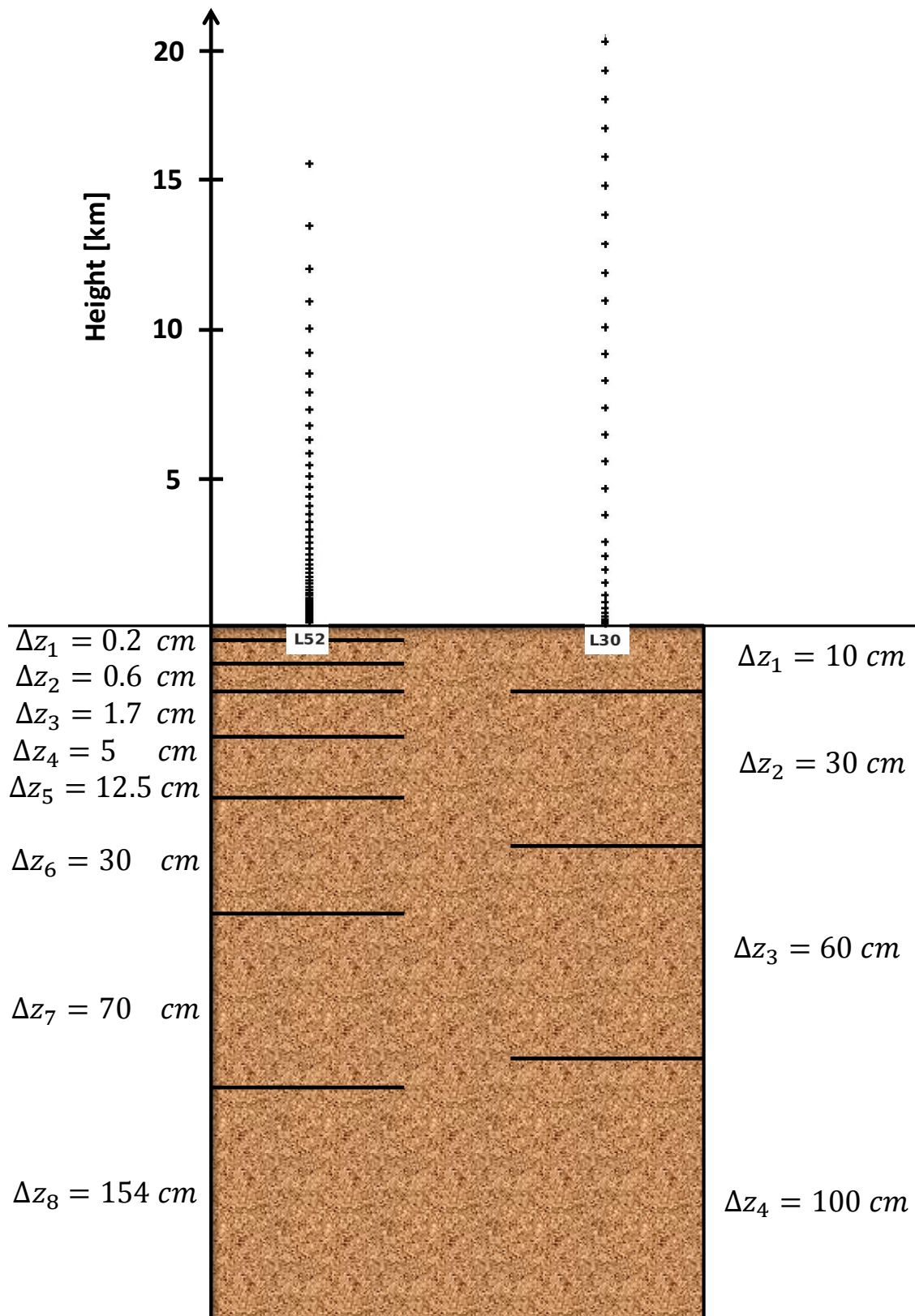


Figure 3.7.: Illustration of soil layers/thicknesses and η -levels used in this study (left) versus default soil layers/thicknesses in Noah-MP LSM and default η -levels in WRF.

3.3.2. Evaluation

The time period of this study is chosen based on the availability of high-resolution observational data in order to validate the model simulation. MACKE ET AL. [2017] carried out a field campaign called the HD(CP)2 Observational Prototype Experiment (HOPE) in and around Jülich, which took place between April 3, 2013 and May 31, 2013. They reported three different atmospheric situations on April 24-26: clear sky for 24th, PBL clouds for 25th, and frontal clouds, precipitation for 26th, of April 2013. Since the boundary layer development and particularly shallow convection is our research interest, we focus on these three days in April 2013.

We use two sets of data to evaluate the reference run (i.e., the simulation with original surface boundary conditions): (1) observation data from HOPE campaign [MACKE ET AL., 2017], and (2) forcing data from ERA-Interim European Centre for Medium Range Weather Forecasts (ECMWF) [DEE ET AL., 2011]. The model validation is constrained to Jülich location (50.909 °N, 6.4139 °E) and at 12 UTC for each day of the study.

The model evaluation concentrates on the vertical profile of the two main atmospheric bulk parameters, potential temperature ($\theta[K]$), and specific humidity ($Q[kg/kg]$). The observed profiles are obtained from surface to 10 km altitude, whereas in ECMWF reanalysis data, the vertical levels are defined from ~ 150 m to ~ 48 km height. In WRF output, the vertical levels are provided from ~ 91 m to ~ 16 km height. Hence, the black and blue curves in Fig. 3.8 do not extend all the way down to the surface.

In general, the vertical profile of potential temperature shows better consistency among different resources than the vertical profile of the specific humidity, particularly above 1 km height. This may be an indicator of unresolved subgrid motions close to surface. On 26th of April, all three θ -profiles are very close even below 1 km. This illustrates that WRF becomes numerically more stable after three days.

The variability of specific humidity profile in model and forcing data is quite significant in the first two days but they become smoother on the third day. However, the magnitude still differs from the observational profiles. On 26th above 1 km altitude, the Q-profile from ECMWF has larger values than observation one and Q-profile from WRF has smaller values, whereas, below 1 km, this relation is opposite: Although in the first two days the WRF and ECMWF Q-profiles reveal large variability against observational Q-profile, their magnitudes are relatively similar to each other, except at around 1 km height and below, i.e., in the boundary layer.

These results reveal a relatively good agreement among the reference WRF run, HOPE observations and ECMWF reanalysis data. But still it is required to ascertain whether the above model setup works properly with para-real boundary conditions or not and

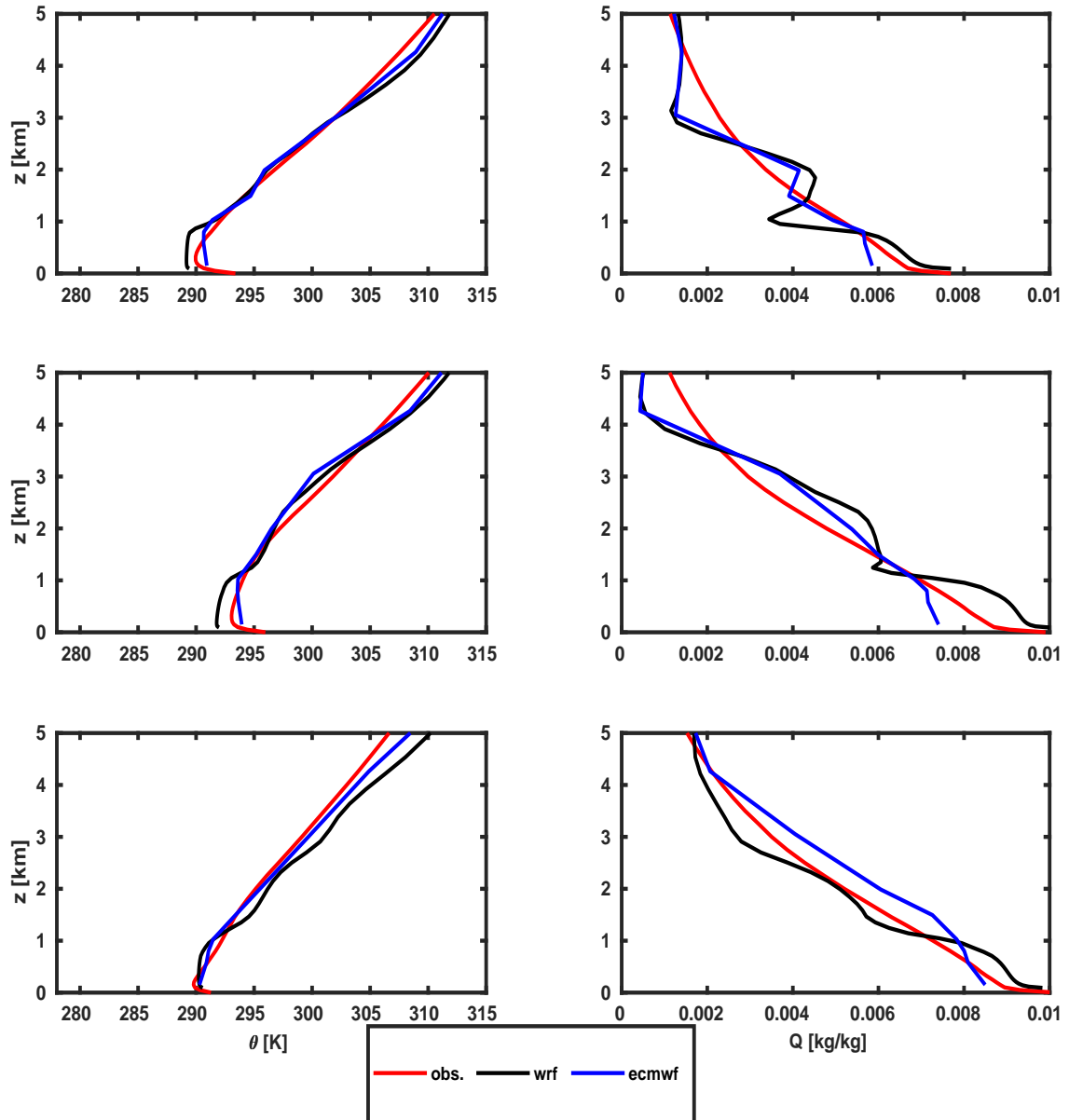


Figure 3.8.: Vertical profile of potential temperature (left column) and specific humidity (right column) at UTC: 12:00. Red, black and blue curves correspond to observation, reference model run, and ERA-Interim ECMWF forcing data at Jülich location. Rows show the days of study starting on 24.04.2013 to 26.04.2013.

what would be the impact of a synthetic surface boundary condition on land-surface-atmosphere interactions? This leads us to the analyses of the next chapter.

4. Illustration of the simulation and analysis framework

This study is aimed to investigate the dynamic effect of well-controlled properties of the land-surface on the atmosphere with the aid of the para-real simulation (cf. Section 2.1) retaining the complexity of the realistic geometry and external forcing. This chapter is designed to first ascertain the adequacy of the study design of a para-real simulation for atmosphere and land-surface processes (Section 4.1), and second, to ensure the convergence of statistics of the model outcome due to different realizations of the random processes incurred in generation of new SPs (Section 4.2).

4.1. Synthesized surface pattern as a lower boundary condition

As mentioned in section 3.3.1, we introduce several modifications to the land surface scheme to replace the SP of only one surface property to resemble or even improve the skill with respect to a real case. In addition, we arrange the WRF-options and its associated tools in a way that the model-setup is adaptable to any para-real simulation either forced by the synthesized SP of albedo, roughness-length, or soil-type. Here, we investigate the adequacy of the para-real model setup –which has the synthesized (SP) as a lower boundary condition– for a simulation of multi-scale interaction between atmosphere and land-surface heterogeneity.

The replacement of the real SP by a synthesized one (cf. Section 2.1) requires careful consideration of the aggregation effect so as to preserve the energetic and material forcing of the PBL from the surface. With due regard of this constraint, the real SP of a selected synthesized SP, is to preserve the aggregation effect of the land-surface heterogeneity. The real SP of a selected surface property (α , z_0 , and s_r) is replaced by a synthetic one with identical PDF but different spatial arrangement. Thus, the bulk surface energy balance is not changed by flux aggregation. Instead, the partitioning of the locally-conserved surface energy balance is changed.

The purpose of this section is to, first, ascertain whether the model is numerically stable and produces physically meaningful results in a para-real setup, despite the fact that the

partitioning of the surface energy balance changes considerably. Second, we investigate, to what extent the new SP is propagated into the atmosphere by the coupling mechanisms we identified above.

To assess these issues, a synthesized SP containing large patches is used, because preliminary studies show stronger signals from large patterns. Specifically, a synthesized SP generated by the quasi-fBs approach (cf. Section 2.2.2) with $s_2=3$ and $k_{max}=0.1$ is chosen, i.e., case #4 according to Fig. (2.6).

For the purpose of this section, we look at the atmospheric state close to the surface because it is expected that –if there is an effect from the surface heterogeneity on the atmospheric states– it is more significant in vicinity of the surface than higher up. As stated in the analysis framework (cf. Section 2.1.2), to delve into the impact of albedo and soil-type surface properties on atmosphere aloft, we look at temperature and water-vapor at 2 m height (T_2, Q_2). To understand the propagation of roughness-length structure into the atmosphere, we analyze aerodynamic coupling mechanism via wind components at 10 m height (U_{10}, V_{10}, W ; Fig. 4.1).

It is of our interest to find the major changes in atmospheric states which are due to new spatial arrangements of considered land-surface properties. Hence, we compare the outputs of the para-real run with the output of the reference run at 15 UTC of the first day of the simulations. We pick 15 UTC because first, the spatial mean of temperature at 2 m height reveals the maximum value at this time step, second, it is late enough after the spin-up time of the model. Thus, the atmospheric states are not affected by the sudden changes due to the sunrise and there is a quite stable PBL.

The model is numerically stable, and the para-real setup produces physically meaningful results with all adjustments we performed on the WRF model. The synthesized SP of surface-albedo is only marginally reflected in T_2 and Q_2 , that is, its pattern does not emerge therein (Fig. 4.1d and 4.1g). In comparison, the simulations forced by a synthesized roughness-length (Fig. 4.1f and 4.1i) and soil-type pattern (Fig. 4.1e and 4.1h), clearly exhibit the coherent signal from the surface in the atmospheric states.

When the soil-type is changed to the synthetic pattern, temperature and humidity signals show opposite sign of changes, i.e., temperature is higher and the moisture is lower than the reference run (Middle column in Fig. 4.1). To keep the surface energy balance, an increase in atmospheric temperature induces a decrease in atmospheric moisture. Thus, the Bowen ratio in the atmosphere remains unchanged. Moreover, this para-real simulation, which has a synthesized SP of soil-type as a lower forcing, indicates that the hydraulic mechanism carries the signal from the synthesized SP of soil-type to the atmosphere.

The opposite changes in temperature and water-vapor can be weakly seen in the para-real run forced by the synthesized SP of albedo (Left column in Fig. 4.1). However,

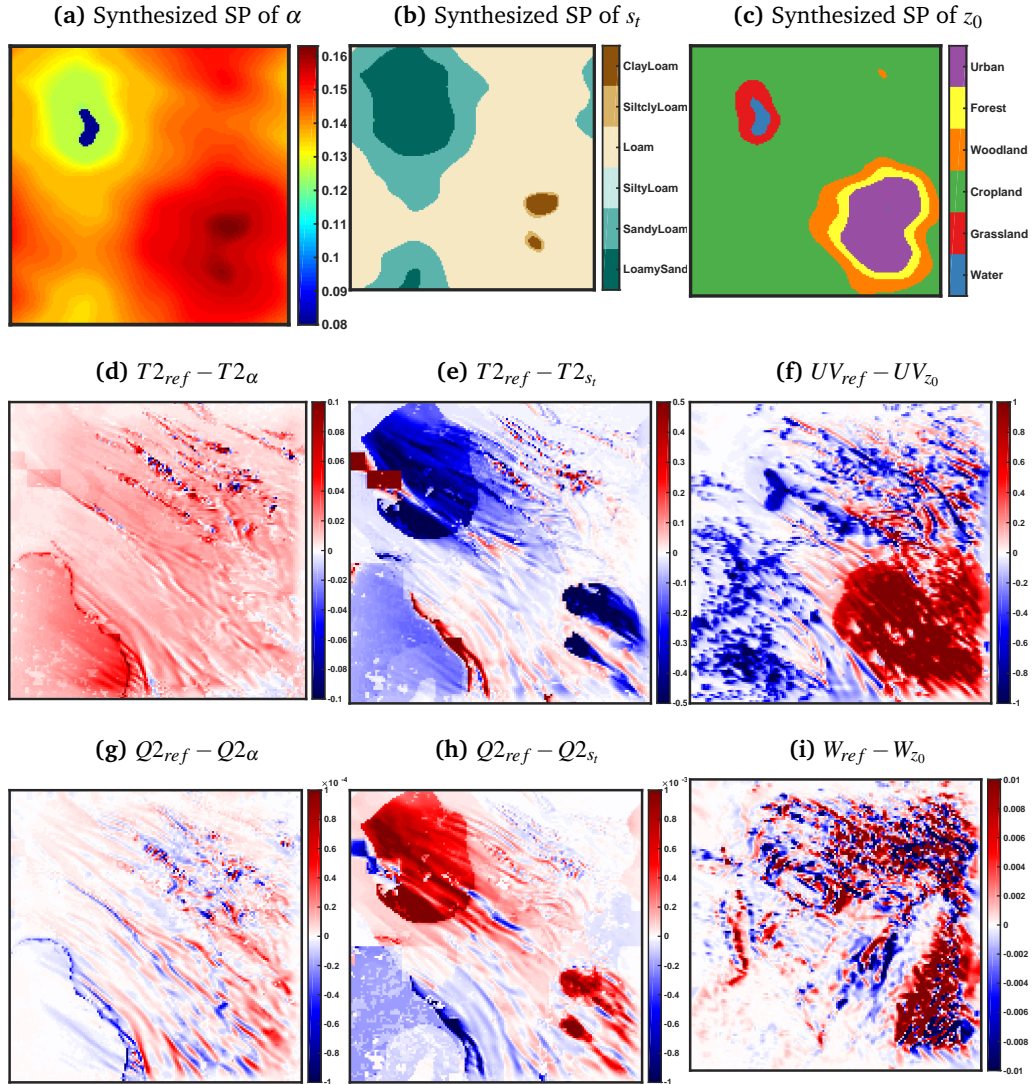


Figure 4.1.: Influence of the individual synthesized SP on atmospheric bulk parameters. Sub-figures (a), (b), and (c) show the synthesized SP of α , s_t , and z_0 , respectively; generated by $s_2=3$ and $k_{max}=0.1$. The remaining subfigures indicate the differences of the atmospheric states $-T2$ [K] (d,e), $Q2$ [kgkg^{-1}] (g,h), $UV = \sqrt{U_{10}^2 + V_{10}^2}$ [ms^{-1}] (f), and W [ms^{-1}] at the first vertical level (i)– between the reference run and the para-real run with a specified synthesized SP shown on top of each column at 15 UTC.

the dominant structures in simulations with the synthesized SP of α , is not as visible as simulations with the synthesized SP of s_r . Generally the temperature in the reference run is higher than the simulation with the synthesized SP of α . It indicates that the dynamic effects can potentially have an impact on the mean. The only visible structure in temperature is the structure of the minimum surface albedo at the top-left corner of the domain which is hardly seen (Fig. 4.1d). The minimum albedo belongs to the 'water' surface-type. It shows that the model significantly differentiate between water and land surface-type.

In the para-real simulation with the synthesized SP of z_0 (Right column in Fig. 4.1), the signal from the roughness-length structures is pronounced on the horizontal velocities of the atmosphere aloft (Fig. 4.1f). However, the new heterogeneity of z_0 is not showed up in the vertical velocity component of the wind (Fig. 4.1i). In addition, the new SP of z_0 enhances the mean horizontal wind velocity in the para-real simulation except at the largest structure of the synthesized SP at the bottom-right corner of the domain.

In conclusion, although the model is forced by a synthesized SP, the setup of the para-real simulations is adequate for the study of the land-surface–atmosphere exchanges. The new arrangement of a single surface property affects the corresponding surface–atmosphere fluxes. The signature of the synthesized SP is propagated into the atmosphere and the new SP is reflected in the identified atmospheric states close to the surface. However, the effect of the new SP of the surface albedo on T_2 is less than what we expected at this height. It may have a larger effect on the atmosphere at another height, as we will see in Chapter 6, where the propagation of the surface signal to the atmosphere (vertically and temporally), is studied.

After establishing the adequacy of the para-real setup for our study, it is required to understand the impact of the random realizations on the outcome of the para-real simulations in the following section, since the generated synthesized SP are random fractals.

4.2. Impact of random realizations (rr) on surface–atmosphere interactions

The synthesized SPs result from a random process (quasi-fBs Section 2.2.2). We quantify here the noise incurred by the randomness of the individual synthesized SP realizations. In other words, we do expect that the individual realization of the random processes used to generate the synthesized SP has an influence on the outcome not only on the specific realization of a simulation but also on its statistics. While the former is a common and anticipated issue in the numerical simulation of dynamical systems, the latter would

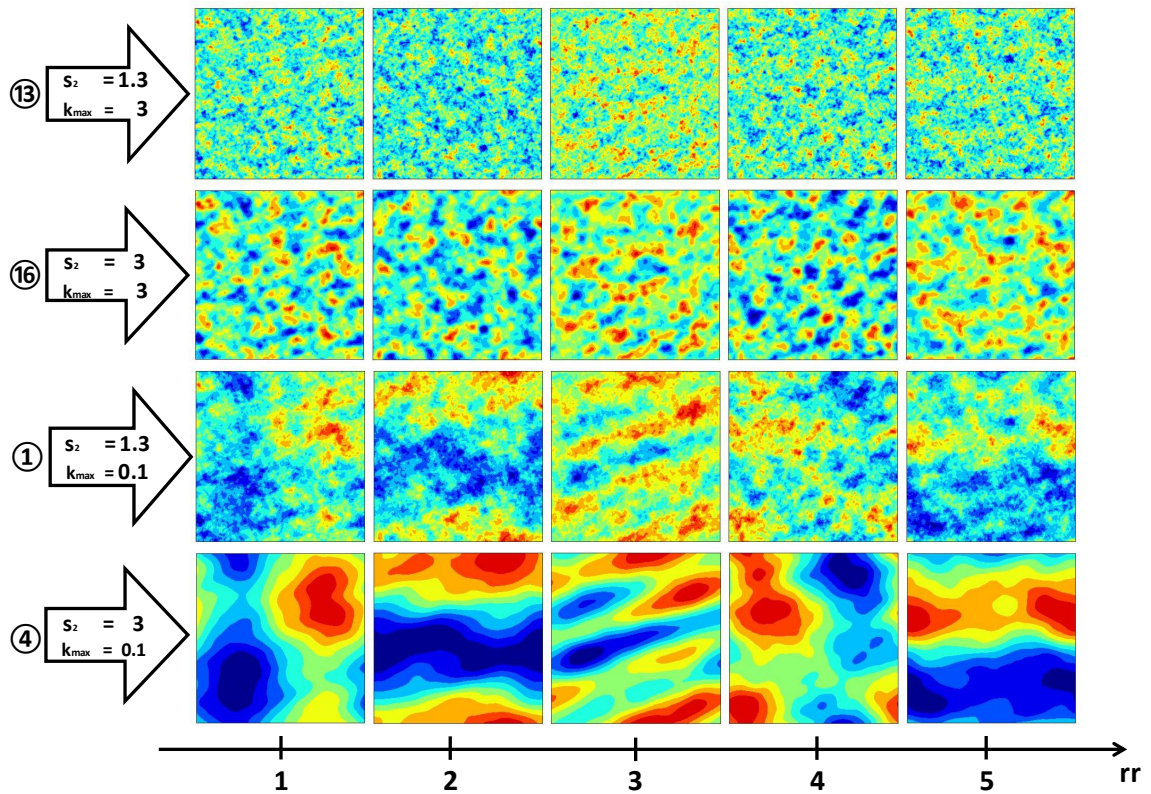


Figure 4.2.: Random realization for the four synthesized SPs at the corners of Fig. 2.6. Five different sets of random realization (columns) for each case (rows). Patterns are normalized between -1 and +1.

potentially prevent us from drawing general conclusions. We thus assess here, (a) whether the random realizations (rr) impact on the quantities that we want to consider, and (b) if it has an impact, how many realizations we have to consider until we achieve acceptable statistical convergence of any kind of property that we look at.

To answer the question (a), we consider random realizations for the synthesized SPs of some extreme cases, i.e., a small-scales SP (#13), an organized SP (#4) and two cases in between (#16, #1 cf. Fig. 2.6). Figure 4.2 shows five rr for the four cases. We name the four cases "families of synthesized SPs". Each family has five children (5 rr). Children of each family of synthesized SPs have the same parents, i.e., they exhibit the same fractal properties as governed by the parameters s_2 and k_{max} . They look different along each of the rows in Fig. 4.2. The differences are particularly large for case #1 and case #4, i.e., those cases with large-scale patches.

As the patterns differ significantly among the 5 rr, we obtained statistics from 5, 10, and 15 rr for the 12 physical cases (4 above-mentioned cases \times 3 surface properties) to find out how many realizations are required to obtain reliable statistics. Here, the result of the impact of the 10 realizations on the main mechanisms is given and in total 120 simulations

are analyzed.

As it is explained in the chapter 2, the main tool for our analyses is ANOVA method. We apply it to decompose the total variance of some key atmospheric states (cf. Section 2.1) into the different subspace components. While the variance of the synthesized SPs remains unchanged across different rr, the variance of the atmospheric states might change due to the nonlinear relation between the surface properties and the surface–atmosphere exchanges.

We focus on the full horizontal variance normalized by the total variance, $\mathbf{S}_{xy} = S_{xy} + S_x + S_y$ (cf. equation (2.15)), i.e., the variance along longitude and latitude dimensions and the changes from the beneath surface pattern are mainly appeared in it. Besides, it excludes all other effects from other dimensions of the variance. The sensitivity index of the full horizontal variance for the considered atmospheric variables is analyzed for families of synthesized SPs as a box-and-whisker plot (Fig. 4.3 and 4.4).

In general, the large-scales organized pattern (case #4) is more sensitive to the different realizations than other patterns as we infer from the large variation of \mathbf{S}_{xy} for all considered atmospheric variables and for all 12 physical cases. This is because in large-scale patterns, the orientation of patches differs significantly in different realizations and this yield so large differences because the geometry of the pattern relative to the forcing is important. In comparison, the small-scales patterns, i.e., cases #13 and #16, show very small variations in \mathbf{S}_{xy} of 10 rr for all considered atmospheric states.

The \mathbf{S}_{xy} of all considered atmospheric variables in the simulations forced by the synthesized SP of soil-type exhibits the largest variation over 10 rr. However, the smallest variation of \mathbf{S}_{xy} among 10 rr is found in the simulations forced by the synthesized SP of α . There is an exception that the sensitivity index of cloud-water (QC) shows the largest range in the simulation with the synthesized SP of z_0 . The range of variability of the sensitivity index over 10 rr for QC differs significantly among three simulations with three different forced surface properties at each case.

The analyses of this section reveal that the key atmospheric variables are affected by the realization of the random process used for generating the synthesized SP. In particular, the simulations which are forced by the synthesized SP with large-scale patches exhibit the considerable sensitivity to the random realization.

In our preliminary study, we investigated 5 rr versus 15 rr. By comparing the result, we find that 5 realizations are relatively little to obtain statistical convergence. The 15 rr, in turn, would be better than the 5 rr, but not much better than 10 random realization. Therefore, we keep on with 10 random realizations which are used for all 16 synthesized SPs and each surface property, separately. In each of 480 para-real simulations (16 (synthesized SPs) \times 10 (random realization) \times 3 (surface properties)), the same meteorological initial

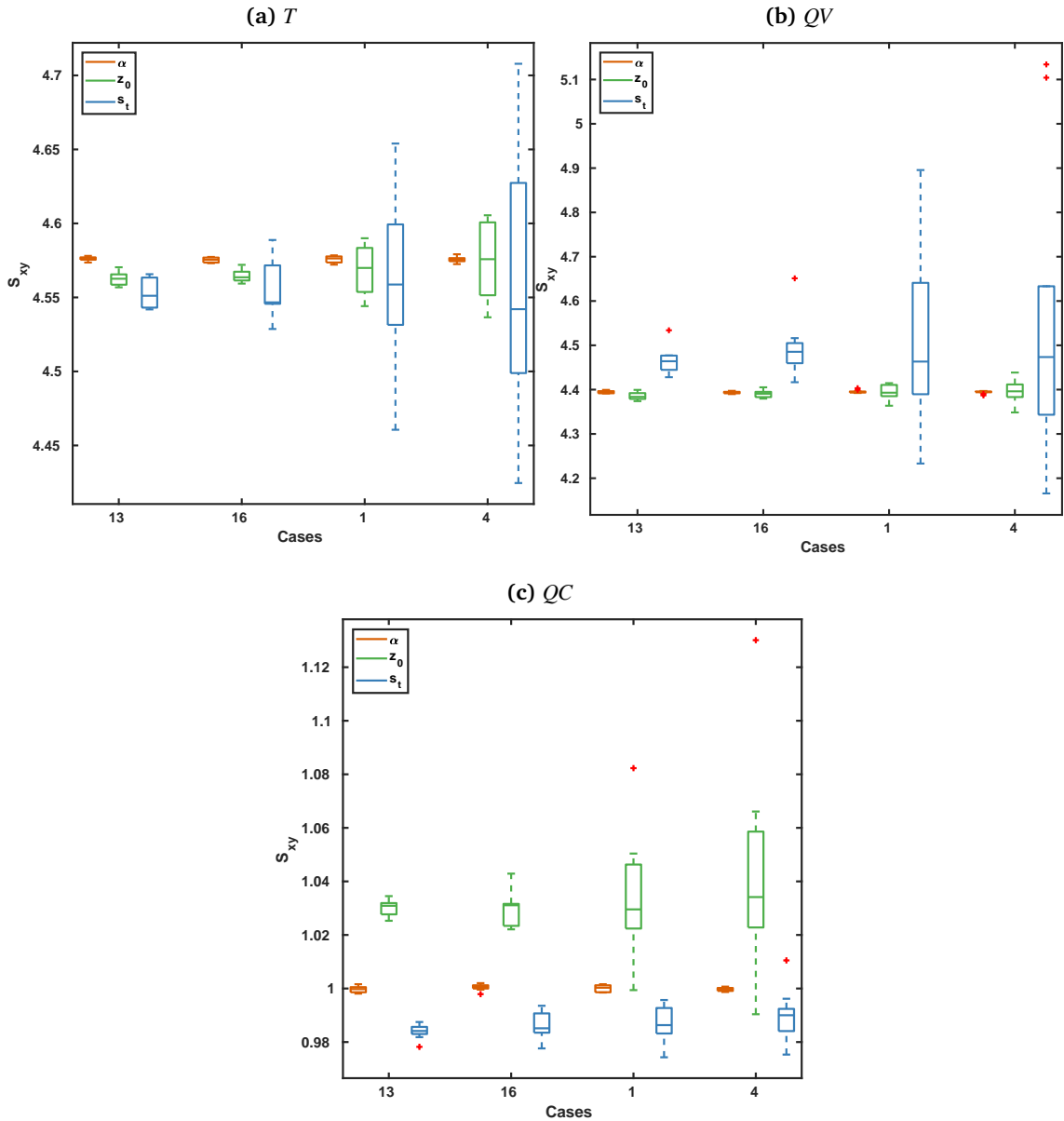


Figure 4.3.: The sensitivity index of the full horizontal variance (S_{xy}) of temperature (a), water-vapor (b), and cloud-water (c) is shown. The horizontal axis indicates the four cases of study which are forced by the synthesized SP. Numbering of the cases is according to the numbering of the synthesized SP in the Fig. 2.6. Each box indicates S_{xy} variations over the 10 rr. The color of boxes refers to a simulation which is forced by a synthesized SP of a specific surface property: α (orange), z_0 (green) and s_t (blue). The bottom and top edges of the box shows the 25th and 75th percentiles of S_{xy} data, respectively. The mark inside the box shows the median and the whiskers are extended to the most extreme values. The outliers are plotted with the red '+' symbol individually.

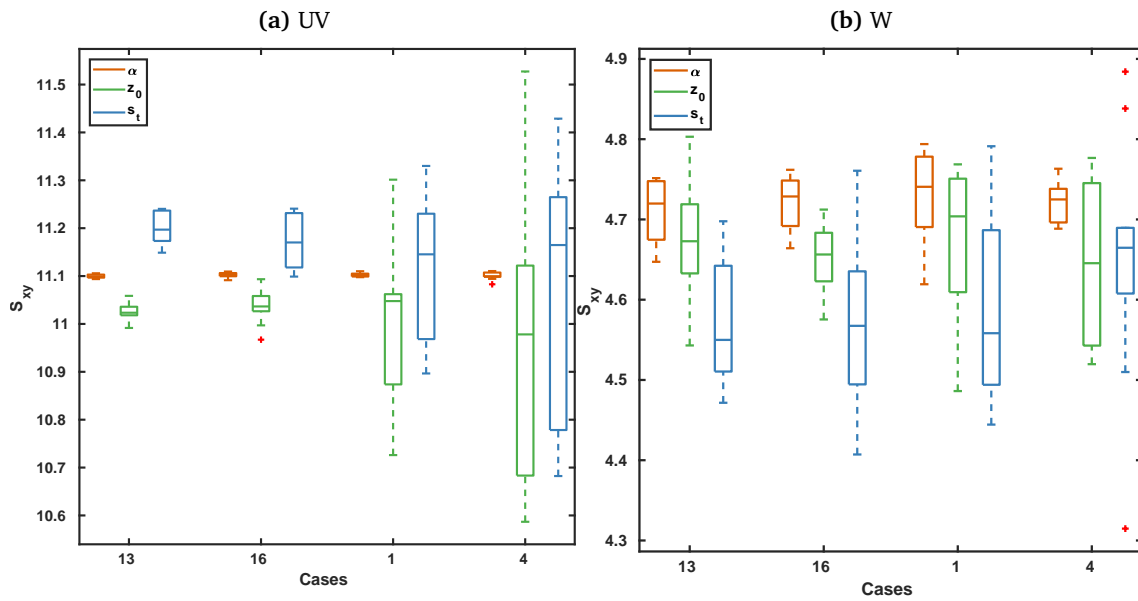


Figure 4.4.: Same as Fig. 4.3, but for wind components: horizontal wind (a), and W (b).

conditions based on ERA-Interim ECMWF reanalysis data are applied and the SP of only one surface property is replaced with a synthesized one.

In this chapter, two main aspects of this study are tested, i.e., para-real setup and random realization. Section 4.1 proves that the current para-real setup is adequate for the investigation of the land-surface–atmosphere interactions. Section 4.2 establishes the necessity of having random realization for obtaining reliable statistic from final analyses. And we conclude that ten realizations are sufficient for this purpose. We continue with the investigated setup for running 480 para-real simulations (48 physical cases times 10 rr) to focus on the dynamics effect of the land-surface heterogeneity and to answer the research questions.

5. Quantifying the impact of land-surface heterogeneity on the atmosphere

Land-surface heterogeneity impacts land-surface–atmosphere interactions through the aggregation effect and the dynamic effect (cf. Section 1.1). Here, we focus on the dynamic effect of land-surface heterogeneity. There is a non-linear relationship between surface properties and corresponding surface fluxes. Hence, the quantification of the effect of this non-linearity on atmospheric variables is demanding, in particular, on their variance. Since the atmospheric state is a function of longitude (lon), latitude (lat), height (lev), and time (t), we first decompose its variance into components of different dimensionality. In section 5.1, we study the impact of different spatial arrangement of three surface properties on multi-dimensional variance components of some atmospheric variables, which are identified in Section 2.1. Secondly, we investigate the impact of spatial changes of surface properties on these components. Section 5.2 investigates the correlation between the synthesized SP and the horizontally decomposed components of the considered atmospheric state variables.

The present analyses focus on the first two days of simulation (24-25 of April 2013, excluding the first 2 hours of the simulations as a spin-up time). The 24-25 of April 2013 are characterized by fair weather, i.e., shallow convection (cf. MACKE ET AL. [2017] and Section 3.2). In such conditions, small-scale changes of the surface properties matter to the development of convective motion in the PBL and may trigger changes to the spatio-temporal organization of shallow convection. The 26th of April 2013, on the contrary, was characterized by the passage of a large-scale frontal system. With such prevalent large-scale forcing, small-scale changes at the surface do not significantly affect large-scale frontal system with precipitation.

While not the focus of this study, our simulation exhibits small-scale numerical noise of the domain boundary during the passage of the frontal system. A possible reason is the inconsistency in chosen microphysics schemes between the two model domains, and the effect of it shows up as a consequence of the strong forcing during passage of the frontal system. Thus, the microphysical scheme becomes crucial. Even the choice of a larger buffer zone can not reduce this effect.

Since this thesis aims to study the multi-scale interactions between convection and land-surface heterogeneity, and related processes mostly occur within the atmospheric boundary layer, we focus on the lower 2 km of the atmosphere. When considering the entire tropospheric column, changes within the PBL induced by the signal of the land-surface heterogeneity might be hidden by the large-scale changes throughout the troposphere, since the induced signals of the surface are relatively small in relation to the synoptic signal. Moreover, most shallow convective motions occur within the first two kilometers above the surface.

5.1. Multi-dimensional variance decomposition

In order to understand the impact of the land-surface heterogeneity on the PBL, our para-real setup (cf. Section 2.1) is designed to unveil motions induced by the dynamic effect of the multi-scale land-surface heterogeneity. As the PDF and consequently the total variance of the surface properties remain unchanged in the para-real simulations, we can assess whether the variance of atmospheric state variables remains unchanged, or if it is non-linearly affected by dynamic effects. In addition, we inquire what would be the signature of the land-surface heterogeneity on the possible change of variance in key atmospheric state variables, i.e., temperature (T), water-vapor (QV), cloud-water (QC), and wind (UV , W).

Since we are specifically interested in the impacts of the new spatial surface arrangement on the PBL, we compare the outcome of the para-real simulations with the outcome of the real run. This allows us to focus on changes caused by the para-real boundary conditions only. For a significance test, this implies the null hypothesis of no change in variance partitioning by the surface:

$$H_0: \bar{S}_u = S_{u,ref}, \quad (5.1)$$

where u indicates subsets of the total variance of a specific atmosphere variable, \bar{S}_u is the mean over 10 rr of the multi-dimensional sensitivity indices of the corresponding para-real run, and $S_{u,ref}$ is the sensitivity index of the reference run with a real surface. If a case meets the null hypothesis, the difference between \bar{S}_u and $S_{u,ref}$ is not significant. Thereupon, the case is not considered in our analyses and displayed with gray in Fig. 5.1 and 5.2. Whenever H_0 is rejected with 90% confidence level, the ratio of \bar{S}_u to $S_{u,ref}$ is shown in S_u -matrices (Fig. 5.1 and 5.2).

Comparing the outcome of all para-real simulations in Figs. 5.1 and 5.2 (where each row stands for one combination of surface fractal parameters (k_{max} , s_2) for which 10 rr are realized, and each column shows the relative change of variance contribution in this configuration), spatial rearrangement of the soil-type pattern (lower third of each matrix) and

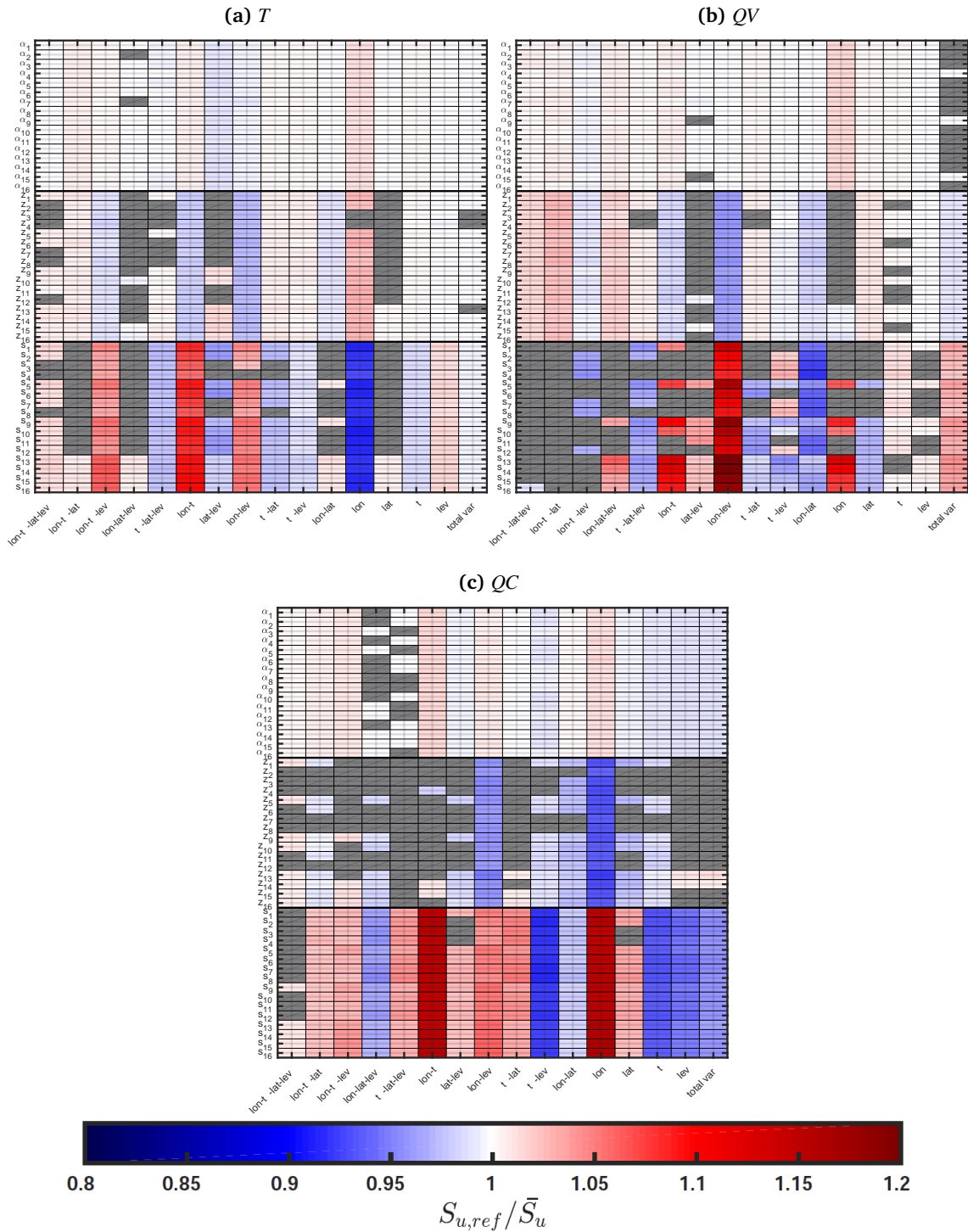


Figure 5.1.: Sensitivity indices, S_u for: (a) Temperature, (b) Water-vapor, and (c) Cloud-water. Columns show different decomposed variance components and rows indicate \bar{S}_u for different para-real runs: albedo ($\alpha_1, \dots, \alpha_{16}$), roughness-length (z_1, \dots, z_{16}), and soil-type (s_1, \dots, s_{16}). The subscripts refer to numbering in Fig. 2.6 for different synthesized SPs. The colorbar indicates the ratio of the variance components of the reference run to the mean over 10 rr of the variance components of the para-real runs. Gray color exhibits insignificant difference between \bar{S}_u and $S_{u,ref}$ with 90% confidence.

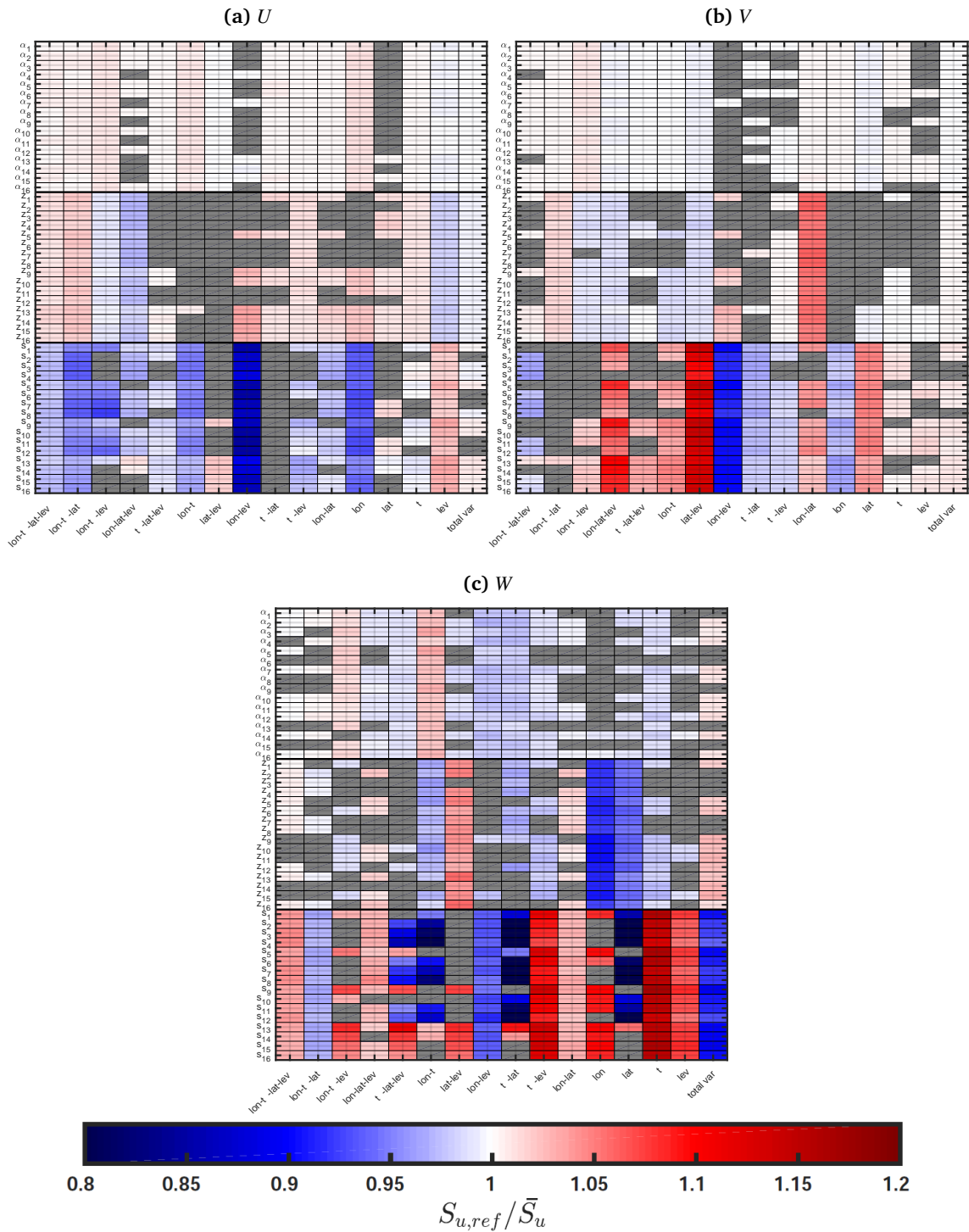


Figure 5.2.: Same as 5.1, but for: (a) U , (b) V , and (c) W .

thus the hydrological coupling affects the sensitivity indices more than the other surface properties (α and z_0). The thermodynamic coupling via α impacts least on the variance partitioning among dimensions of atmospheric variables.

5.1.1. Thermodynamic coupling through surface albedo (α)

When the synthesized SP of the albedo is used to force a para-real run, the total variance of all considered atmospheric variables except water-vapor exhibits tiny but significant changes. The change of α corresponds to the change of R_{net} in the equation 1.1. To keep the surface energy balance, the sensible heat flux (H) and the latent heat flux (LE) also change, such that the impact of these changes is observed in the total variance of T and QV .

We expected that changing the SP of albedo affects the thermodynamic coupling for its immediate impact on the surface energy balance and, thus, surface temperature. This expectation is, however, not met and Fig. 5.1a indicates only minor changes in the partitioning of temperature variance when the synthesized SP of α is used. This indicates that, although the change of surface albedo might change temperature of overlaying atmosphere, it would not change considerably the subspace variance of T along its dimensions, even not along the horizontal component ($S_{lon-lat}$). Besides, the particular forcing of albedo does not lead to accumulation of variance (at any combination of dimensions) of water-vapor and cloud-water. (first third of Fig. 5.1b and 5.1c). Hence, the latent heat flux is also not significantly affected by the thermodynamic coupling.

The role of the dynamic effect in the thermodynamic coupling is relatively prominent in the variance partitioning of vertical component of wind (Fig. 5.2c). It indicates that when a para-real simulation is forced by the synthesized SP of surface-albedo, changes in α induces more variation in the vertical air motion than in horizontal wind to balance the change of surface temperature. In other words, the synthesized SP of α generates buoyant convection in the column of air.

5.1.2. Hydrological coupling through soil-type (s_t)

Hydrological coupling in the para-real simulations with the synthesized SP of soil-type pronouncedly affects the total variance of water-vapor, cloud-water, and W component of the wind (Last column in the last third of Fig. 5.1b, 5.1c, and 5.2c). Hence, the dynamic effect can force the total variance of some atmospheric variables to be changed, despite the aggregation effect is conserved in our para-real setup.

Total variance of water-vapor decreases by 15% (Fig. 5.1b) and total variance of cloud-water increases by 20% (Fig. 5.1c) as compared to the reference run. When the entire domain-box is considered, the decrease in total variance of water-vapor and the increase in total variance of cloud-water compensate each other and the total variance of available water in the atmosphere, either in vapor or cloud form, might remain approximately unchanged.

The total variance of vertical velocity (W) in para-real simulations with the synthesized SP of soil-type is significantly larger than the total variance of W in the reference run. It indicates that there is more variation of vertical velocity when the partitioning of the soil-moisture is changed. This is due to the convection.

The spatial rearrangement of the soil-type SP has significant influence on the variance partitioning of all atmospheric state variables considered here. Soil is directly linked to the availability of moisture in the atmosphere aloft. Moreover, it indirectly affects the atmospheric temperature through the surface energy balance: if LE in equation 1.1 changes due to change of soil-moisture, H must adapt to preserve the surface energy balance.

A possible reason for the substantial impact of soil on the subspace variances of wind components is that soil affects strongly the availability of humidity at the surface. To preserve the surface energy balance, the change of humidity induces the change of temperature. As a result, it may generate horizontal transport of air due to the advection. In addition, it initiates lifting of the air parcel due to the change of the buoyancy force.

In brief, the hydrological coupling shows clearly its role for the partitioning of variance to dimensional subspaces, because changes in partitioning of the soil-moisture at the surface can directly affect the variation of the humidity in the atmosphere aloft and secondary effect of hydrological coupling impacts indirectly other atmospheric variables. However, the sign of the changes in the subspace variances are unclear and the length-scale of different SP does not play a considerable role in the magnitude of the variances.

5.1.3. Aerodynamic coupling through surface roughness (z_0)

The forcing from a synthesized SP of roughness-length affects significantly the aerodynamic coupling because the new SP of z_0 affects the friction velocity at the surface. Consequently, the synthesized arrangement of z_0 can affect wind components. Hence, the largest change in subspaces of variance of atmospheric states is observed in wind components, particularly in the vertical one (second third of Fig. 5.2). This is due to the vertical velocity playing a major role for the mass conservation in the vertical column of air. Thus, the variance of vertical velocity is more affected and the total variance of the vertical velocity decreases by 5%.

Our simulations reveal small changes in the variance partitioning of temperature (second third of Fig. 5.1a), water-vapor (second third of Fig. 5.1b), and cloud-water (second third of Fig. 5.1c). In the surface layer parameterization, temperature (eq. 3.4b) and moisture (eq. 3.5b) scales are related to the roughness-length at the surface layer and z_0 affects the sensible heat flux (eq. 3.4a) and latent heat flux (eq. 3.5a). Thus, the new SP of z_0 causes changes in the sensible and latent heat fluxes and the minor changes are detected in the variance analyses of temperature and moisture of the atmosphere. In general, the dynamic effect does not notably affect the total variance of considered atmospheric states considered through aerodynamic coupling.

5.1.4. Remarks

The length scale of the synthesized SP as lower boundary condition does not significantly impact on the subspace variance partitioning of the atmospheric states. There are a few exceptions in simulations with the synthesized SP of soil-type for which the sign of the changes in a column of a specific variance subspace differ among synthesized SPs with different fractal characteristics. In most cases, the sign of s_{13} , s_{14} , s_{15} , and s_{16} , which are more noisier-SP, is changed. This might be due to the fact that the dynamic effect of the land-surface heterogeneity depends on the scale, while this is not clearly visible in the variance analysis.

Although the flux aggregation due to surface heterogeneity is conserved by construction of our para-real setup, the dynamic effect plays a major role and causes the *total* variance of some atmospheric variables to change through different couplings. Nonetheless, the sign of changes is not consistent among three surface properties.

The sensitivity indices (S_u) appear to carry little information characterizing the SP, i.e., the color does not change along each column of Figs. 5.1 and 5.2 for the individual surface property. Besides, S_u of atmospheric states is strongly affected by **any** synthesized forcing at the surface, regardless of which coupling mechanisms is considered.

In summary, the dynamic effect of the land-surface heterogeneity significantly affects the decomposed subspace variance components of the considered atmospheric state variables. The total variance changes substantially, especially through hydrological coupling, e.g., QV , QC and W in para-real simulations with the synthesized SP of soil-type. The sign of the changes is however not consistent among different atmospheric state variables or among simulations with different SP of selected surface properties. In addition, the signature of the length-scale of the synthesized SP on the changed variance components is not clear. We commence with a correlation analysis to further pin down effects of the surface pattern on the overlaying atmosphere.

5.2. Correlation of synthesized SPs with full 2D standing eddy

The above analysis of variance partitioning identifies relevant coupling processes for the coupled land-atmosphere system under consideration. A systematic signature of the actual properties of our synthesized SP could, however, not be identified for the variance which does not carry local structural information even when decomposed to subspaces. Here, we analyze the correlation between individual synthesized SP and the atmospheric signal from ANOVA decomposed components to unveil the systematic localized linkages between the forcing from the surface and the eventual signal in the atmosphere. ANOVA decomposition carries information not only about the variance partitioning to subspaces, but also the decomposed components that contribute to the total variance. And we aim to understand whether these decomposed components are in any way systematically linked to what is being forced by the surface.

Here, the correlation between the synthesized SP of the surface property and the full horizontal decomposed component of ANOVA (\mathbf{f}_{xy}) is calculated. \mathbf{f}_{xy} represents a horizontal field that explains the 2D full horizontal contributions to the total variance and it is independent of time and vertical level ($\mathbf{f}_{xy} = f_{xy} + f_x + f_y$). The \mathbf{f}_{xy} includes the standing horizontal signal:

$$\begin{aligned}
 \mathbf{f}_{xy} &= f_{xy} + f_x + f_y \\
 \xrightarrow{(2.17)} &= P_{xy}(x, y) - P_x(x) - P_y(y) + P_\emptyset(\emptyset) + P_x(x) - P_\emptyset(\emptyset) + P_y(y) - P_\emptyset(\emptyset) \\
 &= P_{xy}(x, y) - P_\emptyset(\emptyset) \\
 \xrightarrow{(2.16)} &= \iint F(x, y, z, t) dz dt - \iiint F(x, y, z, t) dx dy dz dt.
 \end{aligned} \tag{5.2}$$

Besides, the mean of correlation coefficients between the specific synthesized SP (SSP) and \mathbf{f}_{xy} over 10 rr is calculated. In short, $r^2(SSP_{xy}^i, \mathbf{f}_{xy}^i)$ with $i \in [1, \dots, 10]$, is calculated for different atmospheric variables and is shown in matrices of Fig. 5.3.

In all para-real simulations regardless SP of which surface properties is replaced by the synthesized one, the correlation increases as the persistency (s_2) increases and the wave number of dominant scale (k_{max}) decreases (or the dominant length-scale of SPs increases).

5.2.1. Thermodynamic coupling through α

Temperature (T_{xy}). When the SP of albedo is replaced by a synthesized one, the synthesized SP of α is up to 10% anti-correlated with the horizontal decomposed component of temperature (Fig. 5.3a). When the surface albedo causes stronger reflection, the surface gains less energy from the solar radiation. Consequently, the sensible heat flux and thus

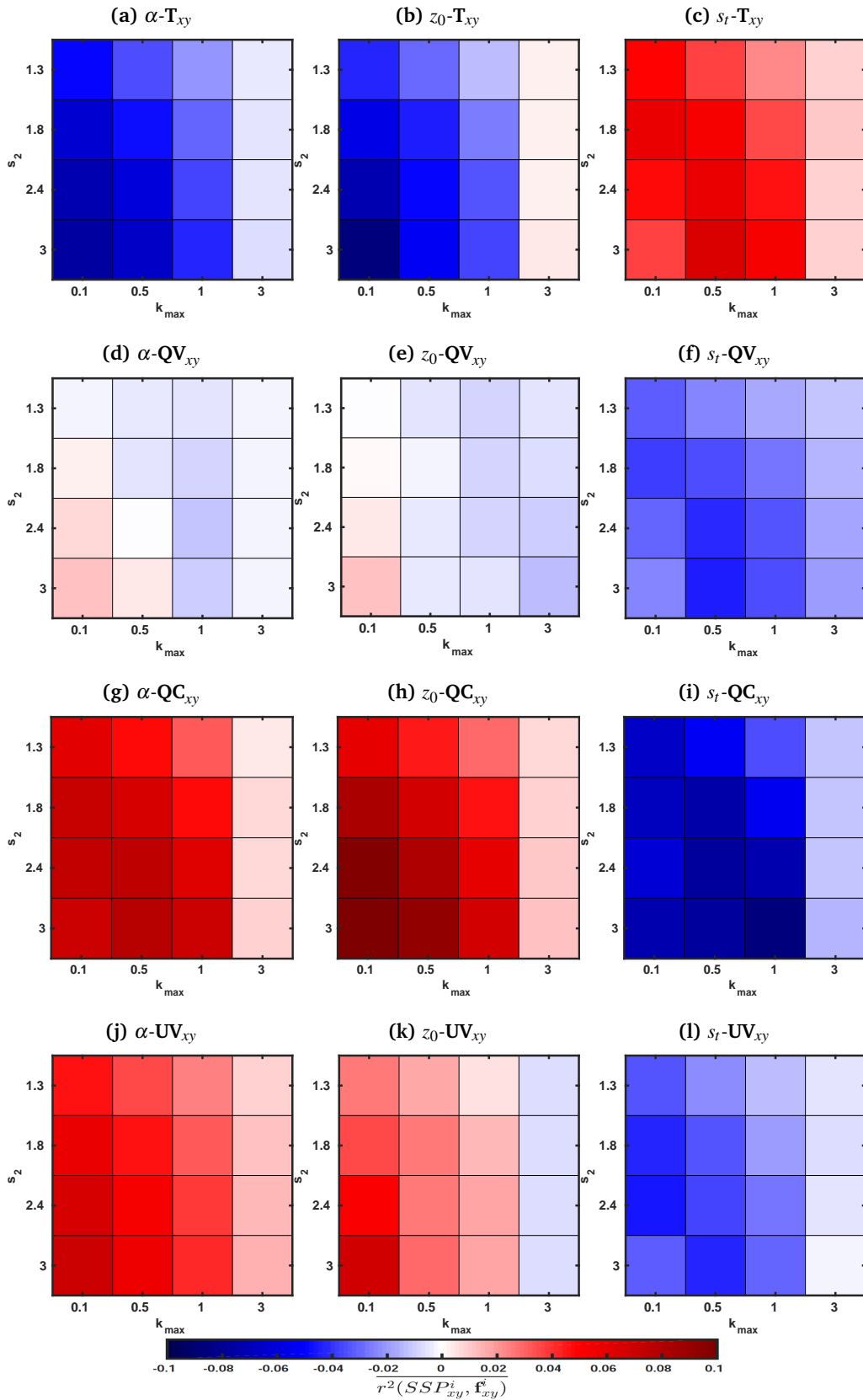


Figure 5.3.: Correlation between a synthesized SP and T_{xy} (a, b, c), QV_{xy} (d, e, f), QC_{xy} (g, h, i), and UV_{xy} (j, k, l) and for 3 surface properties: α (left column), z_0 (middle column), and s_t (right column). Each matrix contains 16 cells indicating 16 synthesized SP of Fig. 2.6.

temperature of the atmosphere aloft decreases. Therefore, the SP of α is anti-correlated with \mathbf{T}_{xy} . As the synthesized SP has a larger length-scale (smaller k_{max}) or larger persistency (larger s_2), the anti-correlation is stronger. The thermodynamic coupling brings up the strong signal from the synthesized SP of α to \mathbf{T}_{xy} . This finding is contrary to what we found in variance partitioning analyses (cf. Section 5.1.1), i.e., tiny changes occur in the variance subspaces of temperature due to the synthesized SP of α .

Water-vapor (\mathbf{QV}_{xy}) and Cloud-water (\mathbf{QC}_{xy}). Thermodynamic coupling is not reflected substantially in the horizontal decomposed component of water-vapor (\mathbf{QV}_{xy}), i.e., the synthesized SP of α and \mathbf{QV}_{xy} are less than 2% correlated (Fig. 5.3d). However, the horizontal decomposed component of cloud-water \mathbf{QC}_{xy} is highly affected by thermodynamic coupling. This difference can be explained as a consequence of the notable impact of the synthesized SP of α on the variance subspaces of W . In section 5.1.1, we found that the influence of α is relatively strong on the vertical component of wind. Thus, more variation of W induces more buoyant convection and consequently more cloud-water. As a result, a stronger correlation is seen between the synthesized SP of α and \mathbf{QC}_{xy} .

Up to 10% positive correlation reveals between \mathbf{QC}_{xy} and all length-scale of synthesized SPs of albedo except the smallest length-scale (Fig. 5.3g). Thermodynamic coupling does not transfer the signal of the noisy-pattern ($k_{max}=3$) of albedo to the atmospheric cloud-water. This illustrates that the dynamic effect is scale-dependent and does not have influence on thermodynamic coupling at this length-scale.

The sign of correlation between the synthesized SP of α and atmospheric humidity (water-vapor and cloud-water) is expected to be opposite of the correlation between the SP of α and \mathbf{T}_{xy} . This is dictated by the surface energy balance: any change in the sensible heat flux has to be compensated for the latent heat flux. Hence, the synthesized SP of albedo is positively correlated with \mathbf{QC}_{xy} (all cases) and \mathbf{QV}_{xy} (large-scale patterns: $k_{max}=0.1$).

There are some cases for which the correlation between the synthesized SP of α and \mathbf{QV}_{xy} is negative. These SPs are small-scale patterns. A possible reason is that the signal of the synthesized SP of albedo in water-vapor is vertically propagated and it is detectable in higher up levels of the atmospheric water-vapor, not in the full horizontal decomposed component of water-vapor (which is the subject of the analysis in the next chapter).

Wind components (\mathbf{UV}_{xy} and \mathbf{W}_{xy}). Up to 10% positive correlation is exhibited between the SP of albedo and horizontal velocity of wind (Fig. 5.3j): the larger the SP of albedo, the stronger the correlation. As α increases, it induces more reflection than absorption from solar radiation at the surface, atmospheric temperature at the surface (θ_0 in equation 3.4b)

is cooled down. Consequently, the friction temperature (θ_*) and thus the sensible heat flux (H) enhances. Therefore, the buoyancy forces the atmospheric motion to increase.

However, there is almost zero correlation between the SP of α and vertical wind velocity (not shown here). It indicates that the thermodynamic coupling does not affect W_{xy} although it affects considerably the variance partitioning of W (cf. Section 5.1.1).

5.2.2. Hydrological coupling through s_t

As the soil-type is a category, a standard regression analyses requires to convert the soil-type to a specific soil property that carries a physical meaning. Relevant soil properties are given in table 5.1. The most important signal from soil-type is moisture transport

Table 5.1.: A list of soil properties given by SOILPARM.TBL of WRF.

Property	Definition
MAXSMC	maximum soil-moisture content
DRYSMC	dry soil-moisture threshold
SATDW	saturation soil diffusivity
SATPSI	saturation soil potential
SATDK	saturation soil conductivity
QTZ	soil quartz content
REFSMC	reference soil-moisture
WLTSMC	wilting point soil-moisture

and we choose the property that characterizes this signal most appropriately. MAXSMC and DRYSMC show the maximum and minimum soil-moisture content. They are extreme values and are not desired in this study. SATDW, SATPSI, and SATDK properties are representative of saturated soil and, thus, not the suitable choice as well. QTZ shows the amount of quartz and it is not relevant to the purpose of this study. REFSMC indicates the capacity of soil to take up the water. WLTSMC shows the minimal amount of moisture in the soil that the plant needs not to wilt. Hence, it is again a kind of extreme value, which does not fit the purpose of analysis of this section. Finally, **REFSMC** is selected to convert soil categories to a soil property and hereafter the synthesized SP of the soil-type is converted to synthesized SP of the REFSMC. In the following, the correlation analysis between the synthesized SP of REFSMC and the identified atmospheric state variables is given.

The influence of the length-scale of SPs through hydrological coupling is consistent with thermodynamic coupling: the larger the pattern, the stronger the correlation. The hydrological mechanism also carries little information about SPs with $k_{max} = 3$ into atmosphere

aloft and less than 2% correlation is found between the synthesized SP of soil and all considered atmospheric states (regardless of sign).

Similar to the multi-dimensional variance analysis in which the hydrological coupling had the largest impact on the variance subspace of all considered atmospheric state, it also exhibits its notable role on the full horizontal decomposed component of all atmospheric state variables. The largest correlation of atmospheric states with the SPs reveals when the atmosphere is forced by the new arrangement of the soil property.

Temperature (T_{xy}). The hydrological coupling significantly impacts on the horizontal decomposed component of the atmospheric temperature, i.e., up to 10% positive correlation exists between T_{xy} and the synthesized SP of REFSMC (Fig. 5.3c). The positive correlation can be verified as an indirect effect of soil-moisture capacity: larger REFSMC indicates that less moisture is released by soil, therefore the sensible heat flux and, thus, atmospheric temperature increases to hold the surface energy balance. As a result, we find a positive correlation between soil-moisture capacity field and T_{xy} .

Water-vapor (QV_{xy}) and Cloud-water (QC_{xy}). In para-real simulations with synthesized SP of soil, the horizontal decomposed component of water-vapor and cloud-water are both negatively correlated with the synthesized SP of REFSMC (Fig. 5.3f and 5.3i). In particular, the hydrological coupling plays a dominant role in QC_{xy} and there is a 10% negative correlation between QC_{xy} and the SP of REFSMC for all length-scale SPs except the synthesized SPs with $k_{max}=3$ (-2% correlation). This negative correlation between REFSMC and moisture in the atmosphere aloft (either as water-vapor or cloud-water form) is due to the reverse relation between the soil capacity field and humidity in the air. As soil has higher capacity to take up moisture (larger REFSMC), the latent heat flux within the surface layer is smaller. Consequently the atmospheric moisture is reduced.

Wind components (UV_{xy} and W_{xy}). The horizontal wind velocity is up to 8% anti-correlated with the SP of soil (Fig. 5.3l). The new arrangement of soil impacts substantially the latent heat flux in the surface layer due to the change of q_0 (cf. equation 3.5a). To accompany this change, u_* is also changed accordingly and, thus, the soil capacity and UV_{xy} are anti-correlated.

In contrast, there is a 6% positive correlation between vertical wind velocity and the synthesized SP of soil (not shown here). the different length-scale of the synthesized SPs has no impact on W_{xy} , i.e., the correlation is uniformly red (+6% correlation). As the surface layer humidity is increased by the soil-moisture, more vertical air motion is induced to hold mass conservation in a column of air. This finding is consistent with what we found

in section 5.1 about the impact of hydrological coupling on the total variance of W : there was an increase in the total variance of W in the para-real simulations coupled with the synthesized SP of soil compared to the reference run.

5.2.3. Aerodynamic coupling through z_0

Similar to the thermodynamic and hydrological couplings, aerodynamic coupling also carries an insignificant signal of noisy-SP with $k_{max}=3$ from the surface to the atmosphere and the correlation between all considered atmospheric states and the synthesized SP of z_0 with small-scale patches ($k_{max}=3$) is around zero.

Temperature (T_{xy}). The horizontal decomposed component of the atmospheric temperature and the SP of z_0 are up to 10% anti-correlated according to the equation 3.4b, i.e., the larger the pattern, the stronger the anti-correlation (Fig. 5.3b). In the WRF surface layer parameterization, the sensible heat flux is linked to the characteristic temperature (θ_*) which is inversely related to the roughness-length.

Water-vapor (QV_{xy}) and Cloud-water (QC_{xy}). Zero correlation of the horizontal decomposed component of water-vapor and the SP of z_0 indicates that aerodynamic coupling has insignificant impact on QV_{xy} (Fig. 5.3e). Instead, it affects considerably cloud-water (Fig. 5.3h). When the surface has a larger-scale roughness pattern, more cloudiness might be generated due to the larger buoyancy force. Thus, cloud and the SP of roughness-length are up to 10% positively correlated.

Wind components (UV_{xy} and W_{xy}). As the roughness-length has a larger-scale synthesized SP, the correlation between the synthesized SP and wind components is stronger, regardless of sign of the correlation coefficient (positive or negative). The positive correlation between the synthesized SP of roughness-length and UV_{xy} is due to the momentum conservation along flow (Fig. 5.3k): An increase of the surface roughness-length causes the flow to decelerate at the surface; thus, the higher-up flow is accelerated to preserve the momentum conservation in a column of air.

There is a very weak correlation between vertical wind velocity and the SP of roughness-length (less than 2%). Aerodynamic coupling affects insignificantly the vertical air movement while it mainly affects the horizontal velocities according to the log-wind-profile (cf. equation 3.3b). In contrast, the total variance of W is affected relatively more than the horizontal components by the aerodynamic coupling (cf. Section 5.1).

5.2.4. Remarks

All three couplings have relatively minor impact on W_{xy} in comparison to UV_{xy} . Since the synthesized forcing from the land-surface is in horizontal directions, it induces the deviation from vertical mean velocity (impact on different dimensionality of its variance). In other words, the buoyancy force which might be generated due to the new synthesized SP through different mechanisms, does not affect the horizontal pattern of W . However, it affects its magnitude.

In summary, the multi-scale surface signal on the horizontally decomposed component of atmospheric variables is clear and almost consistent in all atmospheric variables: the larger the pattern, the stronger the correlation (either negatively or positively). Even the albedo pattern -for which only slight changes in the variance partitioning based on sensitivity indices were found- exerts a coherent signal from the synthesized SP of the albedo (α).

6. Propagation of the land-surface pattern into the atmosphere

In the previous chapter, we studied the impact of the dynamic effect on the main coupling mechanisms through analysis of the sensitivity indices (Section 5.1) and the correlation between the horizontally decomposed component of specific atmospheric variables and the SP of selected surface properties (Section 5.2). We find that 10-20% of the variance of atmospheric variables is governed by the synthesized SP of surface properties.

The coherent signal of multi-scale SP from analyses (Section 5.2) leads us to calculate the correlation between the synthesized SP of the surface property and ANOVA decomposed component as a function of height and time. In particular, it is of our interest to understand whether those atmospheric variables, which exhibited no correlation between the SP and their horizontally decomposed component, are to some extent correlated to the SP of selected surface properties at a specific height or at a specific time. In other words, how far does the signal of the synthesized SP of considered surface properties (α , z_0 , and s_t) propagate vertically by the surface–atmosphere couplings (Section 6.1 and 6.2)? And does the signal also propagate temporally (Section 6.3 and 6.4)?

To answer these two questions, we calculate the correlation between different ANOVA decomposed components and the corresponding synthesized SP. For the sake of brevity, this calculation is summarized in the mathematical notation as

$$\bar{R}_{N_u}^M(\chi), \quad (6.1)$$

where R indicates the correlation between the synthesized SP of M and N_u as function of χ . M represents the three surface properties ($M \in \{\alpha, z_0, s_t\}$), N_u stands for ANOVA component of the atmospheric variables ($N_u \in \{T_u, QV_u, QC_u, UV_u, W_u\}$), and u indicates the dimensionality of ANOVA component ($u \in \{xyz, hz, xyt, ht\}$). The overbar indicates the mean of 10 yr and $\bar{R}_{N_u}^M(\chi)$ is a function of height or time ($\chi \in \{z, t\}$).

In table 6.1, a list of the sensitivity indices is given to have an overview of the contribution of N_u into the total variance. While the fraction of the variance in the single 3D components, S_{xyz} and S_{xyt} is very small, the combined signal, S_{hz} and S_{ht} , carry relatively large amount of variance (up to more than half of the total variance). This potentially warrants

Table 6.1.: Contribution of subspace variance into the total variance [%] from the reference run.

	T	QV	QC	UV	
S_{xyz}	0.16	0.73	4.10	0.97	Section 6.1
S_{hz}	51.61	61.25	11.87	27.26	Section 6.2
S_{xyt}	0.39	3.58	4.07	1.84	Section 6.3
S_{ht}	36.84	27.26	10.34	54.38	Section 6.4

a large explanatory power of the components.

6.1. Vertical propagation of the surface signal into the 3D standing eddy (f_{xyz})

We study here the signal from the surface at different heights through the correlation between the synthesized SP of a surface property and the 3D standing eddy of the corresponding variable. The 3D standing eddy is represented by (cf. Section 2.4.2):

$$\begin{aligned}
f_{xyz} &\xrightarrow{(2.17)} P_{xyz}(x, y, z) - f_{xy}(x, y) - f_{yz}(y, z) - f_{xz}(x, z) - f_x(x) - f_y(y) - f_z(z) - f_\emptyset(\emptyset) \\
&= P_{xyz}(x, y, z) - P_{xy}(x, y) - P_{yz}(y, z) - P_{xz}(x, z) + P_x(x) + P_y(y) + P_z(z) - P_\emptyset(\emptyset) \\
&\xrightarrow{(2.16)} = \int F(x, y, z, t) dt \\
&\quad - \iint F(x, y, z, t) dz dt - \iint F(x, y, z, t) dx dt - \iint F(x, y, z, t) dy dt \\
&\quad + \iiint F(x, y, z, t) dy dz dt + \iiint F(x, y, z, t) dx dz dt + \iiint F(x, y, z, t) dx dy dt \\
&\quad - \iiint F(x, y, z, t) dx dy dz dt.
\end{aligned}$$

According to equation (6.1), $\bar{R}_{N_u}^M(z)$ is calculated for $M \in \{\alpha, z_0, s_t\}$ and $N_u \in \{T_{xyz}, QV_{xyz}, QC_{xyz}, UV_{xyz}, W_{xyz}\}$ (Fig. 6.1).

In general, the larger the length-scale of the SP, the stronger the correlation (either positively or negatively from red to black curves). The noisy-SPs with $k_{max}=3$ reveal almost zero correlation (<2%) with $f_{xyz}|_{z=z'}$ of selected atmospheric states at any height (Black curves in the figures of this chapter), except for two cases. The two exceptions at this length-scale are: (1) hydrological coupling carries the signal from the noisy-SP of soil-moisture into the atmospheric temperature (Fig. 6.1c) and water-vapor (Fig. 6.1f), (2) aerodynamic coupling transports the signal of the roughness-length at this length-scale to horizontal wind velocity (Fig. 6.1k). This illustrates that the hydrological and aerodynamic couplings are independent of the length-scale of the SPs when their immediate

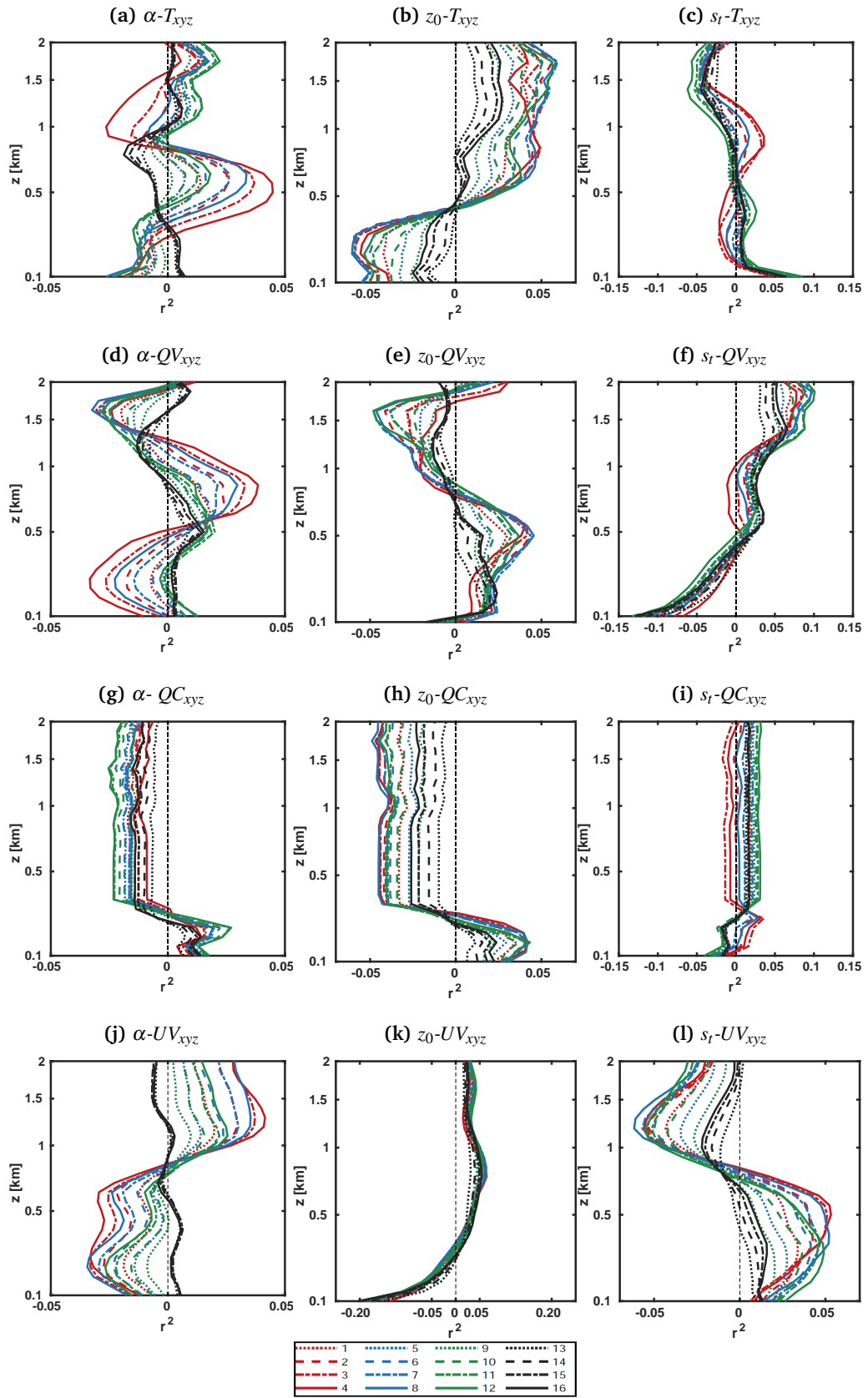


Figure 6.1.: Vertical profile of $\bar{R}_{N_{xyz}}^M$ for α (left column), z_0 (middle column), and s_t (right column)) with T_{xyz} (a,b,c), QV_{xyz} (d, e, f), QC_{xyz} (g, h, i), and UV_{xyz} (j, k, l). The legend shows 16 synthesized SP according to numbering in Fig. 2.6.

effect is considered, i.e., the soil-moisture impacts directly on the atmospheric water-vapor and the roughness-length affects immediately on horizontal wind, regardless of the length-scale of the signal. Therefore, any length-scale SP of s_t and z_0 is transferred by the latent heat flux (and, thus, sensible heat flux as a result of the surface energy balance) and momentum flux respectively, and the signal from any SP is propagated to the atmosphere by the corresponding couplings.

6.1.1. Thermodynamic coupling by α

Temperature (T_{xyz}). Thermodynamic coupling carries information from the SP of α into the atmospheric temperature up to 500 m height, where the maximum positive correlation of α and T_{xyz} occurs (Fig. 6.1a). Then, the signal from the SP of albedo vanishes in atmospheric temperature. The surface temperature (θ_0 in the equation 3.4b) has an inverse relation with the surface albedo and thus the characteristic temperature in the surface layer parametrization (θ_*) reveals similar changes as α . Moreover, the sensible heat flux is linearly related with the θ_* (cf. equation 3.4a). Thus, it obeys the sign of the change of the surface albedo and they are positively correlated.

Water-vapor (QV_{xyz}). Any change in the sensible heat flux has to be adapted by the latent heat flux to keep the surface energy balance. Therefore, water-vapor exhibits a negative correlation between the SP of α and the QV_{xyz} , however, not exactly at 500 m height (Fig. 6.1d). The large negative correlation is found at two vertical levels, i.e., closer to the surface (at about 200 m) and 1500 m height. In fact, at 500 m, no signal from the SP of albedo is detected in the atmospheric water-vapor. It is interesting to find that the water-vapor response to the change of albedo occurs closer to the surface and stronger than the temperature response to the change of α . The positive correlation between the synthesized SP of α and QV_{xyz} at about 1000 m is explained as an opposite impact of α on LE : with increasing albedo, less sensible heat is transferred into the atmosphere, thus more latent heat is changed to preserve the surface energy balance. This 5% correlation between the SP of a surface property (here α) and the atmospheric states at different heights is intriguing because it indicates 5% of variability can be explained only by the SP in either temperature or water-vapor at these heights, where other forcings and complex atmospheric interactions exist.

Cloud-water (QC_{xyz}). The $\bar{R}_{QC_{xyz}}^\alpha(z)$ indicates that the change of partitioning of albedo has a very weak signal on QC_{xyz} (Fig. 6.1g). This is contrary to our finding in section 5.2: the role of new surface forcing through thermodynamic coupling is more dominant on the full horizontal decomposed component (QC_{xy}) than on the QV_{xy} . Although the

magnitude of $\bar{R}_{QC_{xyz}}^\alpha(z)$ is relatively small, the feedback on the new SP of α is considerable. Positive $\bar{R}_{QC_{xyz}}^\alpha(z)$ close to the surface is found due to the surface energy balance: larger α causes less H and consequently more LE . Above 500 m, the small anti-correlation can be interpreted as a feedback on positive $\bar{R}_{QC_{xyz}}^\alpha(z)$ at 500 m.

Wind components (UV_{xyz} and W_{xyz}). The synthesized SP of albedo has no impact on the vertical velocity, i.e., no correlation is found (not shown here). There is an anti-correlation between the synthesized SP of α and horizontal wind component in the vicinity of the surface which is encoded by the surface layer parametrization (cf. eq. 3.4a). Above 1 km, the correlation becomes positive as a result of the momentum conservation. This is pronouncedly seen in the profile of the large-scale and high persistency SPs ($k_{max}=0.1$ and 0.5 (red and blue curves), $s_2=2.4$ and 3 (solid and dashed-dotted curves)). It indicates that the dynamic effect plays a dominant role in propagation of the signal from large-scale patterns through thermodynamic coupling.

6.1.2. Hydrological coupling by s_t

Temperature (T_{xyz}). The maximum positive correlation between the synthesized SP of soil-type and T_{xyz} occurs at the surface (5-10%). It shows that 10 percent of the variability of temperature can be explained by the synthesized SP of the soil-moisture. As explained in Section 6.1.1, in order to keep the local surface energy balance, while REFSMC is increased, less moisture is released by soil into the atmosphere aloft and, thus, the latent heat flux decreases. To locally preserve the surface energy balance, the sensible heat flux increases, indicating that temperature increases as well. Thus, there is a positive correlation between the synthesized SP of REFSMC and temperature at the surface. Besides, there is -5% correlation at the top of the profile (1.5-2 km).

Water-vapor (QV_{xyz}). The entire shape of the profile of the $\bar{R}_{T_{xyz}}^{s_t}(z)$ is reversely exhibited by the profile of the $\bar{R}_{QV_{xyz}}^{s_t}(z)$ (Fig. 6.1f): at the surface, the synthesized SP of REFSMC of all synthesized SPs with different characterizing fractal properties is significantly anti-correlated with QV_{xyz} (7-15%), and the signal from the surface is propagated upto 2 km height (+10% positive correlation). This indicates the direct influence of released moisture by soil and atmospheric humidity at the surface, i.e., as REFSMC decreases, more moisture is released by soil which is carried by the latent heat flux into the atmosphere aloft (anti-correlation between REFSMC and atmospheric water-vapor).

Cloud-water (QC_{xyz}). In contrast to the water-vapor profile, the $\bar{R}_{QC_{xyz}}^{s_t}(z)$ shows small values but its profile curve is similar to water-vapor profile (Fig. 6.1i), i.e., -5% at the

surface and $<+2\%$ above 300 m. The hydrological coupling carries a very weak signal of the SP of soil-moisture into QC_{xyz} . In the previous chapter, however, the hydrological coupling played a dominant role in the change of both QV_{xy} and QC_{xy} , with almost the same order of magnitude.

Wind components (UV_{xyz} and W_{xyz}). No correlation exists between the synthesized SP of the soil-moisture and W_{xyz} (not shown here): the correlation coefficients fluctuate around zero for all synthesized SPs with different fractal characteristics. However, the signal of the SP of soil is seen in the $\bar{R}_{UV_{xyz}}^r(z)$ (Fig. 6.11): at ~ 300 m, the maximum positive correlation between the SP of REFSMC and UV_{xyz} is detected, while the maximum negative correlation (-10%) occurs at 1300 m. The positive correlation is a consequence of the surface layer parametrization (cf. equation 3.5a): as the soil moisture increases, the surface latent heat flux increases to transfer the soil moisture into the atmosphere and wind is generated to transport the moisture. The negative correlation at higher levels is due to the conservation of mass in a column of air.

6.1.3. Aerodynamic coupling by z_0

Temperature (T_{xyz}). There is a -5% negative correlation between the synthesized SP of z_0 and temperature close to the surface (Fig. 6.1b) which can be explained by an inverse relation between the characteristic temperature (θ_*) and z_0 (cf. equation 3.4b). As the thermal energy is increased due to the friction at the surface, it has to be compensated somewhere higher up. This happens above 1 km height in para-real simulations with the synthesized SP of z_0 . There is a positive correlation between the synthesized SP of roughness-length and T_{xyz} above this height.

Water-vapor (QV_{xyz}) and cloud-water (QC_{xyz}). The opposite behaviors are observed in the vertical profile of both water vapor (Figs. 6.1e) and cloud water (Fig. 6.1h): an up to $+5\%$ correlation between cloud-water and the synthesized SP of z_0 exists close to the surface, and a negative one unveils at heights above ~ 500 m. However, the maximum positive correlation ($+5\%$) between water-vapor and the synthesized SP of z_0 appears at about 500 m (more distance from the surface) while the maximum anti-correlation is found at the same height as the maximum positive-correlation between temperature and z_0 . These opposite behaviors result from the surface energy balance. However, in the previous section we found that its impact on the horizontally decomposed component of water-vapor is not significant.

Horizontal wind components (UV_{xyz}). Simulations forced by the synthesized SP of roughness-length clearly show the impact of the aerodynamic coupling on the vertical propagation of the SP: at the ground, there is a strong negative correlation (up to 20%) between the synthesized SP of roughness-length and UV_{xyz} (Fig. 6.1k), due to the inverse relation between the roughness-length and wind (cf. equation 3.3b). Because of the momentum conservation in a column of air, the large negative correlation close to the surface is compensated by the positive correlation higher up, i.e., if flow slows down close to the surface due to larger roughness-length, it has to speed up higher up (positive correlation between the surface roughness-length and higher-up velocity).

Vertical wind component (W_{xyz}). Despite the significant correlation between the synthesized SP of z_0 and $UV_{xyz}|_{z=z'}$, no signal from the synthesized SP of roughness-length is carried by the aerodynamic coupling into W_{xyz} . There is nearly no correlation between the synthesized SP of the roughness-length and the $W_{xyz}|_{z=z'}$ (not shown here). It is interesting to see that the different dimensionality of the vertical velocity variance is significantly affected by the aerodynamic coupling, in particular its total variance (cf. Section 5.1). But changing the roughness-length at the surface has no significant impact on the vertical propagation of the signal from the surface through the vertical velocity of the wind. Besides, the $W_{xyz}|_{z=z'}$ does not reveal the signature of the synthesized SP of z_0 . Any change of the roughness-length at the surface only perturbs the total variance of W through the wind shear stress.

6.1.4. Remarks

Based on the vertically anchored correlation analysis presented hereunto, patterns with larger spatial structure and higher persistency have the maximum values of correlation, regardless of the sign of the correlation. As the dominant scale (k_{max}) is kept constant, the correlation becomes stronger as the persistency of the patterns (s_2) is increased. Additionally, as the persistency of the synthesized SPs remains unchanged but the dominant length-scale increases (decrease of k_{max}), the correlation is enhanced.

The dynamic effect of the land-surface heterogeneity can carry the signal of the surface to the atmosphere aloft via the coupling mechanisms. However, it is length-scale dependent and it can not significantly impact on the propagation of the small-scale synthesized SP ($k_{max}=3$).

In section 5.2 where the vertical integration of the atmospheric states is involved in the analysis (cf. equation 5.2), the links between the surface signal and atmospheric states are hidden. However, here we unveil the vertical propagation of the surface signal by the

vertical anchoring of the correlation analysis. The 3D standing pattern of atmospheric variables (f_{xyz}) contributes to small fraction of the total variance (0.1-5%) and here, we find that, 5-20% of it is correlated with the synthesized SP. Therefore, this finding motivates the next section to study the correlation between the synthesized SP and the full stationary signal of the atmospheric states, which contributes to 12-52% of the total variance.

6.2. Vertical propagation of SSP into the full stationary eddy (f_{hz})

To achieve the full stationary eddy, all spatial decomposed components of ANOVA, which are independent of time, are merged as

$$\begin{aligned}
 f_{hz} &= f_{xyz} + f_{xz} + f_{yz} + f_{xy} + f_x + f_y + f_z \\
 \xrightarrow{(2.17)} &= P_{xyz}(x, y, z) - P_{xy}(x, y) - P_{yz}(y, z) - P_{xz}(x, z) + P_x(x) + P_y(y) + P_z(z) - P_\emptyset(\emptyset) \\
 &\quad + P_{xz}(x, z) - P_x(x) - P_z(z) + P_\emptyset(\emptyset) \\
 &\quad + P_{yz}(y, z) - P_y(y) - P_z(z) + P_\emptyset(\emptyset) \\
 &\quad + P_{xy}(x, y) - P_x(x) - P_y(y) + P_\emptyset(\emptyset) \\
 &\quad + P_x(x) - P_\emptyset(\emptyset) \\
 &\quad + P_y(y) - P_\emptyset(\emptyset) \\
 &\quad + P_z(z) - P_\emptyset(\emptyset) \\
 &= P_{xyz}(x, y, z) - P_\emptyset(\emptyset) \xrightarrow{(2.16)} \int F(x, y, z, t) dt - \iiint F(x, y, z, t) dx dy dz dt. \quad (6.2)
 \end{aligned}$$

$f_{hz}(z = z')$ indicates the eddy of a specific atmospheric state variable explaining the total spatial effects on the total variance at a specific height. Then, the correlation between the synthesized SP and $f_{hz}(z)$ of selected atmospheric state variables is calculated. To have statistically stable results, the mean of correlation over 10 rr is also computed. According to Ex. (6.1), $\bar{R}_{N_{hz}}^M(z)$ is given in Fig. 6.2. The correlation of the vertical velocity (W_{hz}) and the synthesized SP is very small ($\bar{R}_{W_{hz}}^M(z) \sim 0$) which is not shown here.

As already discussed in sections 5.2 and 6.1, the larger the pattern, the stronger the couplings. Besides, the signal of the synthesized SPs with $k_{max}=3$ (length-scale=0.3 km) is not propagated by the main couplings (black curves in Fig. 6.2), except the two cases mentioned in the section 6.1: (1) propagation of the noisy-SP in QV through the hydrological coupling and (2) in UV through the aerodynamic coupling.

In addition, when the f_{hz} is considered, the correlation between the full stationary com-

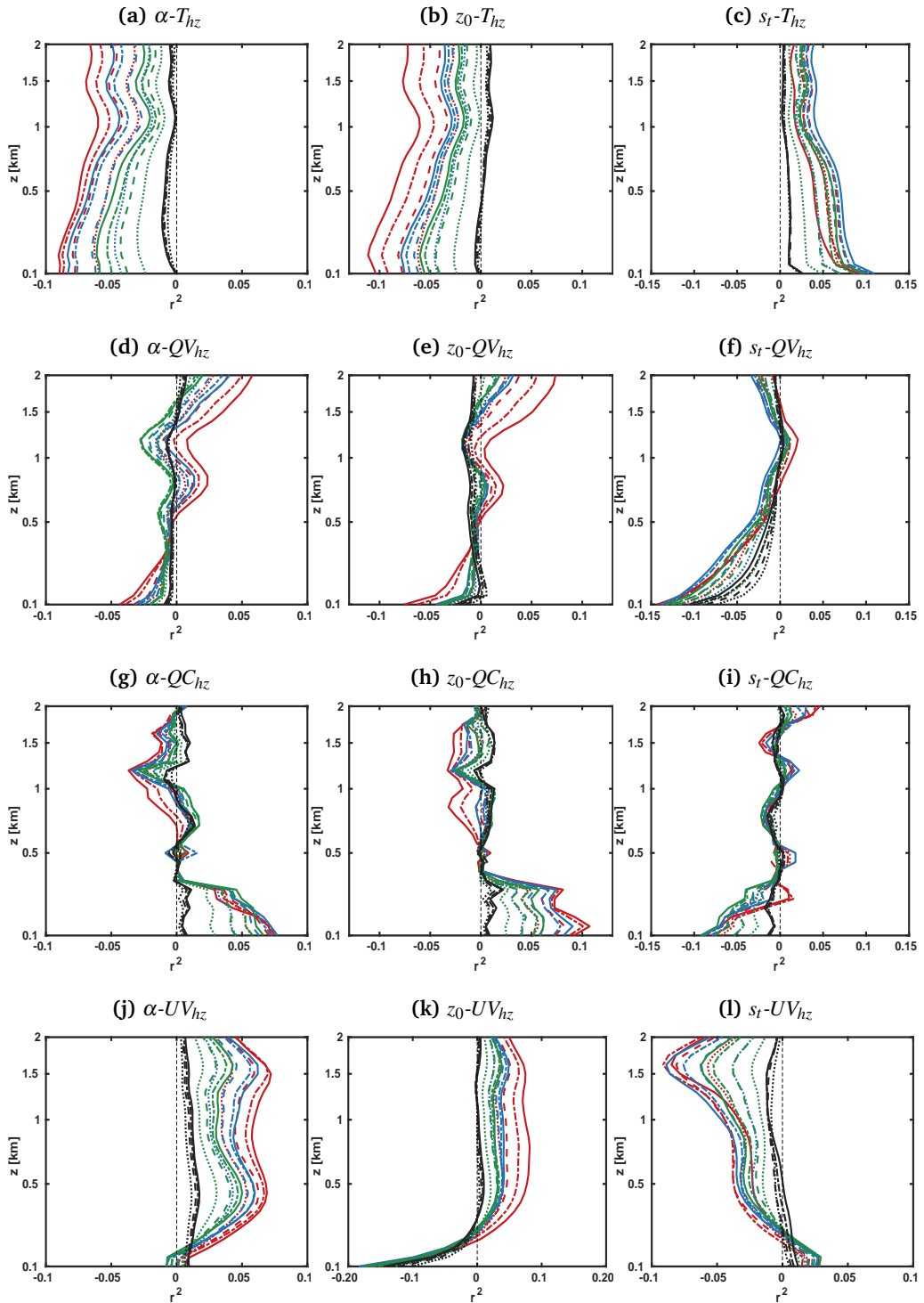


Figure 6.2.: Vertical profile of the correlation between the synthesized SPs of three surface properties (α (left column), z_0 (center column), and s_t (right column)) and the T_{hz} (a, b, c), QV_{hz} (d, e, f), QC_{hz} (g, h, i), and UV_{hz} (j, k, l). The axes and colors are similar to Fig. (6.1).

ponents of ANOVA and the synthesized SP exhibits less fluctuations around zero and the correlation coefficients are relatively larger than section 6.1. This means that the signal from the surface is more coherent in $f_{hz}(z')$ than in $f_{xyz}(z')$. In other words, the new arrangement of the considered surface properties affects all combination of the spatial dimensions of the atmospheric state variables and not only the 3D standing ANOVA component. In fact, f_{xyz} deliberately excludes other spatial ANOVA decomposed components, in particular f_{xy} . We expect f_{xy} to carry the largest effect of the surface compared to other ANOVA components.

6.2.1. Thermodynamic coupling via α

Temperature (T_{hz}). When the partitioning of the surface albedo is changed, the synthesized SP of α and T_{hz} are significantly anti-correlated (5-10%) (Fig. 6.2a) up to 2 km height. This reflects the reduction of sensible heat flux into the atmosphere due to a brighter surface. It is interesting to observe that the albedo signal is almost consistently propagated in T_{hz} up to 2 km height, in comparison with T_{xyz} which does not include T_{xy} . T_{xy} contains the main signal from the surface and here we observe its important role on the vertical propagation of the signal from the surface.

Water-vapor (QV_{hz}). A change of surface albedo has two main impacts on water-vapor (Fig. 6.2d): (1) a direct impact through latent heat flux with its role mainly observable at the surface, (2) an indirect impact via the surface energy balance which mainly plays a role above 500 m. At the lowest vertical level, the negative correlation indicates less evaporation, thus, less water-vapor, due to a large surface albedo (impact #1). This direct impact of large albedo close to the surface is large enough to overcome the indirect impact of change of α (impact #2). As the signal from the surface propagates upwards, the first impact decreases and in turn, the second impact comes into account. Due to the surface energy balance, a positive correlation appears above 500 m to compensate the large change of sensible heat flux due to the change of α . The darker surface reflects an increase of sensible heat flux and in turn, a reduction of the latent heat flux.

Cloud-water (QC_{hz}). The significant positive correlation between the synthesized SP of α and QC_{hz} below 300 m is certainly not due to the convective cloud close to the surface. The time series of domain integrated cloud-water below 500 m (Fig. 6.3) shows the nighttime fog which is the reason of this significant positive correlation at the lowest vertical level. On the other hand, QC above 500 m is confined to the daytime convective clouds (Fig. 6.3). However the strength of daytime QC is very small relative to nighttime QC. Thus, almost zero correlation is seen above 500 m.

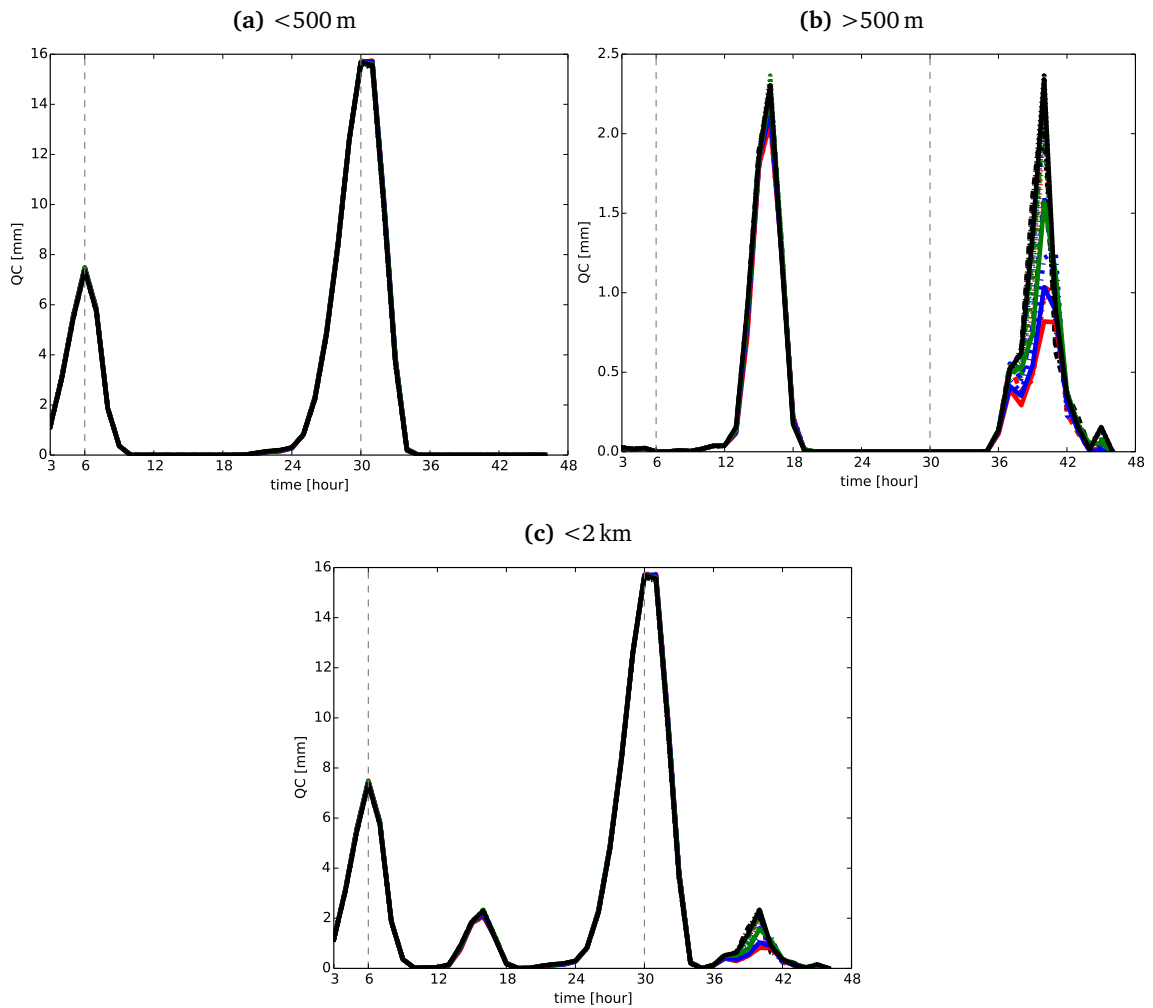


Figure 6.3.: Time series of integrated cloud-water below 500 m (a), in an atmospheric layer between 500 m and below 2 km (b), and below 2 km (c) for para-real simulations forced by s_r . The color of curves is similar to Fig. 6.1.

Horizontal wind (UV_{hz}). The horizontal velocities are positively correlated with the synthesized SP of albedo (Fig. 6.2j). This is due to a decrease of the daytime heat fluxes with higher albedo that leads to less turbulent mixing and thus steeper gradients in the mean velocity profiles.

6.2.2. Hydrological coupling via s_t

Water-vapor (QV_{hz}) and cloud-water (QC_{hz}). The hydrological coupling is considerably affected by the new arrangement of the soil-type, since soil directly alters the availability of the moisture in the overlaying atmosphere. The synthesized SP of the REFSMC and water content are strongly anti-correlated at the surface, i.e., -15% anti-correlation with water-vapor which decreases to the zero-correlation up to 1 km (Fig. 6.2f). There is 10% anti-correlation between the synthesized SP of s_t and QC_{hz} which decreases to the zero-correlation up to 500 m (Fig. 6.2i). The QC below 500 m is the nighttime fog (cf. Fig. 6.3).

Temperature (T_{hz}). When the latent heat flux (LE in eq. 1.1) is changed due to the change of the atmospheric moisture, the sensible heat flux (H in eq. 1.1) is accordingly changed to preserve the surface energy balance. Consequently, we see an opposite sign in the correlation between the synthesized SP of REFSMC and temperature (Fig. 6.2c), i.e., +10% positive-correlation with the atmospheric temperature consistently up to 2 km.

Horizontal wind (UV_{hz}). Based on the latent heat flux parametrization (cf. equation 3.5a), the friction velocity (u_*) exhibits an inverse relation with the moisture scale (q_*), and a direct relation with q_0 . This can also be observed in the correlation analysis: a positive correlation between s_t and UV_{hz} at the lowest vertical level (Fig. 6.2l), and a negative correlation between soil-moisture and UV_{hz} . In comparison to the same correlation analyses but with UV_{xyz} (Fig. 6.1l), the positive correlation signal propagates up to 500 m while it is limited here to the lowest vertical level.

6.2.3. Aerodynamic coupling via z_0

Temperature (T_{hz}). The negative correlation between the synthesized SP of z_0 and T_{hz} (Fig. 6.2b) can be explained through the sensible heat flux parametrization (cf. 3.4a). The negative correlation up to 2 km without changing the sign of the correlation at different levels is consistent with our finding in subsection 5.2.3. When T_{xy} is included in the analysis, the strong signal of the surface is transferred via aerodynamic coupling.

Water-vapor (QV_{hz}). A rougher surface causes more friction and, thus, reduction of wind velocity (u_* decreases). In the latent heat flux parametrization (cf. equation 3.5b), u_* and q_* are reversely related and, thus, directly related to q_0 . Therefore, there is a negative correlation between z_0 and QV_{hz} close to the surface (Fig. 6.2e). Above 500 m the positive correlation between z_0 and q_* appears up to 2 km.

Cloud-water (QC_{hz}). The nighttime cloud-water below 500 m (nighttime fog) is considerably larger than daytime cloud-water (daytime fog), due to the reduced mixing at nighttime (cf. Fig. 6.3). Thus, a significant positive correlation exists between QC_{hz} and z_0 below 500 m (Fig. 6.2h) and an almost zero correlation is revealed above this height.

Horizontal wind (UV_{hz}). UV_{hz} is negatively correlated with the synthesized SP of z_0 close to the surface, because of an inverse relation between z_0 and wind close to the surface (cf. log-wind-profile in eq. 3.3b). The positive correlation is exhibited far above the surface because the momentum conservation has to be kept (Figs. 6.2j). On the other hand, when the sum of all spatial ANOVA components is considered (UV_{hz}), the impact of length-scales of SPs on the aerodynamic coupling is more distinguishable than UV_{xyz} . Hence, the signal from the surface is more coherent when UV_{xy} is included in the analysis.

6.2.4. Remarks

The fluctuation around zero in Fig. 6.2 is less than Fig. 6.1. The reason is that f_{hz} includes all spatial components of ANOVA which are independent of time, especially \mathbf{f}_{xy} . We believe that \mathbf{f}_{xy} contains the largest effects of the new surface forcing. Therefore, the signal is more coherent and it is consistently propagated.

The less randomized the synthesized SPs, the larger the correlation. So in terms of fractal surface parameters: the larger the dominant scale, the stronger the correlation, and, the higher the persistency, the stronger the correlation (regardless of the sign of correlation coefficients).

The correlation analyses reveal that the dynamic effect of land-surface heterogeneity can substantially affect the atmospheric states variables through the thermodynamic, hydrological, and aerodynamic coupling mechanisms. We change the partitioning of a single forcing from the surface properties and all other forcings remain unchanged; we find that the dynamic effect carries information about the new arrangement of the surface property into the atmosphere aloft and 5-20% of variability of an atmospheric state variables at a particular height can be explained only by the synthesized SP.

The dynamic effect depends significantly on the length-scale of the imposed synthesized SP: the larger the scale of the synthesized SP, the more effective the dynamic effect. While the surface signal does not affect the bulk structure of atmospheric boundary layer, regardless of which surface properties is used for forcing (cf. Fig. A.1), the impact of the soil-moisture signal is significant on integrated cloud-water above 500 m on the second day of the simulation (cf. Fig. 6.3). On the contrary, the smallest-length scale synthesized SP of soil reveals the strongest signal on the bulk structure of cloud-water on the second day of the simulation and it doubles the amount of cloud-water above 500 m.

These notable findings of the vertical propagation of the surface signal by the main couplings motivate us to study the temporal propagation of the surface signal. Here, we want to understand whether it is possible to explain the variability of a specific atmospheric state variable at a particular time step only by knowing the SP.

6.3. Temporal propagation of the surface heterogeneity in a horizontal/temporal decomposed component of atmospheric states (f_{xyt})

In this section, we consider f_{xyt} of ANOVA decompositions of the selected atmospheric state variables. Then, the correlation between the synthesized SP and f_{xyt} at a particular time step ($t = t'$) is calculated. Besides, the mean of the correlation over 10 rr is calculated: $\bar{R}_{N_{xyt}}^M(t = t')$ where $M \in \{\alpha, z_0, s_t\}$ and $N_u \in \{T_{xyt}, QV_{xyt}, QC_{xyt}, UV_{xyt}, W_{xyt}\}$ (Fig. 6.4).

6.3.1. Thermodynamic coupling through α

We find that the correlation between the synthesized SP of α and f_{xyt} of all identified atmospheric states is insignificant and very small ($|\bar{R}_{N_{xyt}}^\alpha(t = t')| < 10^{-3}$ where $N_{xyt} \in \{T_{xyt}, QV_{xyt}, QC_{xyt}, UV_{xyt}, W_{xyt}\}$). Thus, $\bar{R}_{N_{xyt}}^\alpha(t = t')$ is not shown in this section. The diurnal cycle does not show up in any of the para-real simulations forced by different length-scales of the synthesized SP of surface albedo. Moreover, different fractal parameters (different s_2 and k_{max}) of the surface albedo heterogeneity do not play a role in the temporal propagation of the albedo signal in f_{xyt} of any atmospheric states.

6.3.2. Hydrological coupling through s_t

Hydrological coupling also does not transfer the signal of soil-moisture into QC_{xyt}, UV_{xyt} and W_{xyt} . However, the signal is relatively large and significant in T_{xyt} (Fig. 6.4a) and

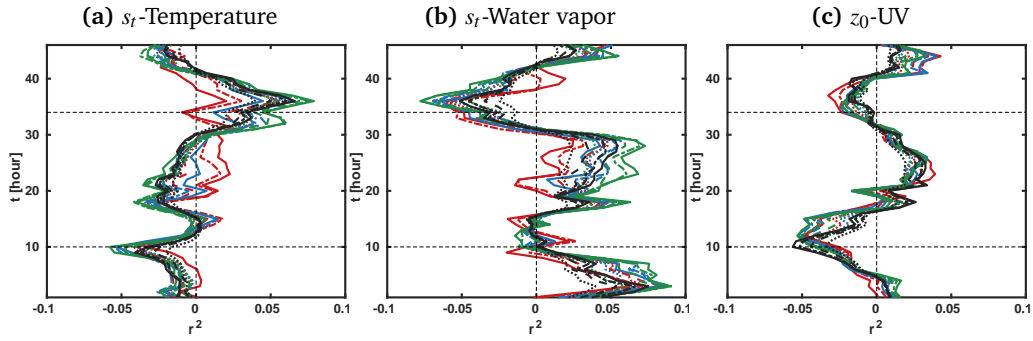


Figure 6.4.: Time series of the correlation between the synthesized SPs of s_t and the T_{xyt} (a), and QV_{xyt} (b), and between the synthesized SP of z_0 and UV_{xyt} (c). The colors are similar to Fig. (6.1). The horizontal black dashed lines indicate noon time of the two days of the simulations at UTC time scale.

QV_{xyt} (Fig. 6.4b). A significant correlation between the synthesized SP of REFSMC and the QV_{xyt} (5-8%) is unveiled at two time steps (Fig. 6.4b): (1) at the beginning of the first day (positive-correlation at 4th time step) and (2) 12 UTC on the second day (negative-correlation at 34th time step) of the para-real simulations. It is interesting to observe that the maximum anti-correlation shows up on the second day of the simulations. It indicates a time-delay to get a strong signal from the soil-moisture in QV_{xyt} . As mentioned by LIU AND SHAO [2013], the soil response is highly time-scale dependent. The positive correlation at the beginning of the simulation is due to nighttime fog. The surface signal in water-vapor induces an inverse response in the atmospheric temperature but some hours later, i.e., 5% anti-correlation of T_{xyt} and soil-moisture at 12 UTC of first day. There is also a significant positive correlation during the nighttime of the second day of para-real simulations caused by a reduction of mixing during the night. However, by sunrise, the mixing starts to grow until noontime of the second day when we see the maximum anti-correlation of QV_{xyt} and the synthesized SP of s_t .

At 12 local time (UTC+2) of the second day of the simulations, T_{xyt} exhibits a feedback on the change of the atmospheric moisture to preserve the surface energy balance (Fig. 6.4a). The 5-8% positive correlation reveals between T_{xyt} and the SP of the REFSMC at noon of 25th of April 2013.

The large scale SPs ($k_{max}=0.1$ and 0.5 (red and blue curves, respectively)), which in previous sections show the largest correlation, here at some time steps show an opposite behavior, and the $\bar{R}_{QV_{xyt}}^{s_t}(t=t')$ for them are smaller than for the small scale SPs ($k_{max}=1$ and 3 (green and black curves, respectively)). It indicates that the more randomized SSPs induce more mixing in T_{xyt} and QV_{xyt} at some time steps. This finding is similar to the time-series of cloud-water on the second day of simulation, i.e., the smallest-length scale SSP of soil doubles cloud-water of atmosphere above 500 m.

6.3.3. Aerodynamic coupling through z_0

The maximum anti-correlation (-5%) between the synthesized SP of z_0 and UV_{xyt} occurs at 12 UTC of the first day (Fig. 6.4c) which is explained by an inverse relation between the z_0 and u_* (cf. equation 3.3b). The diurnal cycle is weakly observed after this time step (less than 5%), e.g. a positive correlation at nighttime due to a reduced mixing and, again, a negative correlation by sunrise as a result of an increase of mixing during the day until noon.

The impact of different length-scale of the synthesized SPs is not significant in this analysis and they affect almost similarly the UV_{xyt} . Moreover, f_{xyt} that of other atmospheric states are not significantly affected by aerodynamic coupling and they exhibit very weak correlation ($|\overline{R}_{N_{xyt}}^{z_0}(t=t')| < 10^{-3}$ where $N_{xyt} \in \{T_{xyt}, QV_{xyt}, QC_{xyt}, W_{xyt}\}$) (not shown).

6.3.4. Remarks

On the second day of simulation, in particular, we find the maximum correlation ($\sim 10\%$) between this single horizontal/temporal and the synthesized SP of the surface properties. The f_{xyt} hold 0.4-5% of the total signal which is small in comparison with f_{hz} . However, the diurnal cycle is found in the three cases mentioned above. This promotes the correlation analysis to look at a merged component which includes all temporal and horizontal ANOVA decomposed components.

6.4. Temporal evolution of the SSP effect on the total z-independent decomposed components of atmospheric variables (f_{ht})

To keep the parallel with sections 6.1 and 6.2, all ANOVA decomposed components independent of z are merged to include all variabilities in x , y , and t dimensions of considered atmospheric variables:

$$\begin{aligned}
 f_{ht} &= f_{xyt} + f_{xt} + f_{yt} + f_t + f_{xy} + f_x + f_y \\
 \xrightarrow{(2.17)} &= P_{xyt}(x, y, t) - P_{xy}(x, y) - P_{yt}(y, t) - P_{xt}(x, t) + P_x(x) + P_y(y) + P_t(t) - P_\emptyset(\emptyset) \\
 &\quad + P_{xt}(x, t) - P_x(x) - P_t(t) + P_\emptyset(\emptyset) \\
 &\quad + P_{yt}(y, t) - P_y(y) - P_t(t) + P_\emptyset(\emptyset) \\
 &\quad + P_t(t) - P_\emptyset(\emptyset) \\
 &\quad + P_{xy}(x, y) - P_x(x) - P_y(y) + P_\emptyset(\emptyset)
 \end{aligned}$$

$$\begin{aligned}
& + P_x(x) - P_0(\emptyset) \\
& + P_y(y) - P_0(\emptyset) \\
& = P_{xyt}(x, y, t) - P_0(\emptyset) \xrightarrow{(2.16)} \int F(x, y, z, t) dz - \iiint F(x, y, z, t) dx dy dz dt. \quad (6.3)
\end{aligned}$$

Then, $\bar{R}_{N_{ht}}^M(t)$ is computed and displayed in Fig. 6.5. The last three components, f_{xy} , f_x , and f_y , are in common with section 6.2. In all three couplings, $\bar{R}_{N_{ht}}^M(t)$ for the smallest length scale (k_{max}) is very small and fluctuates randomly around zero. However, other scales of SSPs unveil a very large correlation between the SSP and f_{ht} of atmospheric states. The $\bar{R}_{N_{ht}}^M(t)$ is twice as large as $\bar{R}_{N_{xyz,ht}}^M(z)$ ($|\bar{R}_{N_{ht}}^M(t)| \simeq 10-40\%$ versus $|\bar{R}_{N_{xyz,ht}}^M(z)| \simeq 5-20\%$). Similar to sections 6.1 and 6.2, the larger the length scale of the synthesized SP, the stronger the correlation; regardless of the sign.

6.4.1. Thermodynamic coupling via α

Temperature (T_{ht}). A negative correlation exists between T_{ht} and the synthesized SP of all length-scales at all time steps (Fig. 6.5a) due to the opposite behavior between the surface albedo and the available energy at the surface: the brighter the surface (large α), the lesser is the energy transferred as a sensible heat flux to the atmosphere aloft. There are two peaks in the time-series of the correlation analyses: 12 UTC of the first and second day of the para-real simulations, when the sun has its maximum effect on the surface energy balance during the simulations. Besides, the diurnal cycle is unveiled in $\bar{R}_{T_{ht}}^\alpha(t)$ and there are two minima during nighttime due to sunset.

Water-vapor (QV_{ht}). In turn, the latent heat flux responses to the change of sensible heat flux to keep the surface energy balance (Fig. 6.5d), however it has some time steps delay. The maxima of $\bar{R}_{QV_{ht}}^\alpha(t)$ show up in the afternoon (not at noon time) of the para-real simulations.

Cloud-water (QC_{ht}). The sudden change at the beginning of $\bar{R}_{QC_{ht}}^\alpha(t)$ might be due to sunrise and the sudden change of surface energy (Fig. 6.5g). After 6 UTC of the first day of the simulation, the correlation between α and QC_{ht} is always positive because larger albedo leads to less sensible heat flux and in turn, more latent heat flux, thus, more evaporation. There is another sudden increase again at 6 UTC, however on the second day of the simulation. This is again because of sunrise and its subsequent increase of mixing.

Horizontal wind (UV_{ht}). Around noon time, when the maximum effect of surface albedo plays a dominant role, there are two peaks of anti-correlation between the synthesized SP

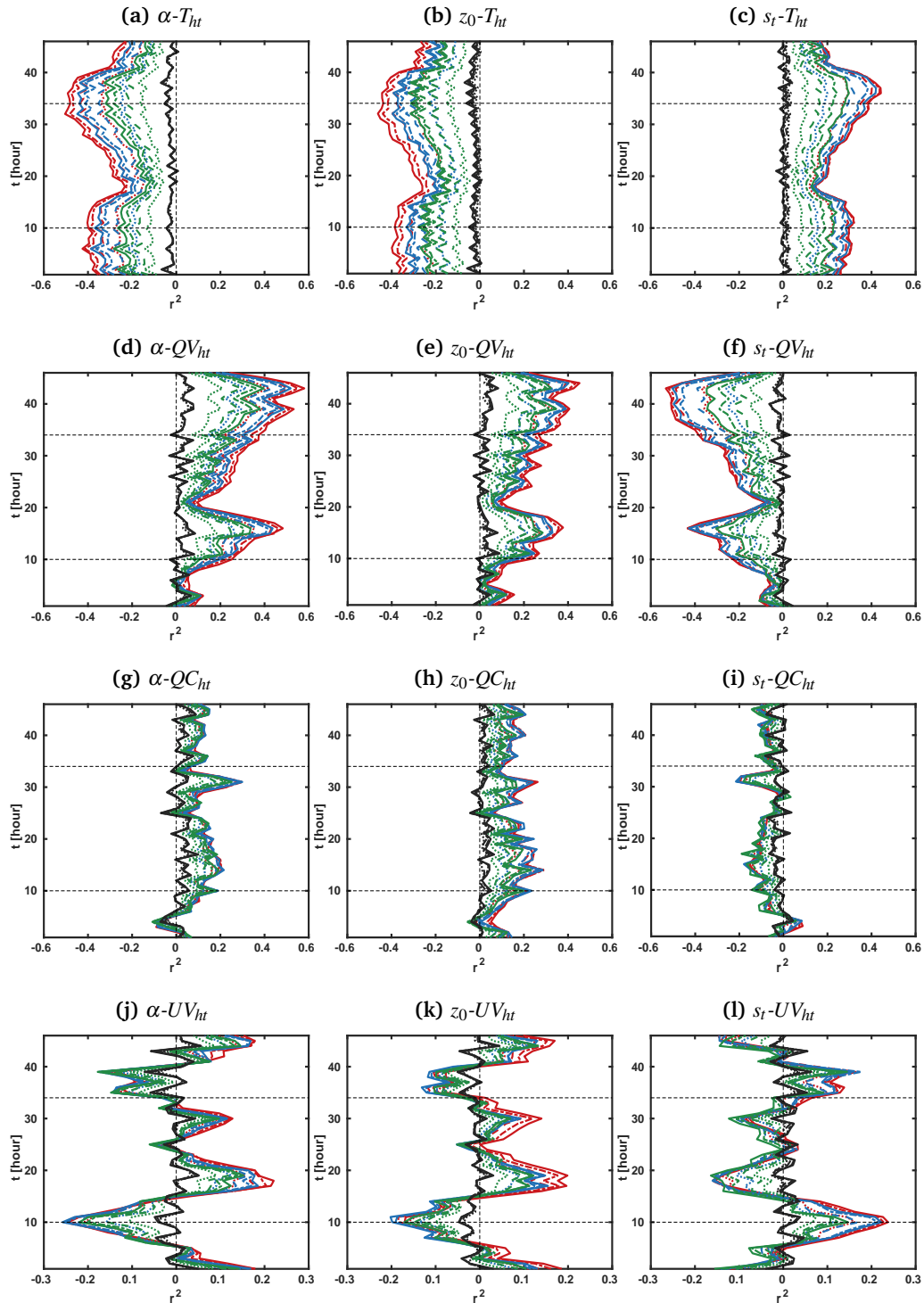


Figure 6.5.: Time series of the correlation between the synthesized SPs of three surface properties, α (left column), z_0 (middle column), s_r (right column) and for T_{ht} (a, b, c), QV_{ht} (d, e, f), QC_{ht} (g, h, i), and UV_{ht} (j, k, l). The axes and colors are similar to Fig. (6.4).

of α and UV_{ht} with the magnitude of 10-20% (Fig. 6.5j). Larger α leads to more reflection and thus less energy from the sun at the surface. Consequently, the mixing close to the surface is reduced which causes less wind. As the synthesized SPs are in xy direction, their dominant effect is unveiled in horizontal wind (UV_{ht}) rather than vertical wind (W_{ht}). Therefore, we do not show $\bar{R}_{W_{ht}}^\alpha(t)$ here. In the evening transitions, when the effect of surface albedo goes to zero due to sunset, $\bar{R}_{UV_{ht}}^\alpha(t)$ also goes to zero. During nighttime, it goes to positive coefficients. This indicates the development of the stable nighttime boundary layer.

6.4.2. Hydrological coupling via s_t

Water-vapor (QV_{ht}). All synthesized SPs of soil-moisture with different fractal parameters exhibit the anti-correlation between the synthesized SP of s_t and QV_{ht} (Fig. 6.5f). There is only an exception for the synthesized SPs with $k_{max}=3$ which $\bar{R}_{QV_{ht}}^{s_t}(t)$ fluctuates randomly around zero. The negative correlation is as a result of an inverse relation between the soil capacity to hold moisture and the amount of water vapor released into the atmosphere aloft. The diurnal cycle of $\bar{R}_{QV_{ht}}^{s_t}(t)$ is observed and, during nighttime, the correlation decreases due to sunset and the resulting stable boundary layer. The minima peaks occur at the end of each day (at 24 UTC), the maxima peaks, however, occur in the afternoon (not noon time). This delay in detecting the largest $\bar{R}_{QV_{ht}}^{s_t}(t)$ for each day is due to the time-dependent soil response to the surface forcing.

By including 1D/2D horizontal and temporal ANOVA decomposed components in the correlation analysis, the temporal signal is more coherent than $\bar{R}_{QV_{xyt}}^{s_t}(t)$ (cf. Fig. 6.4b). This significant difference between QV_{xyt} and QV_{ht} is as a result of excluding QV_{xy} , QV_x , and QV_y from QV_{xyt} which is done deliberately by ANOVA method. Thus, the most important signal of surface which is expected to exist in xy dimensions, is not considered in $\bar{R}_{QV_{xyt}}^{s_t}(t)$.

Temperature (T_{ht}). In response to the change of water-vapor, T_{ht} is changed accordingly to preserve the surface energy balance (Fig. 6.5c). The positive correlation at the beginning of the simulation starts to grow until noontime, because, by sunrise, more evaporation occurs, thus more moisture is released by soil to the atmosphere. Hence, the sensible heat flux and atmospheric temperature is reversely changed. The second maximum of $\bar{R}_{T_{ht}}^{s_t}(t)$ on the second day appears around noontime of the second day of the para-real simulation with synthesized SP of soil. At the evening transitions on both days, the minima of $\bar{R}_{T_{ht}}^{s_t}(t)$ occur due to sunset. Similar to $\bar{R}_{QV_{ht}}^{s_t}(t)$, $\bar{R}_{T_{ht}}^{s_t}(t)$ is considerably larger than $\bar{R}_{T_{xyt}}^{s_t}(t)$ (cf. Fig. 6.4a).

Cloud-water (QC_{ht}). On the first day of the simulation, no clouds are observed. Therefore, the sudden change from a positive to a negative correlation in the morning transition of the first day of the para-real simulation is due to the nighttime fog (Fig. 6.5i). Until the next morning transition, $\bar{R}_{QV_{ht}}^{s_t}(t)$ is constant. Then, there is a sudden increase again at the morning transition, due to nighttime fog.

Horizontal wind (UV_{ht}). Because of an increase of evaporation during the day, we see positive $\bar{R}_{UV_{ht}}^{s_t}(t)$ after the morning transition (Fig. 6.5l) and the peak of positive correlation is around noon on both days. During nighttime, the zero or anti-correlation between horizontal wind and s_t is unveiled as a result of the stable boundary layer developed at night and causing less evaporation and, thus, less wind.

6.4.3. Aerodynamic coupling via z_0

Temperature (T_{ht}). Based on the surface layer parametrization (cf. equation 3.4b) showing an inverse relation between the z_0 and θ_* , negative $\bar{R}_{T_{ht}}^{z_0}(t)$ is exhibited every time steps (Fig. 6.5b). However, it decreases around evening transitions and again increases during morning transitions. The peak of maxima of $\bar{R}_{T_{ht}}^{z_0}(t)$ are observed at noon time of both days. The rougher the surface, the smaller the u_* which leads to less sensible heat transfer (H) to the atmosphere aloft.

Water-vapor (QV_{ht}). On the other hand, the less H induces more latent heat flux to preserve the surface energy balance. Hence, the positive $\bar{R}_{QV_{ht}}^{z_0}(t)$ is revealed in Fig. 6.5e. Similar to $\bar{R}_{QV_{ht}}^\alpha(t)$ and $\bar{R}_{QV_{ht}}^{s_t}(t)$, the response from latent heat flux has some hours delay and the maxima of $\bar{R}_{QV_{ht}}^{z_0}(t)$ turn out in the afternoons.

Cloud-water (QC_{ht}). The positive $\bar{R}_{QC_{ht}}^{z_0}(t)$ for all time steps can be explained as a correlation between fog and z_0 , in particular, a sudden peak at the morning transition on the second day (Fig. 6.5h). The diurnal cycle in $\bar{R}_{QC_{ht}}^{z_0}(t)$ is not as clear as other atmospheric states.

Horizontal wind (UV_{ht}). The two maxima of negative $\bar{R}_{UV_{ht}}^{z_0}(t)$ occur at noon time of both days of the simulation, as a result of log wind profile which is similar to Fig. 6.4c. However, the values of $\bar{R}_{UV_{ht}}^{z_0}(t)$ are significantly larger than $\bar{R}_{UV_{xyt}}^{z_0}(t)$ and the impact of different length scales of the synthesized SPs is clearer: the smaller the k_{max} of SSPs, the stronger the $\bar{R}_{UV_{ht}}^{z_0}(t)$. Here, the inter-relation of the three couplings is unveiled: during night when the boundary layer is stable, less mixing occurs, and flux-gradient relationship can be

broken, as the pattern of a synthesized SP of roughness-length has a larger length-scale, the reduction of horizontal wind due to friction is less dominant in the whole domain. Therefore, positive $\bar{R}_{UV_{ht}}^{z_0}(t)$ is observed during nighttime of the para-real simulation forced by synthesized SP of z_0 .

6.4.4. Remarks

For the analysis of this section, the full 2D horizontal eddy, $f_{xy} + f_x + f_y$, is included and the important fraction of the total signal exists in f_{ht} . We find that the sign of $\bar{R}_{N_{ht}}^M(t)$ here is consistent with our finding in section 5.2 (cf. Fig. 5.3), where we computed the correlation between the synthesized SP and the full 2D standing atmospheric signal ($r^2(SSP_{xy}^i, \mathbf{f}_{xy}^i)$). The signal of \mathbf{f}_{xy} is strong enough that the day transitions can not significantly change its temporal evolution. However, the sign of $\bar{R}_{UV_{ht}}^M(t)$ is consistent with $r^2(SSP_{xy}^i, \mathbf{UV}_{xy}^i)$ only during nighttime of the simulations, when the atmospheric boundary layer is stable. It indicates that horizontal wind is highly sensitive to the external forcings.

Here, f_{ht} is explained up to a third of the total signal and this amount is relatively larger than others considered ANOVA components (\mathbf{f}_{xy} , f_{xyz} , f_{hz} , and f_{xyt}). It indicates that the dependency of the surface-atmosphere couplings on time is as important as their dependency on the full horizontal forcing. When these components (\mathbf{f}_{xy} and all time-dependent components) are considered (as we did here), there is a chance up to 20% to explain an atmospheric signal by the surface pattern (cf. Table 6.2).

Table 6.2.: Maximum chance to explain an atmospheric signal by a single couplings through the corresponding surface property: $E_u^M = S_u^M \times |\bar{R}_{N_u}^M|_{max}$. Colors indicate different couplings: thermodynamic (red), aerodynamic (green), and hydrological (blue) coupling.

	T	QV	QC	UV
E_{xyz}^α	0.01	0.03	0.12	0.05
$E_{xyz}^{z_0}$	0.01	0.04	0.21	0.20
E_{xyz}^{st}	0.02	0.12	0.21	0.06
E_{hz}^α	7.77	3.68	0.95	2.18
$E_{hz}^{z_0}$	5.77	4.91	1.45	5.49
E_{hz}^{st}	6.64	9.20	1.63	2.70
E_{xyt}^α	0	0	0	0
$E_{xyt}^{z_0}$	0	0	0	0.09
E_{xyt}^{st}	0.03	0.30	0	0
E_{ht}^α	18.40	16.32	3.10	12.95
$E_{ht}^{z_0}$	14.70	11.40	3.14	13.32
E_{ht}^{st}	14.90	16.64	3.33	12.92

Table 6.2 provides the maximum chance to explain an atmospheric signal by a synthesized SP of a single surface property for each considered atmosphere-surface coupling, separately. E_u^M is computed as a multiplication of the sensitivity index (S_u^M) and the maximum absolute value of the correlation coefficient ($|\bar{R}_{N_u}^M|_{max}$), where u indicates the dimension of ANOVA components, M shows the surface properties studied here, and N_u illustrates the considered ANOVA components. The largest chance is found when f_{ht} is considered and the maximum possibility for each considered atmospheric state is observed when the direct impact of couplings is considered, e.g., the impact of thermodynamic coupling on atmospheric temperature, the effect of hydrological coupling on atmospheric humidity, and the influence of aerodynamic coupling on wind. After f_{ht} , it is verified that f_{hz} shows up 10% chance to explain the atmospheric states by the surface signal. However, the atmosphere-surface couplings do not significantly affect the single ANOVA decomposed components of atmospheric state variables (f_{xyz} and f_{xyt}) and there is less than 1% chance to explain these single components only by knowing the SP.

7. Summary and discussion

In the present work, the dynamic effect of land-surface–atmosphere coupling mechanisms is studied (Section 1.3) using the Weather Research and Forecasting (WRF) model in its advanced research mode together with the Noah-MP land surface model (Chapter 3). The focus is on the three inter-related surface–atmosphere coupling mechanisms namely, thermodynamic, aerodynamic and hydrological coupling. For each coupling mechanism, we select a corresponding surface property–albedo (α), roughness-length (z_0), and soil-type (s_t)– in order to study the impact of its heterogeneity with different length-scale and persistency on the atmospheric boundary layer development. To do so, we introduce a novel approach called a '*para-real*' ensemble modelling where each simulation uses the same full complexity of real boundary conditions but is forced by a synthesized surface pattern of the surface properties (Section 2.1).

7.1. Para-real ensemble modelling as a new approach to coupled land–atmosphere modelling

The synthesized SPs (SSPs) are generated from a tailored randomized spectrum approach termed quasi-fractional Brownian surface (quasi-fBs). The quasi-fBs is based on the estimation of real heterogeneity parameters from original geo-data (Section 2.2.2). In fact, the quasi-fBs is a random 2D surface generated through a Fourier-Spectral approach as a realization of a Brownian process. The PDF of the SSPs match those of the original SP to minimize effects on the bulk surface energy balance. Indeed, only the surface properties are reshuffled in space such that the new spatial arrangement does not affect flux aggregation. Since the synthesized SPs are random fractals, we generate a series of random realizations (rr) with identical heterogeneity parameters to ascertain that the results are independent of the particular realization of the underlying random process (Section 4.2).

An ensemble of 48×10 para-real simulations is used here to study the coupling mechanisms (Section 2.3). That is, in total we analyze 480 simulations for 48 different physical parameter configurations and use 10 different random realizations of the surface boundary condition (ensemble members) for each case. The output is analyzed by conventional

averaging (Section 4.1), ANOVA sensitivity index analysis (Section 5.1), ANOVA decomposed components and through a comprehensive correlation analysis (Section 5.2 and Chapter 6). This allows us to investigate the impact of the length-scale and fractal persistency at the surface exerted on the atmospheric state.

7.2. Insights from para-real ensemble modelling to individual land–atmosphere coupling mechanisms

The **thermodynamic coupling** is found to be rather weak in general. When considered in terms of ANOVA sensitivity indices, there is no significant impact of the thermodynamic coupling through the surface-albedo (α) on the partitioning of subspace variances of the atmospheric variables. That means, despite a pronounced structural reorganization of the surface (that is in the horizontal direction), the variance partitioning accessible through a classic ANOVA analysis is not affected in favor of the horizontal direction. A more detailed analysis in terms of averages and combinations of decomposed ANOVA components, however, unveils that up to 10% of the full 2D standing eddy of temperature variance can be explained through the sensible heat flux. In fact, the albedo signal consistently propagates up to 2 km height. The maximum correlation between the SSP of albedo and the atmospheric temperature is found at noontime. Furthermore, the albedo pattern affects considerably the atmospheric humidity, in particular cloud-water. In fact, the largest-scale albedo pattern explains up to 10% of nighttime fog.

Similar to that of thermodynamic coupling, the influence of the **aerodynamic coupling** is not quantifiable through ANOVA sensitivity index analyses. Also, the expected impact of the aerodynamic coupling on the wind component (a negative correlation due to slow-down of near-surface wind with higher roughness) is not found in the full 2D standing component of the wind, because height is integrated in this component, thus, hiding the slow-down that is confined to a thin layer in vicinity of the surface. If, however, the height dependence is included in the analysis, we find 20% anti-correlation of the roughness-length with the horizontal wind close to the surface. Moreover, the aerodynamic coupling is highly sensitive to the diurnal cycle due to the stable boundary-layer at night, where the linearity of the flux-gradient relationship in only the aerodynamic components is broken down as a consequence of temperature stratification.

The **hydrological coupling** is found to be most important for the atmospheric boundary layer development (up to 2 km height studied here). It primarily acts through modification of the moisture availability and a corresponding repartitioning of the energy surplus at the surface to sensible and latent heat flux. When the SP of soil changes, the hydrological coupling significantly affects the partitioning of variance to the dimensional subspaces

considered through ANOVA sensitivity indices. Despite the statistical significance of the change, the sign of change remains unclear, which prevents us from extracting physical insight from ANOVA sensitivity indices (despite the statistical significance of changes). The largest impact among the couplings investigated here is found on atmospheric water. The maximum influence of soil-moisture on the atmospheric water vapor reveals a correlation of about 20% at the first vertical level. This decreases monotonically to about 10% at 2 km above surface. The SSP of soil significantly impacts the cloud water, but the impact of length scale differs among the atmospheric layer below 500 m and the region in between 500 m and 2 km above surface. While the largest-scale pattern of soil has maximum impact below 500 m (that is only for nighttime fog), it exhibits minor influence on the cloud water above 500 m. Instead, the maximum effect on the cloud water above 500 m is found for the smallest length scale pattern of soil where we in fact observe doubling of the bulk cloud water. Such impact on the bulk profiles was not observed in other physical cases (that is, for other variables, larger length scales or higher persistency) and indicates a threshold for cloud formation that is triggered in this particular case.

7.3. The role of length scale and persistency on surface–atmosphere couplings

Although we isolate the key coupling mechanisms by changing only one single surface property in the para-real simulations, the inter-related and non-linear processes cause considerable changes in all variables, i.e. those concerning the aerodynamic, thermodynamic *and* the hydrodynamic coupling mechanism. For instance, up to 15% of the atmospheric temperature variability can be explained through the surface pattern of roughness-length and up to 13% of the horizontal wind variability is explained by the soil-moisture pattern. We, however, find that the immediate impact of each surface property is largest in terms of the directly corresponding variable, i.e. albedo for atmospheric temperature, roughness-length for horizontal wind, and soil type for atmospheric water, where the large-scale forcing might no longer be considered external but become part of the set-up. When aiming at a quantification of the effect of the small-scale surface signal on large-scale phenomena, a simulation with larger domains and over an extended period of time should be considered.

Regarding the length-scale of the land-surface heterogeneity, the maximum surface signal is found in the atmospheric boundary layer up to 2 km height when the para-real simulation is forced by the SSP with the dominant length-scale about 10 km. At the smallest dominant length-scale considered here (300 m), the surface signal propagates vertically only when the immediate impact of land-surface heterogeneity is considered. That is, we only

find an impact of the roughness-length on the horizontal wind and of the soil-moisture on the water-vapor as it is explicitly encoded in the surface-layer similarity relations in Noah-MP-LSM. Further, with larger persistency of the SSP (i.e., less randomized SSP), the impact of the surface signal significantly strengthens.

While the signal on the bulk structure of the atmosphere is mostly negligible, for cloud-water above 500 m, the smallest length-scale SSP of soil-moisture induces more cloud-water. The SSP of soil with dominant length-scale about 10 km produces two times less cloud-water than the SSP of soil with dominant length-scale of about 300 m. In this context, the more noisy is the SSP, the more cloud-water is generated by convection. This needs further investigation with full consideration about time and vertical levels, since the scale-dependency of shallow convective clouds is found on the second day of simulation and the atmospheric layer between 500 m and 2 km. This approves findings of LIU AND SHAO [2013] about the time-scale dependence of atmosphere-soil coupling. The SSP of albedo and roughness-length does not affect the development of shallow convection, though we find that they are important in fog formation.

7.4. Synthesis

This work suggests that ANOVA method and its products, i.e., variance partitioning to dimensional subspaces and sensitivity indices, do not illustrate well the dynamic of atmosphere–surface exchanges. Although it allows an isolated analysis of the signal contained in a particular dimension (or combination of dimensions) of the atmospheric state, the *combined* ANOVA decomposed components demonstrate better the dynamic effect of the surface–atmosphere interactions than individual ANOVA decomposed components. In fact, the combined components are integration of the atmospheric state variables with respect to time or height, which can be obtained without computationally sophisticated ANOVA method.

To conclude, this work showed that there is a strong dependence of the length-scale of the surface forcing and the strength of atmosphere–surface coupling: the larger the length-scale of the surface pattern, the stronger the impact of the surface signal on the atmospheric state. Furthermore, higher persistence of the surface signal also strengthens the coupling mechanisms. It is verified that the dynamic effect of land-surface heterogeneity plays a major role in propagating the surface signal into the atmospheric boundary layer (both vertically and temporally). Atmosphere–land-surface couplings depend on the temporal evolution of the surface signal and our results illustrate: there is no simple linear forward propagation, but the impact of the local coupling significantly depends on external forcing. Finally, the results showed the key role that the hydrological mechanism

plays in coupling the surface to the atmosphere, and it highlights the importance of improving the representation of hydrological-processes in parameterization of the coupled land–atmosphere system.

A. Supplement figure

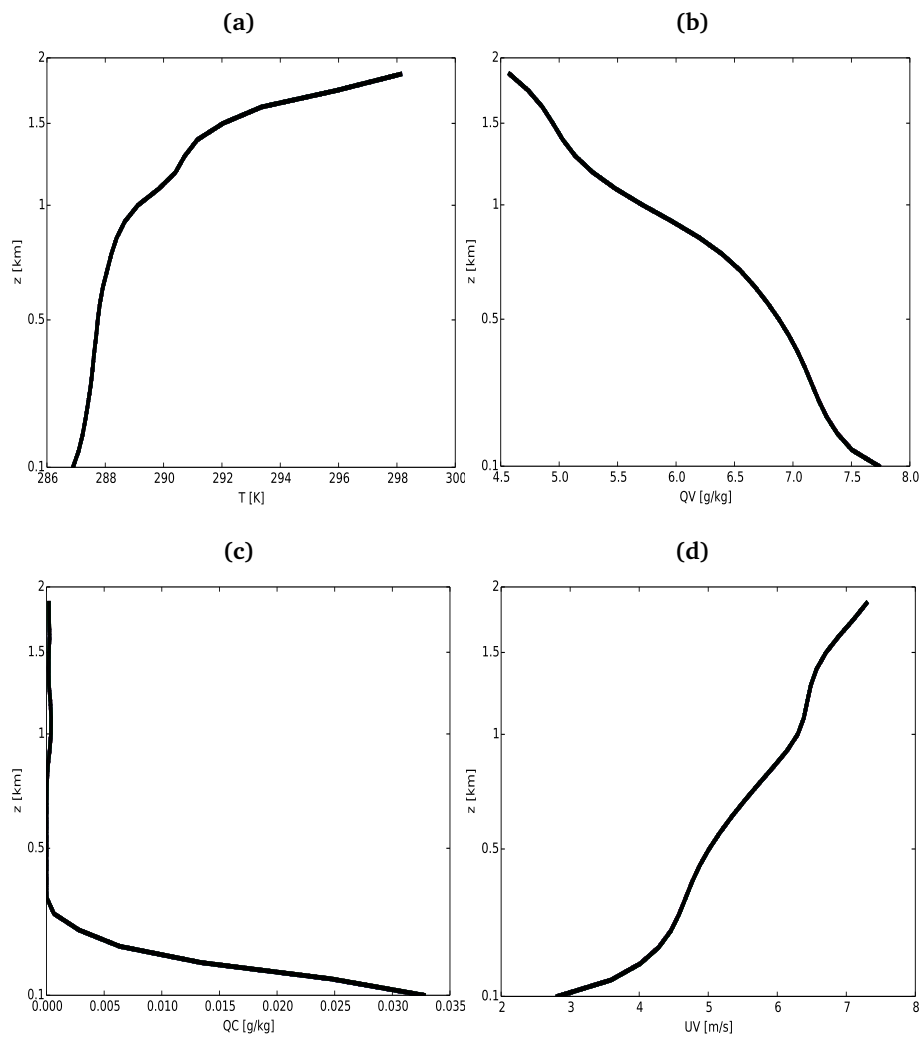


Figure A.1.: Vertical mean profile of temperature (a), water-vapor (b), cloud-water (c), and horizontal wind (d). The profiles are similar for all para-real simulations regardless of which surface properties used for forcing.

Bibliography

- Abedini, M. J. and Shaghaghian, M. R. (2009). Exploring scaling laws in surface topography. *Chaos, Solitons and Fractals*, 42(4):2373–2383.
- Ament, F. and Simmer, C. (2006). Improved representation of land-surface heterogeneity in a non-hydrostatic numerical weather prediction model. *Boundary-Layer Meteorology*, 121(1):153–174.
- Arakawa, A. and Lamb, R. V. (1977). Computational design of the basic dynamical processes of the UCLA general circulation model. *Methods of Computational Physics*, 17:173–265.
- Avissar, R. and Pielke, R. A. (1989). A Parametrization of Heterogenous Land Processes in Atmospheric Numerical Models. *Monthly Weather Review*, 117:2113–2136.
- Avissar, R. and Schmidt, T. (1998). An Evaluation of the Scale at which Ground-Surface Heat Flux Patchiness Affects the Convective Boundary Layer Using Large-Eddy Simulations. *Journal of the Atmospheric Sciences*, 55(16):2666–2689.
- Bhumralkar (1974). Numerical experiments on the computation of ground surface temperature in an atmospheric general circulation model. *Journal of Applied Meteorology*, 14:1246–1258.
- Blackmoret, D. and Zhou, G. (1998). A new fractal model for anisotropic surfaces. *International Journal of Machine Tools and Manufactur*, 38:551–557.
- Brunsell, N. A. and Anderson, M. C. (2011). Characterizing the multi-scale spatial structure of remotely sensed evapotranspiration with information theory. *Copernicus Publications on behalf of the European Geosciences Union*, 8(8):2269–2280.
- Bunde, A. and Shlomo, H. (1994). Fractals in Science. *Springer*, pages 10–115.
- Burrough, P. A. (2008). Fractal dimensions of landscapes and other environmental data. *Nature*, 294(5):240–242.
- Buttkus, B. (2000). Spectral Analysis and Filter Theory in Applied Geophysics. *Springer*, pages 165–170.

- Chen, S.-H. and Sun, W.-Y. (2002). A One-dimensional Time Dependent Cloud Model. *Journal of the Meteorological Society of Japan*, 80(1):99–118.
- Deardorff, J. W. (1978). Efficient prediction of ground surface temperature and moisture, with inclusion of a layer of vegetation. *Journal of Geophysical Research*, 83(7):1889–1903.
- Dee, D. P., Uppala, S., Simmons, A., Berrisford, P., Poli, P., Kobayashi, S., Andrae, U., Balmaseda, M. A., Balsamo, G., Bauer, P., Bechtold, P., Beljaars, A. C. M., van de Berg, L., Bidlot, J., Bormann, N., Delsol, C., Dragani, R., Fuentes, M., Geer, A. J., Haimberger, L., Healy, S. B., Hersbach, H., Hólm, E. V., Isaksen, I., Kallberg, P. W., Köhler, M., Matricardi, M., McNally, A. P., Monge-Sanz, B. M., Morcrette, J.-J., Park, B.-K., Peubey, C., de Rosnay, P., Tavolato, C., Thépaut, J.-N., and Vitart, F. (2011). The ERA-Interim reanalysis: Configuration and performance of the data assimilation system. *Royal Meteorological Society*, 137(9):553–597.
- Dickinson, R. E., Henderson-Sellers, A., and Kennedy, P. (1993). Biosphere-Atmosphere Transfer Scheme (BATS), Version 1e as coupled to the NCAR Community Climate model. *National Center for Atmospheric Research (NCAR)*.
- García-Carreras, L., Parker, D. J., and Marsham, J. H. (2011). What is the Mechanism for the Modification of Convective Cloud Distributions by Land Surface-Induced Flows? *Journal of the Atmospheric Sciences*, 68(3):619–634.
- García-Serrana, M., Gulliver, J. S., and Nieber, J. L. (2018). Description of soil microtopography and fractional wetted area under runoff using fractal dimensions. *Earth Surface Processes and Landforms*, 43(13):2685–2697.
- Gardiner, C. (2004). *Stochastic methods: a handbook for the natural and social sciences*. Springer, pages 77–85.
- Garrigues, S., Allard, D., Baret, F., and Weiss, M. (2006). Quantifying spatial heterogeneity at the landscape scale using variogram models. *Remote Sensing of Environment*, 103(1):81–96.
- Giorgi, F. and Avissar, R. (1997). Representation of heterogeneity effects in Earth system modeling: Experience from land surface modeling. *Reviews of Geophysics*, 35(4):413–437.
- Graves, T., Gramacy, R., Watkins, N., and Franzke, C. (2017). A brief history of long memory: Hurst, Mandelbrot and the road to ARFIMA. *arXiv:1406.6018v3*, 19(9):1–40.
- Gu, G. F. and Zhou, W. X. (2006). Detrended fluctuation analysis for fractals and multifractals in higher dimensions. *Physical Review E - Statistical, Nonlinear, and Soft Matter Physics*, 74(6):1–8.

- Hadfield, M. G., Cotton, W. R., and Pielke, R. A. (1991). Large-eddy simulation of thermally forced circulation in the convective boundary layer. Part I: A small-scale circulation with zero wind. *Boundary-Layer Meteorology*, 57:79–114.
- Hechtel, L. M., Moeng, C.-H., and Stull, R. B. (1990). The effect of nonhomogeneous surface fluxes on the convective boundary layer: a case study using large-eddy simulation. *Journal of the Atmospheric Sciences*, 47:1721–1741.
- Hintz, M., Lennartz-Sassinek, S., Liu, S., and Shao, Y. (2014). Quantification of land-surface heterogeneity via entropy spectrum. *Journal of Geophysical Research Atmosphere: Atmospheres*, 119:8764–8777.
- Hoeffding, W. (1948). A class of statistics with asymptotically normal distribution. *The Annals of Mathematical Statistics*, 19(3):293–325.
- Hong, S.-Y., Noh, Y., and Dudhia, J. (2006). A New Vertical Diffusion Package with an Explicit Treatment of Entrainment Process. *Monthly Weather Review*, 134:2318–2341.
- Honnert, R. (2019). Grey-Zone Turbulence in the Neutral Atmospheric Boundary Layer. *Boundary-Layer Meteorology*, 170(2):191–204.
- Hooker, G. (2007). Generalized functional ANOVA diagnostics for high-dimensional functions of dependent variables. *Journal of Computational and Graphical Statistics*, 16(3):709–732.
- Huang, H. Y. and Margulis, S. A. (2009). On the impact of surface heterogeneity on a realistic convective boundary layer. *Water Resources Research*, 45(4):1–16.
- Huang, H. Y. and Margulis, S. A. (2010). Evaluation of a fully coupled large-eddy simulation-land surface model and its diagnosis of land-atmosphere feedbacks. *Water Resources Research*, 46(6):1–19.
- Iacono, M. J., Delamere, J. S., Mlawer, E. J., Shephard, M. W., Clough, S. A., and Collins, W. D. (2008). Radiative forcing by long-lived greenhouse gases: Calculations with the AER radiative transfer models. *Journal of Geophysical Research Atmospheres*, 113(13):2–9.
- Jiménez, P. A., Dudhia, J., González-Rouco, J. F., Navarro, J., Montávez, J. P., and García-Bustamante, E. (2012). A Revised Scheme for the WRF Surface Layer Formulation. *Monthly Weather Review*, 140(3):898–918.
- Kessler, E. (1995). On the continuity and distribution of water substance in atmospheric circulations. *Atmospheric Research*, 38(32):109–145.
- Klemp, J. B., Skamarock, W. C., and Dudhia, J. (2007). Conservative Split-Explicit Time

- Integration Methods for the Compressible Nonhydrostatic Equations. *Monthly Weather Review*, 135(8):2897–2913.
- Laprise, R. (1992). The Euler equations of motions with hydrostatic pressure as an independent variable. *American Meteorological Society*, 120:197–207.
- Lhomme, J. P., A., C., and B., M. (1994). Effective parameters of surface energy balance in heterogeneous landscape. *Boundary Layer Meteorology*, 71:297–309.
- Liu, S. and Shao, Y. (2013). Soil-layer configuration requirement for large-eddy atmosphere and land surface coupled modeling. *Atmospheric Science Letters*, 14(2):112–117.
- Liu, S., Shao, Y., Kunoth, A., and Simmer, C. (2017). Impact of surface-heterogeneity on atmosphere and land-surface interactions. *Environmental Modelling and Software*, 88:35–47.
- Macke, A., Seifert, P., Baars, H., Barthlott, C., Beekmans, C., Behrendt, A., Bohn, B., Brueck, M., Bühl, J., Crewell, S., Damian, T., Deneke, H., Düsing, S., Foth, A., Di Girolamo, P., Hammann, E., Heinze, R., Hirsikko, A., Kalisch, J., Kalthoff, N., Kinne, S., Kohler, M., Löhnert, U., Lakshmi Madhavan, B., Maurer, V., Kumar Muppa, S., Schween, J., Serikov, I., Siebert, H., Simmer, C., Späth, F., Steinke, S., Träumner, K., Trömel, S., Wehner, B., Wieser, A., Wulfmeyer, V., and Xie, X. (2017). The HD(CP)2 Observational Prototype Experiment (HOPE) - An overview. *Atmospheric Chemistry and Physics*, 17(7):4887–4914.
- Mahfouf, JF., Richard E., Mascart P (1987). The influence of soil and vegetation on the development of mesoscale circulations. *Journal Climate Applied Meteorology*, 26:1483–1495.
- Mahrt, L. (2000). Surface heterogeneity and vertical structure of the boundary layer. *Boundary-Layer Meteorology*, 96(1-2):33–62.
- Manabe, S. (1969). Climate and the ocean circulation: I. The atmospheric circulation and the hydrology of the Earth's surface. *Monthly Weather Review*, 97(11):739–774.
- Mandelbrot, B. (1977). The fractal geometry of nature. *W. H. Freeman and Co.*
- Mandelbrot, B. B. and Van Ness, J. W. (1968). Fractional Brownian Motions, Fractional Noises and Applications. *SIAM Review*, 10(4):422–437.
- Muniandy, S. V. and Lim, S. C. (2001). Modeling of locally self-similar processes using multifractional Brownian motion of Riemann-Liouville type. *Physical Review E - Statistical, Nonlinear, and Soft Matter Physics*, 63(4 II):461041–461047.
- Niu, G. Y., Yang, Z. L., Mitchell, K. E., Chen, F., Ek, M. B., Barlage, M., Kumar, A., Manning, K., Niyogi, D., Rosero, E., Tewari, M., and Xia, Y. (2011). The community Noah land

- surface model with multiparameterization options (Noah-MP): 1. Model description and evaluation with local-scale measurements. *Journal of Geophysical Research Atmospheres*, 116(12):1–19.
- Oleson, K. W., Niu, G. Y., Yang, Z. L., Lawrence, D. M., Thornton, P. E., Lawrence, P. J., Stockli, R., Dickinson, R. E., Bonan, G. B., and Levis, S. (2007). Improvements to the Community Land Model and their impact on the hydrological cycle. *Journal of geophysical Research*, 133:G01021.
- Patton, E. G., Sullivan, P. P., and Moeng, C.-H. (2005). The Influence of Idealized Heterogeneity on Wet and Dry Planetary Boundary Layers Coupled to the Land Surface. *Journal of the Atmospheric Sciences*, 62(1995):2078–2097.
- Peitgen, H.-O. and Saupe, D. (1988). The Science of Fractal Images. *Springer*, pages:71–110.
- Raasch, S. and Harbusch, G. (2001). An analysis of secondary circulations and their effects caused by small-scale surface inhomogeneities using large-eddy simulation. *Boundary-Layer Meteorology*, 101(1):31–59.
- Rieck, M., Hohenegger, C., and van Heerwaarden, C. C. (2014). The Influence of Land Surface Heterogeneities on Cloud Size Development. *Monthly Weather Review*, 142(10):3830–3846.
- Rodriguez-Iturbe, I., K. Vogel, G., Rigon, R., Entekhabi, D., Castelli, F., and Rinaldo, A. (1995). On the spatial organization of soil moisture fields. *Geophysical research letter*, 22(20):2757–2760.
- Roy, S. B., Weaver, C. P., Nolan, D. S., and Avissar, R. (2003). A preferred scale for landscape forced mesoscale circulations? *Journal of Geophysical Research*, 108:1–11.
- Rutherford, A. (2011). ANOVA and ANCOVA: A GLM Approach. *John Wiley & Sons*, pages:4–52.
- Seth, A., Giorgi, F (1996). A three-dimensional model study of organized mesoscale circulations. *Journal of Geophysics Research*, 101:7371–7391.
- Shao, Y., Liu, S., Schween, J. H., and Crewell, S. (2013). Large-Eddy Atmosphere-Land-Surface Modelling over Heterogeneous Surfaces: Model Development and Comparison with Measurements. *Boundary-Layer Meteorology*, 148(2):333–356.
- Shao, Y., Sogalla, M., Kerschgens, M., and Brücher, W. (2001). Effects of land-surface heterogeneity upon surface fluxes and turbulent conditions. *Meteorology and Atmospheric Physics*, 78(3-4):157–181.
- Shen, S. and Leclerc, M. Y. (1995). How large must surface inhomogeneities be before

- they influence the convective boundary layer structure? A case study. *Quarterly Journal of the Royal Meteorological Society*, 121:1209–1228.
- Skamarock, W. C., Klemp, J. B., Dudhia, J., Gill, D. O., Barker, D. M., Duda, M. G., Huang, X.-Y., Wang, W., and Powers, J. G. (2008). A Description of the Advanced Research WRF Version 3. *NCAR Technical Note*.
- Sobol, I. M. (1993). Sensitivity analysis for nonlinear mathematical models. *Mathematical Modelling Computational Experiments*, 1(4):407–414.
- Wicker, L. J. and Skamarock, W. C. (2002). Time-Splitting Methods for Elastic Models Using Forward Time Schemes. *Monthly Weather Review*, 130(8):2088–2097.
- Wyngaard, J. C. (2004). Toward Numerical Modeling in the 'Terra Incognita'. *Journal of the Atmospheric Sciences*, 61(14):1816–1826.
- Yang, Z. L., Niu, G. Y., Mitchell, K. E., Chen, F., Ek, M. B., Barlage, M., Longuevergne, L., Manning, K., Niyogi, D., Tewari, M., and Xia, Y. (2011). The community Noah land surface model with multiparameterization options (Noah-MP): 2. Evaluation over global river basins. *Journal of Geophysical Research Atmospheres*, 116(12):1–16.

Erklärung

Ich versichere, dass ich die von mir vorgelegte Dissertation selbständig angefertigt, die benutzten Quellen und Hilfsmittel vollständig angegeben und die Stellen der Arbeit - einschließlich Tabellen, Karten und Abbildungen-, die anderen Werken im Wortlaut oder dem Sinn nach entnommen sind, in jedem Einzelfall als Entlehnung kenntlich gemacht habe; dass diese Dissertation noch keiner anderen Fakultät oder Universität zur Prüfung vorgelegen hat; dass sie -abgesehen von unten angegebenen Teilpublikationen- noch nicht veröffentlicht worden ist sowie, dass ich eine solche Veröffentlichung vor Abschluss des Promotionsverfahrens nicht vornehmen werde. Die Bestimmungen dieser Promotionsordnung sind mir bekannt. Die von mir vorgelegte Dissertation ist von Prof. Dr. Y. Shao betreut worden.

Köln, den 30.09.2019

Zahra Sadat Parsakhoo

Acknowledgement

First and foremost I wish to thank my advisor Professor Dr. Yaping Shao for encouraging my research and for allowing me to grow as a research scientist. His scientific guidance and advice on both research as well as on my career have been priceless. His patience lets me to be more productive and his deep and vast knowledge stimulates me to be more creative in my study. Above all, I would like to thank him for his constant support, his patient encouragement, and his unfailing dedication to this project.

I would also like to thank my committee members, PD Dr. Hendrik Elbern, and Dr. Cedrick Ansoerge for their constructive comments. I am also grateful to Prof. Joachim Saur for taking the time to be the chair of my advisory panel. I would especially like to thank Cedrick for his brilliant comments and suggestions. Without his help, I could not imagine to finish my PhD work in time. He involved in my study very patiently and supportive and he welcomed any discussion with me about technical issues and important concepts at any time with open arms.

Many thanks go to my colleagues in our research group and my former and present office- and floor-mates for their scientific and moral support, for their open ears to my worries and for all the nerdy fun we had together. Specially: Sven Ülbrich, Donata Banyte, Qian Xia, Robert Rauterkus, Philipp Henckes, Mahya Sadaghiani, and Kobra Khosravian.

Lastly, I would like to thank my family for all their love and encouragement. For my parents who raised me with a love of science and supported me in all my pursuits. Words cannot express how I grateful to them for all of the sacrifices that they have made on my behalf especially when I decided to move to Germany for my graduate study. And most of all for my loving, supportive, encouraging, and patient husband, Hassan Rahmany whose faithful support during the final stages of this Ph.D. is so appreciated. Last not least I thank my daughter, Dana. After her birth, new phase of my PhD started. She gave me a more cheerful life and colors my world outside of my office.

At the end, I would like to dedicate my thesis to wonderful, gentle, and beautiful soul of my grandfather, Baba-haji. With his sudden loss during my PhD time, a piece of my heart is also lost. God rest his soul in peace.